UNIVERSIDADE DE LISBOA
FACULDADE DE CIÊNCIAS
DEPARTAMENTO DE FÍSICA

Study of global dust storms on Mars using high resolution spectroscopy

Hermano Cardoso de Menezes Valido

Mestrado em Física
Astrofísica e Cosmologia

Dissertação orientada por:
Pedro Mota Machado

2019

Acknowledgements

First of all, I should say that completing this degree was an arduous and laborious endeavor, however, I feel gratified for, in doing so I have improved my scientific and human skills immeasurably. All of this could not have been possible without the human structure that allowed me to persevere.

I would like to thank all the professors I had throughout the course of this Master's degree, in particular, Prof. Iveta Pimental, the former Coordinator for the Master in Physics, for her friendly and welcoming attitude when I was starting my journey through this scientific area.

I would like to thank my thesis supervisor, Doutor Pedro Mota Machado, for introducing me to the world of scientific research and for teaching me how to be a scientist.

My journey would not have been possible without the love and support of my family, to whom this thesis is dedicated. To my father, for watching documentaries with me when I was growing up, getting me interested in science and for his example of hard work. To my mother for all, she gave up to raise me and my sisters, for all of her love and support and motivation to become whatever I want to be. To my 3 brothers and my 3 sisters for all their support and friendship. To my only friend who is as much part of my family as any of the above.

Lastly, I would like to acknowledge one more person, without whom I could never have completed this degree, my girlfriend. For her support, love, and example of strength and perseverance.

"For small creatures such as we the vastness is bearable only through love."

- Carl Sagan

Abstract

This thesis presents ground-based wind velocity measurements of Mars during the 2018 global dust storm using Doppler velocimetry based on observations made with the *Ultraviolet and Visual Echelle Spectrograph* (UVES) at the European Southern Observatory's Very Large Telescope (VLT) facility in Chile. This instrument's high resolution ($R \approx 100,000$) allows for the dust cloud velocity to be measured, by computing the Doppler shift induced in the Fraunhofer lines (in the $\lambda = 420 - 1100nm$) in the solar radiation that is backscattered in the dust, by the motion of that same dust, with an error of approximately $5ms^{-1}$. This allows us to sound Mars middle atmosphere during a global dust storm and obtain latitudinal wind profiles under the assumption that the non-zonal wind is negligible.

The purpose of this research project is to successfully apply and validate a new approach to investigate Mars' middle atmosphere wind velocities from ground-based observations. This is the first time that a Doppler velocimetry method based on observations made in the visible and ultraviolet wavelength range is employed to study the Martian atmosphere.

Global dust storms are complex stochastic events that can drastically alter the atmospheric dynamics. During such events dust can be lifted to heights above $50km$ across all latitudes and longitudes, increasing the optical depth for months and consequently the heating rates. The increased heating rates strengthen the Martian circulation. The processes that allow for the development of global dust storms are poorly understood. Furthermore, the cut-off mechanisms that spur the end of these storms are also without consensus and may even vary from storm to storm. These storms usually develop in the southern hemisphere during southern Summer and Spring ($L_s \approx 180° - 360°$), however, the 2018 storm started developing in the northern hemisphere on $L_s \approx 185°$.

The relative Doppler velocities were retrieved using the Doppler velocimetry technique, fine-tuned by our solar system group to the case of Venus (Machado, Luz, Widemann, Lellouch, & Witasse, 2012; Machado, 2014; Machado, Widemann, Luz, & Peralta, 2014; Machado et al., 2017) and adapted by me to the case of Mars. These velocities are measured relative to the reference pixel which we chose to be the one closest to the half phase angle point. This allows us to obtain the spatial and temporal wind variations.

The raw data was treated and reduced to apply our method. This included the computation of the master bias and master flat and the de-biasing and flat field the data images. Furthermore, a dispersion relation is constructed based on the Thorium-Argon lamp exposure to perform a very accurate wavelength calibration, essential for our method to be feasible. Lastly, the data was corrected to account for the curvature of the slit. This allowed the retrieval of the 1D-spectra from the raw *echellogramme*.

I adapted the MATLAB scripts from the pipeline, used for the case of Venus atmospheric studies, to the case of Mars. This includes the reduction of the active window of the slit and the adaptation of the different geometry of our observations. Spherical geometry was used to locate the observation within the planet and compute the de-projection factors for each point of the slit for each exposure to de-project the radial Doppler velocities from the observer's (Earth) line-of-sight.

The rotation velocity's contribution to the overall Doppler shift was removed by computing and sub-

tracting the rotation velocity at each point of the slit for all the positions. Furthermore, the contributions made to the total shift by the Young effect was evaluated and deemed negligible under the specific geometry of our observations.

The final velocities were computed and presented.

The next steps in this research project are to further improve the subtraction the planetary rotation contribution to the Doppler shifts, use radiative transfer models to better constrain the altitude that was being sounded and remove bad pixels creating unwanted effects on the observations.

Keywords: Mars, Dust Storms, Winds, Doppler Velocimetry, Planetary Atmospheres

Resumo

O projeto de investigação desenvolvido e aqui apresentado, foca-se numa tentativa de caracterização da baixa/média atmosfera durante uma tempestade de poeira global em Marte. Esta tese de mestrado foi realizado sob a orientação do Doutor Pedro Mota Machado, investigador do Instituto de Astrofísica e Ciências do Espaço (IA). O propósito deste trabalho de investigação é aplicar e validar uma nova abordagem que permite sondar as velocidades de vento na atmosfera de Marte a partir de observações terrestres. Esta é a primeira vez que uma técnica de velocimetria de Doppler, baseada em observações realizadas nos comprimentos de onda ultravioleta e visível, é aplicada ao estudo dos ventos em Marte. Esta técnica tem o potencial de providenciar uma nova forma de investigar este tipo de eventos em Marte e complementar estudos feitos com observações efetuadas a partir de sondas em órbita do planeta ou de *rovers* na superfície.

A tese apresenta medições de velocidades Doppler de ventos zonais na atmosfera de Marte, durante a tempestade de poeira global de 2018, obtidas através de velocimetria de Doppler a partir de observações efetuadas com o espectrómetro de alta resolução Ultraviolet and Visual Echelle Spectrograph (UVES) do *Very Large Telescope* (VLT) situada nas instalações do ESO no Chile.

A alta resolução do instrumento ($R \approx 100,000$) permite-nos medir a velocidade a que as nuvens de poeira se movem ao medirmos o desvio de Doppler induzido nas linhas Fraunhofer (no intervalo de comprimentos de onda $\lambda \approx 420\tilde{}1100nm$), da radiação solar que é dispersa na poeira suspensa na atmosfera, pelo movimento da poeira. Isto permite-nos investigar a atmosfera de Marte durante uma tempestade de poeira global e obter perfis latitudinais de ventos zonais sob a suposição de que o vento não zonal é desprezável.

As tempestades de poeira global são eventos complexos e estocásticos que fazem parte do ciclo de poeira presente em Marte. São capazes de provocar alterações drásticas das propriedades e dinâmicas atmosféricas. A poeira é elevada da superfície por ação do vento e pode atingir alturas acima dos $50km$ durante estes eventos, aumentando a profundidade ótica ao longo das várias latitudes e longitudes. A poeira é extremamente absorvente no infravermelho, o que aumenta as taxas de aquecimento e consequentemente fortalece a circulação, criando um ciclo de feedback positivo. Os processos que permitem o desenvolvimento

de tempestades de poeira global de 3 em 3 anos (R. Zurek & J. Martin, 1993) permanecem mal compreendidos. Além do mais, também não existe consenso relativamente aos mecanismos de cessação destas tempestades. Estes eventos geralmente desenvolvem-se no hemisfério do sul durante a Primavera e Verão (no hemisfério do sul - $L_s \approx 180° - 360°$ - período de Afélio) no entanto, esta desenvolveu-se no hemisfério do norte durante o equinócio de Primavera do hemisfério do sul ($L_s \approx 185°$).

A primeira confirmação de uma observação de uma tempestade de poeira global foi efectuada pela sonda Mariner 4 aquando da sua chegada a Marte em 1964. Desde então foram reunidas provas suficientes para a confirmação de outras 8 tempestades. Ao longo das últimas décadas várias missões foram desenvolvidas para estudar estes fenómenos e o seu efeito na atmosfera de Marte. No entanto o custo destas missões é extremamente elevado quando comparado com o custo de realização de observações telescópicas a partir da Terra.

As observações utilizadas neste trabalho de investigação foram efectuadas a 25 de Junho de 2018, com o braço vermelho do UVES/VLT, no Chile ao longo de 2 horas. A data das observações foi escolhida de modo a maximizar o diâmetro angular de Marte e minimizar o ângulo de fase. Com o objectivo de cobrir uma gama considerável de latitudes e longitudes foi utilizada uma configuração de fenda longa (0.3 segundos de arco de largura e 12 segundos de arco de comprimento). Foram efectuadas 80 exposições em duas configurações predefinidas (fenda espectroscópica alinhada perpendicularmente e paralelamente ao eixo de rotação do planeta) com 5 exposições por posição ao longo de várias posições. A resolução espacial obtida no centro do disco planetário é de aproximadamente $63km$.

Neste trabalho utilizou-se um método de medição directa dos ventos baseada em espectroscopia de alta resolução na gama de cumprimentos de onda do visível. Esta técnica é baseada no método de velocimetria de Doppler que foi aperfeiçoada para espectroscopia de fenda longa de grandes objectos alvo (Machado et al., 2012; Machado, 2014; Machado et al., 2014, 2017) e adaptada por mim para o caso de Marte. As velocidades neste método são medidas relativamente ao pixel de referência que escolhemos ser o píxel mais próximo do ponto de meio ângulo de fase. Isto permite-nos obter variações espaciais e temporais do vento.

O tratamento e a redução dos dados provenientes do UVES foram efectuados com recurso a um pacote de scripts MATLAB fornecido pelo Doutor Pedro Machado que os havia adaptado para o caso de Vénus. Isto inclui a computação do master bias e master flat e o seguinte processo de "de-bias" e "flat-field" das imagens. Além disso a relação de dispersão é construída com base na exposição à lâmpada de Tório-Argon de forma a calibrar os comprimentos de onda de forma muito precisa. Por fim os dados foram corrigidos de forma a contar com a curvatura da fenda. Este processo permite que se obtenham os espectros de alta resolução 1-D a partir dos *echellogrammes* brutos.

Efectuei a reprogramação dos scripts usados para os estudos atmosféricos de Vénus com vista a sua adaptação para o caso de Marte. Em primeiro lugar a redução da janela activa na fenda, em segundo lugar a utilização de geometria esférica para localizar todos os pontos das nossas observações dentro do globo e computar os factores de de projecção para cada um desses pontos. Isto permitiu de projectar as velocidades da linha de visão terrestre.

Para remover os efeitos da rotação planetária dos desvios de Doppler foi computado e removido a contribuição desta, para Doppler total, em cada ponto da slit, para todas as posições da slit. Foi ainda avaliada a possível contribuição do efeito de Young para os desvios Doppler medidos e considerada desprezável na geometria específica das observações efectuadas.

Foi calculada e apresentada, para cada píxel ao longo da fenda espectroscópica, as velocidades medidas. Há que ter em atenção que os detectores cobrem gamas de comprimento de onda diferentes e sondam diferentes profundidades ópticas.

Os resultados obtidos revelam o potencial desta técnica pioneira no estudo de velocidades de ventos a partir de observações terrestres, e em particular na investigação de eventos desta natureza em Marte. Esta técnica poderá permitir a caracterização do vento em função da latitude e hora local e o estudo da sua variabilidade espacial a temporal.

No seguimento de este projecto de investigação contemplam-se vários futuros desenvolvimentos.

Neste processo está incluído a melhor subtracção das contribuições da rotação planetária para os desvios de Doppler, utilizar modelos de transferência radiactiva para melhor restringir a altura que as nossas observações estão a sondar e remover pixeis defeituosos que criam efeitos indesejados nas nossas observações.

Palavras-Chave: Marte, Tempestades de Poeira, Ventos, Velocimetria de Doppler, Atmosferas Planetárias

Contents

List of Figures

List of Tables

List of Abbreviations

L_s Solar Longitude.

R_{eff} Effective radius.

λ Wavelength.

$\tau_{visible}$ Optical depth in the visible wavelength range.

ASPERA-3 Analyser of Space Plasmas and Energetic Ions for Mars Express.

CCD Charged Coupled Device.

CD Cross Disperser.

ESA European Space Agency.

ESO European Southern Observatory.

FITS Flexible Image Transport System.

GCM General Circulation Model.

HARPS High Accuracy Radial velocity Planet Searcher.

HRSC High Resolution Stereo Camera.

JPL Jet Propulsion Laboratory.

LMD Laboratoire de Météorologie Dynamique.

MARCI Mars Color Imager.

MaRS Mars Radio Science.

MARSIS Mars Advanced Radar for Subsurface and Ionosphere Sounding.

MCO Mars Climate Orbiter.

MCS Mars Climate Sounder.

MDGM Mars Daily Global Maps.

MGS Mars Global Surveyor.

MO Mars Observer.

MOC Mars Orbiter Camera.

MRO Mars Reconnaissance Orbiter.

NASA National Aeronautics and Space Administration.

NPH North polar hood.

OMEGA Observatoire pour la Minéralogie, l'Eau, les Glaces et l'Activité.

PFS Planetary Fourier Spectrometer.

SHP South polar hood.

SPICAM Spectroscopy for the Investigation of the Characteristics of the Atmosphere of Mars.

TES Thermal Emission Spectrometer.

THEMIS Thermal Emission Imaging System.

UVES Ultraviolet and Visual Echelle Spectrograph.

VLT Very Large Telescope.

VMC Visual Monitoring Camera.

1 Introduction

Mars, because it can be seen by the naked eye (at least once every 2 years or so) was one of the first celestial objects to be identified as a planet and consequently observed and studied by ancient astronomers. In 1610 Galileo Galilei used a telescope (that he had built himself) to see a magnified image of Mars for the first time in history. Today there have been eight successful landings on the Martian surface and several more spacecraft successfully put into orbit. Each of these amazing accomplishments is a small (or not so much) part of a much larger endeavor - the study and exploration of the planet Mars.

The European Space Agency's (ESA) mission Mars Express, a mission that has been active for over fifteen years, had an estimated total cost of approximately 300 million Euro which included spacecraft, payload, launch, and operations costs (ESA, 2017). NASA's Curiosity rover which integrates the Mars Science Laboratory mission has had an estimated cost of more than 2 billion US Dollars (*NASA Mars Science Laboratory Landing Press Kit*, 2012). The number of hours spent by researchers preparing, analyzing and studying the data from these two missions alone is beyond counting. Why is it worth to spend all these resources studying a planet that distances millions of kilometers from Earth? Why should all this time and money be spent studying Mars and, in particular, its atmosphere?

Mars has a terrestrial atmosphere meaning that a better understanding of the Martian atmosphere can potentially improve our comprehension of both our atmosphere and planetary atmospheres in general. This is incredibly valuable in the field of exoplanetary research, where the characterization of atmospheres with limited data is essential to identify potentially habitable planets. Furthermore, a precise and extensive characterization of Mars' atmosphere is an essential pre-requisite for any mission (manned or not) to Mars. Additionally since plaque tectonics, which constantly and continuously destroys ancient rock records that contain invaluable data about the history of our planet, is thought to barely exist on Mars, such record would be preserved and might provide us with important geological data. This is one (among others) excellent motivator for the exploration of this planet Mars.

1.1 Scientific Context

In February 1971 Charles F. Chapen, (a famous astronomer at the time employed at the Lowell Observatory's Planetary Research Center) made the following prediction regarding Mars and the Mariner missions in particular (Sheehan, 1996a):

> *If a bright yellow cloud again develops in the Hellespontus region [as was the case in 1956], ... it will likely do so after opposition. A vast atmospheric disturbance could interfere with ... the first Mariner or biter spacecraft mission, which is planned to begin reconnaissance of the planet in November.*

Mariner 9 was launched on the 30^{th} of May 1971 (shortly after the launch failure of Mariner 8) and arrived on Mars in early November of the same year. Upon its arrival, it found the whole planet indistinguishably covered by suspended dust - a global dust storm which obscured the whole planet was

occurring, the first ever to be confirmed. If not for the versatility and adaptability of the mission's plan, a large part of the planned data collection and the bulk of the mission's objectives would have gone unfulfilled.

Global dust storms are unique to Mars and are, perhaps, the most spectacular atmospheric event taking place anywhere in the Solar System (see Figure 1.1). These storms induce thermodynamic responses throughout the whole atmosphere however, their occurrence is unpredictable and shows inter-annual variability and despite the massive development our understanding of Mars has suffered over the last 50 years, these storms are still viewed as stochastic events and the issue of their year-to-year variability remains largely unresolved.

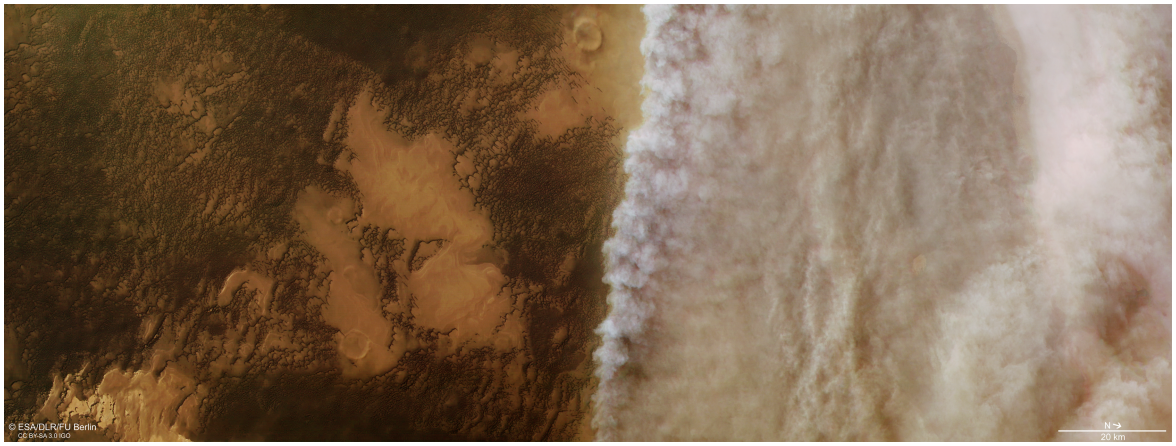

Figure 1.1: High resolution stereo camera (HRSC) on board ESA's Mars Express captured image of an up-welling front of dust clouds – visible in the right half of the frame – near the north polar ice cap of Mars in April, 2018. Source: Space in Images .

Global dust storms do strengthen the circulation, however, due to the low mass of the Martian atmosphere, the winds carry little momentum and pose little threat to man-made structures. Their characterization is, nonetheless crucial, as they are critical to the Martian climate and can pose other dangers. These storms can lift enough dust into suspension to dramatically increase the opacity of the atmosphere for several months. A consequence example is the recent 'demise' of NASAs Opportunity Rover - which was solar-powered and did not survive the 2018 global dust storm. These storms are also believed to be electrically charged, which can pose a serious threat to any operational electronic devices. Furthermore, recent findings suggest that such storms may have played an important role in Mars' loss of water (Vandaele et al., 2019).

With the planning of further exploration - including manned missions - in the next decade or so, the interest in the study of such phenomenon and its effects on the atmosphere has grown substantially among the astrophysics scientific community.

1.2 Objectives

The scope of this work is to study the behavior of Mars' middle atmosphere during a global dust storm using ground-based observations made with VLT-UVES and Doppler velocimetry techniques, for the first time, to complement observations of orbiter instruments. The success and validation of the application

of this method to the atmosphere of Mars may provide a new, unique way to investigate the Martian atmosphere during global dust storms.

The intent is to contribute to a better understanding of the circulation during planet-encircling dust events. We measured the wind velocity and its spatial and temporal variability, through high resolution spectroscopy and Doppler velocimetry. The observations were made with the high-resolution spectrograph UVES with ESO's Very Large Telescope (VLT) in the visible wavelength range.

The main goal of this research line is therefore, to provide direct instantaneous (the velocities retrieved for each pixel sounding the planet are obtained simultaneously) wind measurements using visible Fraunhofer lines scattered at Mars' dust hazes, which allows spatial wind variability studies and will make possible to obtain a latitudinal profile of the wind.

1.3 Structure

The thesis is arranged as follows:

- Section 2 gives an introductory description of Mars atmosphere's most relevant features along with a history of its exploration (focused on the last century).
- Section 3 describes the Ultraviolet and Visual Echelle Spectrograph instrument at the Very Large Telescope facility and the observations (including the circumstances in which they were made) and provides a global picture of the onset and decay of the 2018 global dust event.
- Section 4 depicts in detail the Doppler velocimetry method used in this work, including the data reduction and the corrections made. Additionally, it presents and succinctly describes the Doppler velocities retrieved.
- Section 5 summarily discusses the results while giving an outlook on possible future work.

2 Mars

Mars and Earth formed through similar processes in regions of similar distance to the center of the proto-planetary disk. However Earth and Mars share more than just an origin, Table 2.1 and Table 2.2 list some of the parameters for Mars and Earth. It is noteworthy that Mars' rotation period is remarkably similar to Earth's and in clear weather conditions, both atmospheres are transparent at visible wavelengths.

Since both planets are heated by radiative and convective exchanges with the surface the global circulation is extremely alike. Even though Earth and Mars equatorial radius differ by a factor of ≈ 0.5 they have similar values of total land area. Furthermore, just like Earth, Mars' rotation also has a tilt (≈ 25.19 on Mars and ≈ 23.44 on Earth; see Table 2.2) meaning that both planets have seasonal cycles. It is even possible that Mars had a more Earth-like environment in the past, and there even have been suggestions that life may have once existed on Mars.

Table 2.1: Parameters for Mars and Earth. Source: Compiled from Wilson (2003) and NASA Space Science Data Coordinated Archive (Williams, 2018a).

Parameters	**Mars**	**Earth**
Mass ($10^{24}kg$)	0.64171	5.9724
Volume ($10^{10}km^3$)	16.318	108.321
Equatorial Radius (km)	3396.2	6378.1
Polar Radius (km)	3376.2	6356.8
Mean Density (kg/m^3)	3933	5514
Surface Gravity (m/s^2)	3.71	9.80
Surface Pressure ($mbar$)	$500 - 800$	101300
Surface Area (km^2)	1.4437	5.1006
Surface Area without oceans (km^2)	1.4437	1.4894
Number of Natural Satellites	2	1
Topographic Range (km)	30	20
Visible Atmospheric Optical Depth	$0.1 - 10$	$0.2 - 100$
Average Temperature (K)	210	288

Table 2.2: Orbital parameters for Mars and Earth. Source: Compiled from NASA Space Science Data Coordinated Archive (Williams, 2018a).

Parameters	**Mars**	**Earth**
Semi-major Axis (10^6km)	227.92	149.6
Sidereal Orbit ($days$)	686.980	365.256
Perihelion (10^6km)	206.62	147.09
Aphelion (10^6km)	249.23	152.10
Synodic Period ($days$)	779.94	–
Maximum Orbital Velocity (km/s)	26.50	30.29
Minimum Orbital Velocity (km/s)	21.97	29.29
Orbital Eccentricity	0.0935	0.0167
Orbital Inclination (deg)	1.850	0.000
Sidereal Rotation Period (hrs)	24.6229	23.9345
Obliquity to Orbit (deg)	25.19	23.44

The similarities are remarkable, Sir William Herschel acknowledged this resemblance in Herschel, 1784 (as cited in Sheehan, 1996b):

> *The analogy between Mars and the earth is, perhaps, by far the greatest in the whole solar system. The diurnal motion is nearly the same; the obliquity of their respective ecliptics, on which the seasons depend, not very different; of all the superior planets the distance of Mars from the sun is by far the nearest alike to that of the earth: nor will the length of the martial year appear very different from that which we enjoy, when compared to the surprising duration of the years of Jupiter, Saturn, and the Georgium Sidus [Uranus]. If, then, we find that the globe we inhabit has its polar regions frozen and covered with mountains of ice and snow, that only partly melt when alternately exposed to the sun, I may well be permitted to surmise that the same causes may probably have the same effect on the globe of Mars; that the bright polar spots are owing to the vivid reflection of light from frozen regions; and that the reduction of those spots is to be ascribed to their being exposed to the sun.*

Nevertheless, there are still substantial differences between both atmospheres, and these can have profound implications on the atmospheric conditions and overall climate. Mars orbit is not as circular as Earth's, at perihelion ($L_s \approx 251°$) Mars is 20% closer to the Sun that at Aphelion ($L_s \approx 70°$). This means that in addition to having seasons caused by the obliquity of its rotation (analogously to Earth), Mars also has seasons due to the eccentricity of its orbit.

The atmosphere is smaller in mass and composed primarily of carbon dioxide. Driven by the seasons, CO_2 follows an annual cycle of condensation and deposition of CO_2 ice on the poles and consequent sublimation. Through the course of this cycle, the total mass of the atmosphere varies and since the CO_2 is the main component, mixing ratios of less abundant molecules change significantly.

The CO_2 cycle is not the only that greatly influences atmospheric dynamics. The Martian atmosphere has a permanent layer of suspended dust which is mainly composed of silicon dioxide (SiO_2). This dust layer has an optical depth of $\tau \approx 0.3 - 0.5$ in the clearest seasons but can reach much greater values during dust storms. Such storms are ubiquitous on Mars (particularly in southern summer and spring) and can reach planet-encircling scales. Consequently, the global and local circulation can vary significantly, since dust injected into the atmosphere can affect the solar heating rates, the temperature, and the pressure field.

Both H_2O and dust also follow annual cycles and are at some point present in the form of clouds (or hazes). Both these aerosols absorb visible and ultraviolet radiation considerably heating the atmosphere, therefore, changing the thermal structure and changing the dynamics of the atmosphere. These cycles have as much influence on the climate as they do on one another.

Despite being transparent to the solar visible radiation, the light that passes through the atmosphere is absorbed by the surface and re-emitted in the infra-red. Consequently, the CO_2, which is very absorbent in that wavelength range, absorbs the light, increasing the atmospheric temperature. As opposed to the case of Earth, Mars does not have a stratosphere-like layer where solar heating from the ozone layer happens instead, it is usually divided (thermodynamically) into three layers. The average temperature is approximately $210K$ however, a much greater thermal amplitude (on both short and long time-scales)

is present. These amplitudes are enhanced by the low thermal inertia caused by the lack of oceans, by the superimposition of the southern summer solstice ($L_s = 270°$) and perihelion and by the increased presence of dust storms during this season.

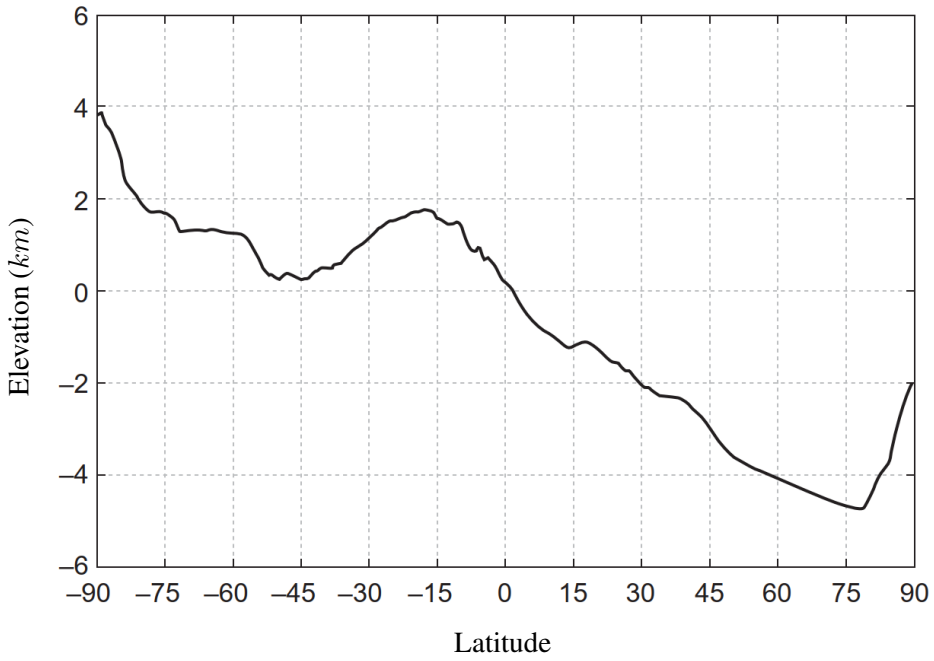

Figure 2.1: Zonally averaged topography. Data from Mars Orbiter Laser Altimeter (Mars Global Surveyor) Source: Read and Lewis (2006).

Just like Earth, Mars' global circulation is dominated by a Hadley circulation, but its latitudinal extent is much larger (in part due to the planet's small size). At a local near-surface scale, topography dominates the dynamics. This can create dichotomies between both hemispheres since the northern hemisphere has a much lower mean elevation (Smith et al., 1999). Additionally, the northern hemisphere is much smother (see Figure 2.1), this indicates that the surface of the northern hemisphere is more recent which means that at some point Mars was probably geologically active and could have even had a strong magnetic field.

The greatest difference between the study of both atmospheres resides in the observation and data collection. We do not have a complete spatial and temporal coverage on Mars, as we do on Earth, for most observed properties. It is extremely hard to understand a complex system like the Martian atmosphere with limited data. Nevertheless, each observation is useful, as it can be used to constrain general circulation models (GCMs) which are detrimental in the understanding and interpretation of the global processes that rule the Martian climate.

2.1 Composition

The Martian atmosphere is light compared to Earth's (it contains $\approx$ 9 times less mass) which leads to a surface atmospheric pressure of approximately $8\ mbar$ ($\approx 0.5\%$ of Earth's surface atmospheric pressure). However, Mars' surface pressure is not constant, it varies greatly at several time-scales:

– **Annual:** CO_2, which makes up $\approx 95\%$ of the atmosphere (see Table 2.3), follows a annual cycle

in which it condensates on to the seasonal cap in the winter pole and sublimates from the seasonal cap in the summer pole, varying it total atmospheric abundance by $\approx 30\%$. This variation alters the total mass of the atmosphere and consequently, it changes the surface pressure in a cyclic fashion (see Figure 2.2).

– **Diurnal:** The low thermal inertia of the surface combined with the lack of oceans and the varying solar isolation (throughout the day) creates sun-synchronous diurnal thermal tides. These tides heat (during the day) and cool (during the night) the atmosphere, expanding and contracting it respectfully, altering the surface pressure daily (see Figure 2.3).

– **Semi-Diurnal:** Semi-diurnal (last half a day) tidal components have been observed since the Viking missions. This semi-diurnal temperature variation increases with dust loading (Wilson & Richardson, 2000).

Mars' atmosphere is composed mainly of carbon dioxide ($\approx 95\%$) with minor amounts of Argon ($\approx 0.2\%$) and nitrogen ($\approx 0.2\%$) and trace amounts of other elements, like oxygen, water, hydrogen, ozone and methane (see Table 2.3).

CO_2 and H_2O follow seasonal cycles as well and can both condensate to form ice clouds. Thus both their abundances show temporal variability. Other non-condensible elements do not alter their absolute abundances but they do, however, change their relative abundance as a consequence of the varying absolute abundance of other elements (Smith, Bougher, Encrenaz, Forget, & Kleinböhl, 2017).

Dissociation of the carbon dioxide by ultraviolet sunlight (see Table 2.4 - R2) produces both carbon monoxide and atomic oxygen. The inverse reaction (see Table 2.4 - R3) however, is spin forbidden and too slow. The competing reaction, the formation of molecular oxygen, (see Table 2.4 - R15) has a rate constant a few orders higher. This mean the abundance of dissociation products like CO, O_2, O_3 and O should be greater and the amount of the CO_2 in the atmosphere should not be as stable (Yung & DeMore, 1998).

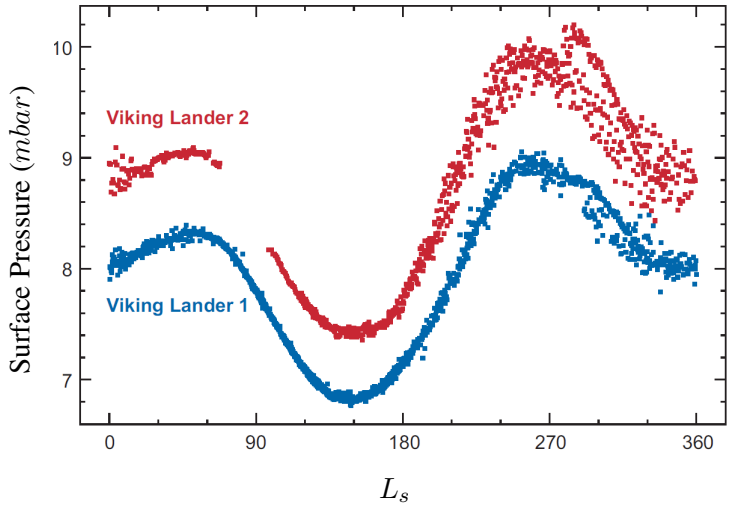

Figure 2.2: Daily averages of surface pressure (mbar) as recorded by the two Viking Lander spacecraft. The shift between both curves results from elevation differences in both landing sites. Source: Smith (2008).

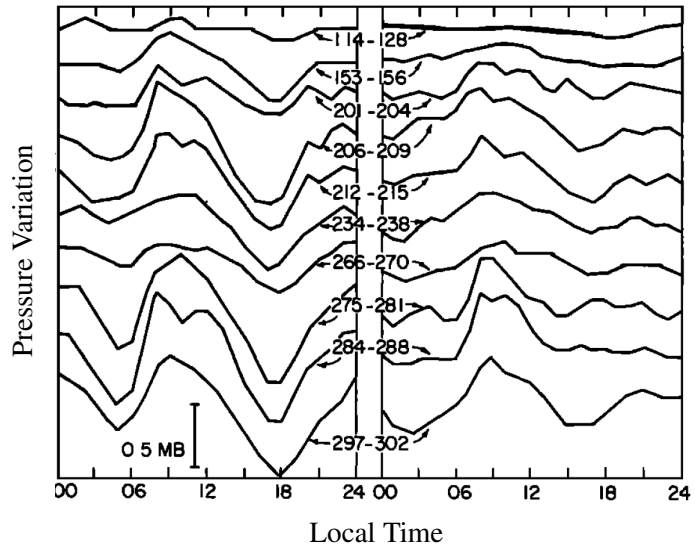

Figure 2.3: Daily variation of surface pressure as recorded by Viking Lander 1 (on the left) and by Viking Lander 2 (on the right). Source: Leovy and Zurek (1979).

Despite being present in small quantities water vapor plays a pivotal role in the photochemical stability of the CO_2 rich Martian atmosphere. The photolysis of H_2O by absorption of ultraviolet radiation (see Table 2.4 - R1) provides hydrogen radicals (HO and H). Reactions R4, R6 and R9 (see Table 2.4) form a cycle where CO_2 is formed and HO is used as a catalyst. This cycle rate constant is several orders of magnitude higher than R3 (see Table 2.4) and accounts for the removal of oxygen bellow $\approx 25km$ (McElroy & Donahue, 1972) and for $\approx 85\%$ of the recycling of CO into CO_2 (Krasnopolsky, 2010). It is noteworthy that the HO molecules are not consumed in this cycle and therefore, very few of them are required for this process to be effective (Yung & DeMore, 1998).

Table 2.3: The abundance of the major gases that make up the Mars' atmosphere. Source: (Smith et al., 2017).

Gaseous Species	**Average Abundance**	**Reference**
CO_2	0.9532	Owen et al. (1977)
N_2	0.027	Owen et al. (1977)
	0.019	Mahaffy et al. (2013)
Ar	0.16	Owen et al. (1977)
	0.19	Mahaffy et al. (2013)
O_2	0.0014	Hartogh et al. (2010)
CO	$800ppm$	Smith et al. (2009)
H_2O	$15\breve{}1500ppm$	Smith (2004)
H_2	$15ppm$	Krasnopolsky and Feldman (2001)
Ne	$2.5ppm$	Owen et al. (1977)
Kr	$0.3ppm$	Owen et al. (1977)
Xe	$0.08ppm$	Owen et al. (1977)
O_3	$10\breve{}350ppb$	Perrier et al. (2006)
H_2O_2	$10\breve{}40ppb$	Encrenaz et al. (2004)
CH_4	$0\breve{}40ppb$	Mumma et al. (2009)
	$0.7\breve{}7ppb$	Webster et al. (2015)
	$13\breve{}18ppb$	Giuranna et al. (2019)

Table 2.4: Relevant reactions with their rate constants. For two-body reactions the units are $cm^3 s^{-1}$, and for three-body reactions the units are $cm^6 s^{-1}$. M represents the background gas (usually CO_2). Source: Adapted from (Atreya & Gu, 1995).

N_o	**Reactions**	**Rate Constants**	**Reference**
R1	$H_2O + h\nu \longrightarrow OH + H$		Thompson et al. (1963)
R2	$CO_2 + h\nu \longrightarrow CO + O$		Atreya and Gu (1994)
R3	$CO + O + M \longrightarrow CO_2 + M$	$9.8 \cdot 10^{-33} \cdot e^{\frac{-2180}{T}}$	Slanger et al. (1972)
R4	$H + O_2 + M \longrightarrow HO_2 + M$	$5.7 \cdot 10^{-32} \cdot (\frac{T}{300})^{-1.6}$	DeMore et al. (1992)
R5	$HO_2 + HO_2 \longrightarrow H_2O_2 + O_2$	$2.3 \cdot 10^{-13} \cdot e^{\frac{600}{T}}$	DeMore et al. (1992)
R6	$O + HO_2 \longrightarrow OH + O_2$	$2.9 \cdot 10^{-11} \cdot e^{\frac{200}{T}}$	Atkinson et al. (1989)
R7	$H_2O_2 + h\nu \longrightarrow OH$		Okabe (1978)
R8	$HO_2 + h\nu \longrightarrow OH + O$		Okabe (1978)
R9	$CO + OH \longrightarrow CO_2 + H$	$4.35 \cdot 10^{-14} \cdot (\frac{T}{298})^{1.35} \cdot e^{\frac{365}{T}}$	Larson et al. (1988)
R10	$H + HO_2 \longrightarrow 2\,OH$	$7.2 \cdot 10^{-11}$	Atkinson et al. (1989)
R11	$H + HO_2 \longrightarrow H_2 + O_2$	$5.6 \cdot 10^{-12}$	Atkinson et al. (1989)
R12	$H + HO_2 \longrightarrow H_2O + O$	$2.4 \cdot 10^{-11}$	Atkinson et al. (1989)
R13	$H + O_3 \longrightarrow OH + O_2$	$1.4 \cdot 10^{-10} \cdot e^{\frac{-470}{T}}$	DeMore et al. (1992)
R14	$O + OH \longrightarrow O_2 + H$	$2.2 \cdot 10^{-11} \cdot e^{\frac{120}{T}}$	DeMore et al. (1992)
R15	$O + O + M \longrightarrow O_2 + M$	$5.21 \cdot 10^{-35} \cdot e^{\frac{900}{T}}$	Tsang and Hampson (1986)
R16	$O + O_2 + M \longrightarrow O_3 + M$	$6.0 \cdot 10^{-34} \cdot (\frac{T}{300})^{-2.3}$	DeMore et al. (1992)
R17	$OH + HO_2 \longrightarrow H_2O + O_2$	$4.8 \cdot 10^{-11} \cdot e^{\frac{250}{T}}$	Keyset (1988)
R18	$H_2O_2 + OH \longrightarrow HO_2 + H_2O$	$2.9 \cdot 10^{-12} \cdot e^{\frac{-160}{T}}$	DeMore et al. (1992)
R19	$O_3 + h\nu \longrightarrow O_2 + O(^1D)$		WMO (1985)
R20	$O_3 + h\nu \longrightarrow O_2 + O(^3P)$		WMO (1985)
R21	$O_2 + h\nu \longrightarrow 2\,O$		Watanabe et al. (1953)

At high altitudes, where the HO_2 abundance is very small there is an alternative cycle that also uses OH as a catalyst. R13, R16 and R9 (see Table 2.4) form a similar cycle that uses O_3 instead of O_2 to restore the HO_2 (McElroy & Donahue, 1972; Atreya & Gu, 1995). Ozone is also removed by photolysis (see Table 2.4 - R19, R20).

Hydrogen peroxide is a indirect product of H_2O photolysis, it forms via R5 (see Table 2.4). This is an important species because, like H_2O, it suffers photolysis (see Table 2.4 - R7) and provides the atmosphere with hydrogen radicals. This creates a new variant of the CO_2 production cycle (see Table 2.4 - 2R9, 2R4, R5 and R7) where once again OH acts like a catalyst (Yung & DeMore, 1998). Furthermore H_2O_2 is also believed to be responsible for the oxidation of the Martian surface and therefore its reddish color.

We have seen that due to the presence of water in the middle and low atmosphere, hydrogen radicals are also present at these altitudes. Reaction R14 (see Table 2.4) is the primary source ($\approx 90\%$) of O_2 on Mars (Lefèvre & Krasnopolsky, 2017). The loss of oxygen occurs by R4 (see Table 2.4) but this reaction does not break the $O-O$ bond and the O_2 is immediately returned by reaction R6 (see Table 2.4). Around 80% of the breaking of the $O-O$ bond is accounted for by the photolysis of oxygen (R21), hydro-peroxyl (R8), hydrogen peroxide (R7) and by reaction R10 (see Table 2.4) (Lefèvre & Krasnopolsky, 2017). However most of the odd oxygen ($O(^1D)$, O and O_3) produced comes not from

any of the above-mentioned reactions (that depend on species whose abundance is minimal) but from the photolysis of carbon dioxide (see Table 2.4 - R2). At high altitudes, these atoms are only lost by reaction R15 (see Table 2.4) which is very slow and yields enough photochemical lifetime to allow the Hadley circulation to transport it to lower altitudes and high latitudes. At these altitudes, in the polar night, oxygen atoms are removed via the formation of ozone (see Table 2.4 - R16) while in the sunlit part of the atmosphere O_3 suffers photolysis (see Table 2.4 - R19 and R20) (Lefèvre & Krasnopolsky, 2017). However, the low abundance of ozone (see Table 2.3) means that it does not offer protection (like Earth does) against ultraviolet radiation.

Nitrogen is the second most abundant molecule on the Martian atmosphere (see Table 2.3). The strong $N-N$ bond keeps this molecule uncreative but it can be broken by absorption of extreme ultraviolet solar radiation or photoelectrons in the ionosphere. A part of the subsequent production of odd nitrogen (N and NO) survives long enough to be transported to the lower atmosphere where they will contribute to the formation of higher oxides of nitrogen (which, as we have seen, are crucial to the stability of the atmosphere) (Lefèvre & Krasnopolsky, 2017).

Hydrogen is produced as result of the dissociation of H_2O (see Table 2.4 - 2R11, 2R1, R9, R2, R14 and 2R4). While most of the hydrogen produced will be removed by reacting with hydroxide or oxygen atoms, $\approx 20\%$ will be transported to the upper atmosphere. Once in the ionosphere H_2 is decomposed by ionospheric reactions and can escape thermally from the atmosphere (Yung & DeMore, 1998). It also takes part in one of three photochemical cycles responsible for the production of CO_2 ($\approx 5 - 10\%$). As a consequence oxygen atoms are produced which, in turn, contributes to the production of ozone.

Argon is one of the most abundant molecules after carbon dioxide (see Table 2.3) and it is crucial in the understanding of the evolution of the Martian atmosphere. As Ar does not react with anything else on the atmosphere of Mars, it can only be lost to space by sputtering. Fractionation of Argon occurs as a consequence of sputtering and the ratio of $^{38}Ar/^{36}Ar$ is a good monitor of those atmospheric losses. It is currently believed that Mars actually evolved from a more earth-like climate to the current dry and cold atmosphere primarily through loss of atmosphere (Jakosky et al., 2017).

Methane is perhaps the most debated molecule present in the Martian atmosphere. It has been reported to be present (and missing) several times, with overall differences in abundances and, until very recently, without independent confirmation. The origin is also highly debated as a biogenic origin could be a signature of life (even if long ago). The most recent developments suggest that methane is being freed by faults within the ice which release the underlying trapped gases (Giuranna et al., 2019).

2.2 Structure

Mars' atmosphere's thermal structure shares many aspects with Earth's. Like Earth, Mars' atmospheric temperatures generally decrease with height but unlike it, there is no ozone layer to absorb ultraviolet radiation. Mars globally averaged surface temperature is around $200K$ but the thermal tides (see Section 2.1) insure a high thermodynamic variability, particularly close to the surface.

The Martian atmosphere is thermally divided into 3 layers (see Figure 2.4): the lower, the middle

and the upper atmosphere.

The lower atmosphere extends from the surface to $\approx 50km$ of altitude ($\approx 2Pa$). Its analog on Earth is the troposphere and identically, it is dominated by heat exchanges with the surface. The surface's albedo, thermal inertia, slope, and the atmospheric opacity contribute to the local atmospheric temperature but on a global scale, it is mostly controlled by solar insolation (Smith et al., 2017).

Mars' solar insolation seasonal variation is about 30% and so the temperatures of the lower atmosphere are highly dependent on the season. At high latitudes obliquity seasons dominate (temperatures are hotter at Summer solstice and cooler at Winter solstice) and despite having some relevance near the surface at low latitudes, orbital seasons tend to control the lower atmosphere's temperature at low latitudes (Smith et al., 2017).

The summer hemisphere's pole has the highest insolation values and consequently has higher surface temperatures but it has a relatively low-temperature gradient. In the winter hemisphere temperatures are very cold but the Hadley circulation present at that season transports warm air to high latitudes creating an inversion layer above the poles (McCleese et al., 2008; McCleese et al., 2010). During equinoxes the roughly symmetric Hadley circulation ensures the highest temperatures are found at tropical latitudes near the surface, decreasing towards the poles for altitudes bellow $30km$ (Smith, 2008; McCleese et al., 2010).

Identically to Earth's troposphere, the Martian lower atmosphere temperature is highest close to the ground and drops with height, having a relatively low lapse rate ($\approx 2.5Kkm^{-1}$) due to the constant presence of suspended dust particles which absorb radiation and release latent heat (R. Haberle, 2015; Smith et al., 2017). Ice clouds also play a role in regulating temperatures as they warm the atmosphere at low latitudes during the aphelion season (Clancy et al., 2017).

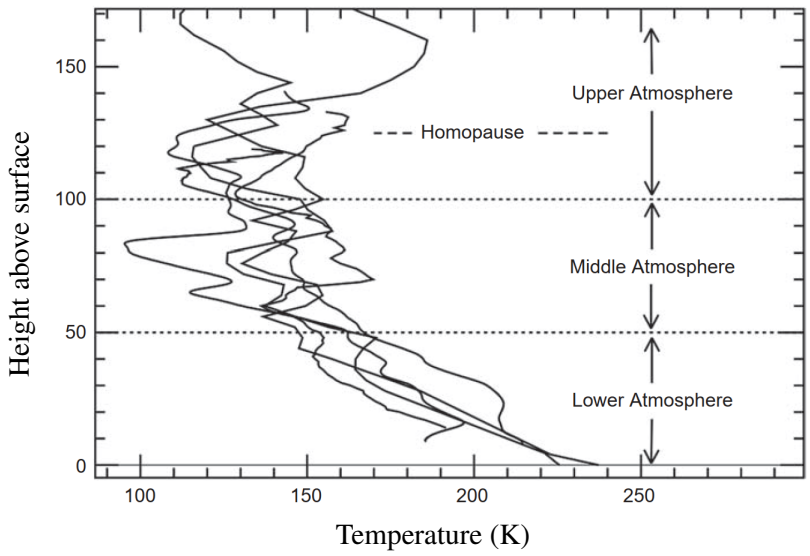

Figure 2.4: Overview of Mars atmosphere thermal structure, defining the "lower", "middle", and "upper" atmosphere. The temperature profiles shown are inferred from accelerometer observations during the descent through the atmosphere of landed spacecraft. Source: (Smith et al., 2017).

In the part of the atmosphere closest to the surface (the planetary boundary layer) a daily cycle controls the temperature (Smith et al., 2017): just before sunrise the atmosphere is cooled and stratified;

the sun heats the surface which heats the atmosphere from bellow creating a temperature gradient (super-adiabatic in the lowest $100m$), turbulent convections starts and remains until the afternoon, as the solar insolation decreases so does the surface temperature, eventually it becomes cooler than the air above it (turning off the convection) and the temperature gradient is reversed. This inversion layers grow through the night and can reach altitudes of $\approx 1km$ (Smith, 2008).

Similarly to Earth's mesosphere, the middle atmosphere is a bounded layer ($\approx 50 - 100km$) where temperature generally decreases with altitude. This part of the atmosphere is plagued by traveling waves associated with the thermal tides, which at great heights (low densities) have increased amplitudes (and can create super adiabatic lapse rates) which can act as powerful drivers of the atmospheric dynamics (Smith et al., 2017). One effect is the amplification of dowelling which can strengthen a Hadley circulation and increase the adiabatic heating of the poles.

The upper atmosphere starts at the end of the middle atmosphere ($\approx 100km$) and ends at the base of the exosphere ($\approx 150 - 200km$). It includes the Martian homopause at around $125km$ of altitude. Equivalently to Earth's thermosphere, it is thermally controlled by the absorption of solar far and extreme ultraviolet radiation which creates a positive lapse rate in this layer.

Several factors contribute to the energy balance of Mars' thermosphere. Heating due to absorption of ultraviolet and extreme ultraviolet radiation at high altitudes creates a positive temperature gradient. Molecular conduction (downwards) mitigates the thermal amplitude and CO_2 $15\mu m$ emission cooling occurs. Heat transport and redistribution by the action of global winds is also a relevant mechanism. These winds maintain the temperature stable but have some variability, particularly due to gravity waves, thermal tides and dust storms (Bougher et al., 2017).

2.3 Clouds

Clouds are relatively common on Mars but due to the very low temperature and pressure (as compared to earth) they are made of water ice instead of liquid. These atmospheric conditions are at their most extreme during the polar night and can even lead to the formation of CO_2 ice clouds. The Martian water clouds are associated with larger circulations and as such usually display a cirrus form. While H_2O clouds' latent heat release is negligible for the convective forcing, its radiative effects can alter the thermal structure. CO_2 clouds' latent heat release, on the other hand, is relevant since combined with its radiative effects it acts to mitigate the temperature difference between the winter pole and the rest of the atmosphere.

The scheme above (see Figure 2.5) was used by several authors to try to unambiguously classify every cloud feature from Mariner 9 or the Viking Orbiters (French et al., 1981; Kahn, 1983). It allows for a clear classification of Martian clouds based on observable properties.

Lee waves are composed of several ridges of cloud (see Figure 2.6 (a)) that occur on the lee side of elevated topographic features at altitudes of approximately $10 - 20km$. They are most common in the southern hemisphere during the aphelion season. Wave clouds are formed by linear clouds in a row (see Figure 2.6 (d)) at altitudes of around $5 - 15km$. Their incidence is greatest in the aphelion season

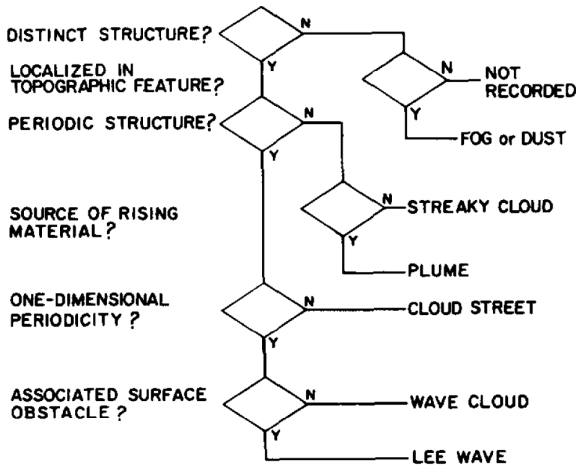

Figure 2.5: Cloud keying scheme. Source: French et al. (1981).

in middle to high latitudes and the Tharsis region. Cloud streets contain row cumulus-like clouds with double periodicity. They occur mostly on the north pole during aphelion season and over Tharsis and Syria Planum regions throughout the late aphelion season. Plumes are stretched out clouds that spread in a certain direction indicating rising material (probable dust) (see Figure 2.6 (b)). They favor the southern hemisphere during the perihelion season. Streaky clouds have well defined streaked features (see Figure 2.6), occur at approximately $10 - 30km$ and are less common in the early perihelion season. Fog involves all clouds that do not have a form (see Figure 2.6) and is common in depressed topographic features ($\approx 0 - 5km$ of altitude).

The global distribution of water ice clouds has been relatively well studied and there are some important annually recurrent cloud occurrences. The aphelion/tropical cloud belt is a mostly continuous row of several types of clouds that occurs roughly in the tropical region during the aphelion season at altitudes of $10 - 40km$. The polar hoods are the collection of mostly cirrus clouds that form at high latitudes during the hemisphere's winter when the temperatures are very cold.

The tropical cloud belt is composed of mostly optically thin clouds but it also contains a small portion of orographic clouds ($\tau_{visible} \approx 0.5$ on average) which, as opposed to the rest of the clouds, does not dissipate in the southern summer. It forms as a result of low (below $10km$) water vapor saturation altitude due to lack of dust and cold temperatures (a consequence of the orbital season) which couples with the northern summer "Hadley" circulation to create this cloud belt (Clancy et al., 1996). This belt is not symmetrical as it extends from around $10°$ S to $20° - 30°$ N, which may result from the cloud formation being stronger in the upward advection regions of the "Hadley" circulation (Clancy et al., 2017);

Polar hoods (north and south) form around the winter seasons as a result of very cold atmospheric temperatures and generally associated with storm systems, streak clouds, and lee clouds. While these are binary features and do have similarities, they are not symmetrical.

The north polar hood (NPH) is more prominent than the south polar hood (SPH) due to the greater availability of water vapor. The NPH starts forming at approximately $L_s = 150°$ and starts dissipating at around $L_s = 30°$, generally having a stationary wave number two pattern. Local and regional dust storms and subsequent dust clouds are also common in the late northern summer at mid-to-high latitudes.

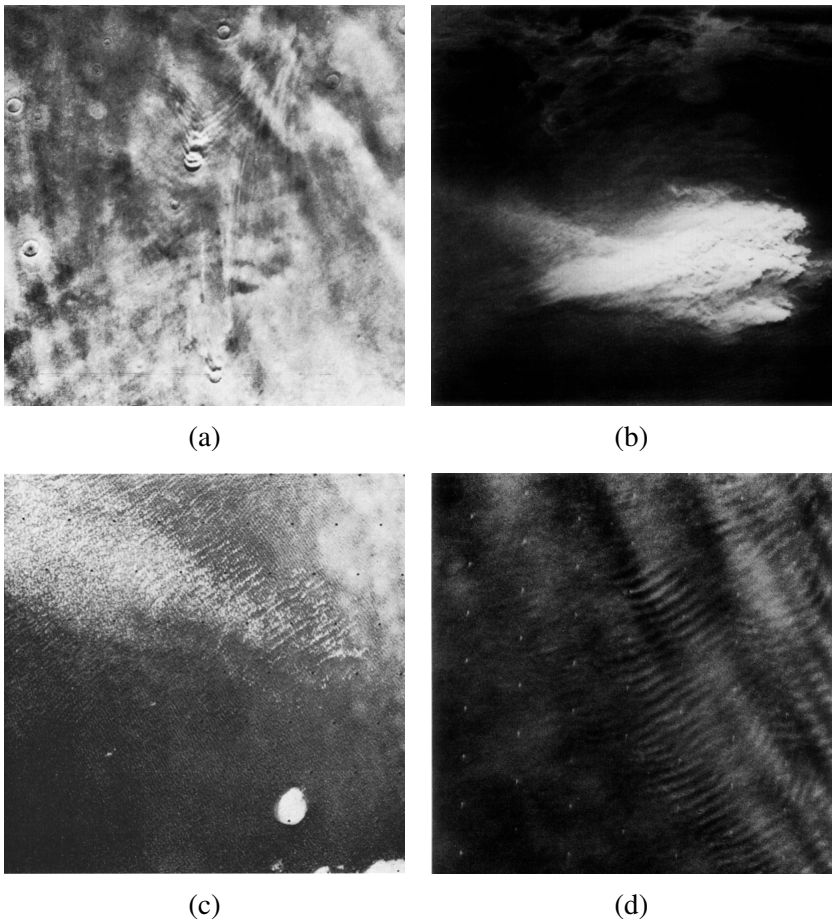

Figure 2.6: Examples of cloud types: (a) Lee waves, streak clouds, and thin and moderate haze in northern high latitudes during late summer and early autumn (Viking Orbiter picture 840A16). (b) Plume (Viking Orbiter picture 211B24). (c) Cloud streets and moderate haze in high northern latitudes during midsummer (Viking Orbiter picture 062B53. (d) Wave clouds (Viking Orbiter picture 201B61). Source: Compilation from French et al. (1981); Kahn (1983).

The lower atmospheric temperature during night-time increases condensation rates and allows the NPH to extend further south (can reach $\approx 25^\circ$ N) than during the day and at times this can even lead to a greater visible optical depth (Clancy et al., 2017).

The SPH starts to form around $L_s = 340^\circ$ and is present until approximately $L_s = 70^\circ$ and again between $L_s \approx 100^\circ - 200^\circ$. It has the form of an annulus for most of the time that it is present and it is divided into an upper layer who's altitude ($25 - 35km$) is controlled by the condensation temperature altitude (which varies with the diurnal tides) and a low lying layer ($\approx 10km$).

Figure 2.7 shows the Martian water ice cloud latitudinal and seasonal distribution for several Mars years. There is very little interannual variability of water ice clouds on Mars. Most of the variation that does happen occurs as a consequence of increased dust loading due to the occurrence of regional-to-global dust storms. This is strongly related to the remarkable repeatability of the tropical cloud belt as the dust opacity is very stable in the aphelion season (Kloos, Moores, Whiteway, & Aggarwal, 2018). The polar hood clouds are influenced by these dust events, this subject will be further discussed in section 2.4.4.

The condensation of the main constituent of an atmosphere to form clouds is an almost unique (in

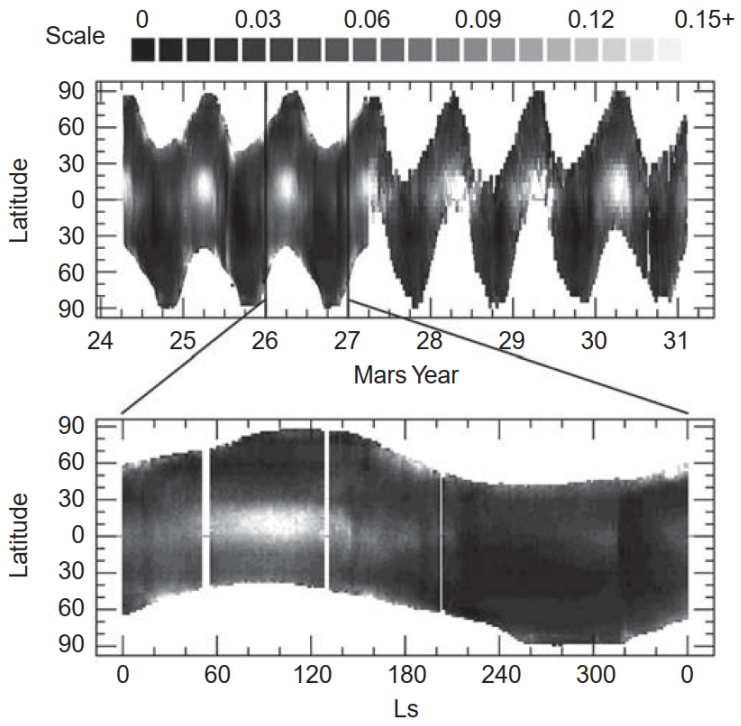

Figure 2.7: The global (zonally averaged) distribution of $12\mu m$ cloud absorption optical depth is presented versus latitude and L_s for multiple Mars years, corresponding to the 1999–2011 period. The period MY 26 is expanded for better viewing of a typical annual behavior. The period MY 24–26 incorporates MGS TES measurements (Smith, 2004), whereas the period MY 27–31 incorporates MO THEMIS measurements (Smith, 2009). The aphelion cloud belt and polar hood cloud structures apparent in this figure exhibit modest inter-annual variations. Source: Clancy et al. (2017).

the solar system) atmospheric feature that is found on Mars. CO_2 ice clouds are present in the polar winter and the tropics at mesospheric altitudes ($> 50km$) where temperatures can reach sufficiently low values to freeze CO_2. Mesospheric clouds form essentially by homogeneous nucleation while polar clouds may also form by condensing onto thin dust particles or water (heterogeneous nucleation). The mesospheric clouds are spatially restricted within tropical latitudes ($\approx 15°S - 20°N$) and the longitude range $-100°E - 23°E$ and seasonally bound to the early-to-mid aphelion season ($9° - 135°$) (Aoki et al., 2016).

The water ice clouds are composed of particles of $R_{eff} \approx 1 - 2\mu m$ and do contribute to the thermal balance of the atmosphere. By absorbing thermal infra-red radiation (emitted by the surface during the night) and re-emitting it they can warm the atmosphere and create inversion layers in the tropics or cool it, in the poles, by emitting to space. Thus ice water clouds contribute to a smaller temperature gradient between the polar and equatorial regions. While the effect of latent heat release from H_2O ice clouds is negligible they may have a relevant role in the redistribution of aerosols like water and dust (Colaprete & Toon, 2000). CO_2 clouds' latent heat release, on the other hand, is important in counterbalancing the radiative cooling of the atmosphere in the polar night.

2.4 Climate

Mars' climate is a consequence of the coupling of three important cycles, of water, carbon dioxide and dust, with radiative and dynamical processes. These cycles use atmospheric processes to exchange material in between reservoirs. While CO_2 is the primary driver of the Martian climate, all three cycles are interconnected and can have a remarkable influence on each other.

2.4.1 Carbon Dioxide Cycle

Carbon dioxide on Mars follows a cycle of condensation and sublimation at the winter and summer poles, respectively, which is primarily controlled by isolation - that can vary by $\approx 40\%$ between aphelion and perihelion (R. W. Zurek, 2017). The exchange between these two reservoirs, caps and atmosphere, results in the growth and recession of the winter and summer polar caps respectively and the variation of the total atmospheric mass by $\approx 30\%$. The surface pressure also varies (a consequence of the atmospheric mass variation) as we've seen in Figure 2.2. This variation is semi-annual as the cycle evolves in an opposite fashion, meaning that as the northern polar cap is advancing, in the northern winter, the southern polar cap is receding and vice versa.

This cycle is distinctively asymmetrical as Mars' orbital eccentricity confers distinct durations for equivalent seasons in opposite hemispheres (southern summer is longer than the northern summer). This results in the conditions for condensation prolonging themselves in time during the northern winter which results in more CO_2 being condensed.

At the heart of the CO_2 annual cycle is the energy balance at the poles, and it is that balance that determines the polar condensation and sublimation rates. A simple but elucidative model is presented in Paige and Ingersoll (1985):

$$F_\gamma + F_{Hor} + F_{Cond} = S_{Atm} + S_{\mathrm{CO_2}} \tag{2.1}$$

Here F_γ represents the net flux of solar and infra-red radiation at the top of the atmosphere, F_{Hor} is the net horizontal heat flux at the boundaries, F_{Cond} is the net vertical heat conduction, S_{Atm} is the rate of total potential energy stored in the regional atmospheric columns and $S_{\mathrm{CO_2}}$ is the rate of latent heat storage in condensing or sublimating CO_2 condensates in the region.

This equation rests on the importance of the CO_2 heat storage term:

$$S_{\mathrm{CO_2}} = -L_{\mathrm{CO_2}} \frac{dM_{\mathrm{CO_2}}}{dt} \tag{2.2}$$

$L_{\mathrm{CO_2}}$ is the CO_2 latent heat sublimation term, and $\frac{dM_{\mathrm{CO_2}}}{dt}$ is the net rate of solid CO_2 accumulation within the region of study.

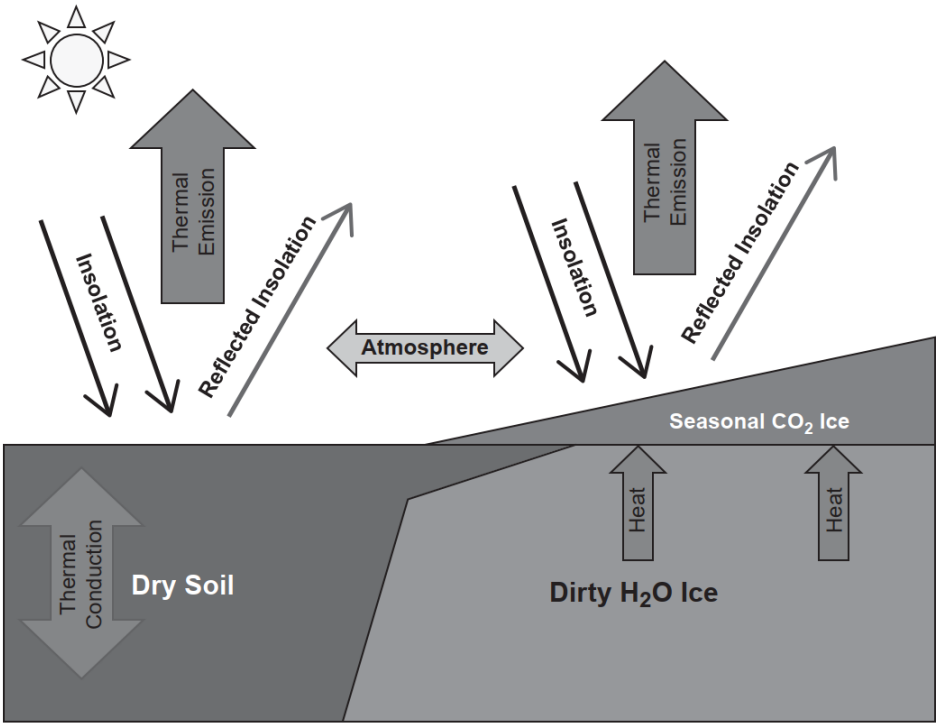

Figure 2.8: Polar energy balance cartoon. The thin black arrows are the solar energy, which is either absorbed or reflected (thin gray arrows) back into space. The two thick open arrows pointing up are the radiative heat loss to space. The thick open arrows in the regolith are the heat conduction and the release of the stored solar heat back into surface ice. The sideways arrow is the heat transported by the atmosphere. Source: Titus et al. (2017).

$$\frac{dM_{\mathrm{CO_2}}}{dt} = \frac{1}{L_{\mathrm{CO_2}}}\epsilon\sigma T^4 - (1 - A_p)F_{solar} \tag{2.3}$$

Here, A_p represents the planetary albedo, ϵ is the surface ice emissivity and T is the temperature. $\epsilon\sigma T^4$ represents the outward flux of emitted radiation at the top of the atmosphere.

Figure 2.8 represents this model. The surface ice emissivity and the planetary albedo, which can be modified by clouds and dust (aerosols), affect how CO_2 ice accumulates. Hence it becomes clear the crucial role of both parameters on the deposition and removal of dry ice in the poles. There are, however, several other properties that influence this cycle.

The surface albedo and surface ice emissivity, in particular, have crucial roles as the albedo controls the sublimation rate and emissivity regulates the condensation rate (Paige & Ingersoll, 1985; Kahre & Haberle, 2010). Both these properties are affected by the presence of dust both on the surface, which increases the emissivity and decreases the albedo, and airborne which can act to increase the atmospheric condensation and subsequent deposition of ice through snowfall (Pollack, Haberle, Schaeffer, & Lee, 1990) which also acts as an atmospheric dust removal mechanism. Furthermore, both the albedo and the emissivity are highly dependent on composition and grain size.

There are two phases of each poles' annual cycle: The waning and the waxing.

The polar night is the least well understood polar period as it is both faced away from the sun and covered by a seasonal H_2O polar hood which limits our observational ability. Nevertheless, it is an important part of the cycle as it is during this period that atmospheric conditions allow for the condensation of CO_2 to occur and subsequent waxing of the polar cap. This cap growth occurs both by direct condensation onto the surface and atmospheric condensation followed by snowfall. The low pressure caused by the loss of CO_2 creates a polar vortex that restricts meridional atmospheric transport in the lower atmosphere (Titus et al., 2017). In the southern polar regions, this significantly increases the abundance of non-condensible gases. Above the lower atmosphere, latitudinal transport is no longer inhibited by the polar vortex which allows for dust (arising from global dust storms) to reach the poles. Airborne dust may be important at the poles in providing nuclei for heterogeneous nucleation.

In the summer season, the caps recede as a direct response to solar insolation. One of the global consequences of this comes from the conservation of angular momentum which demands the increase of the planetary rotation speed. In the north pole the whole CO_2 cap, which is tracked in its edges by a water annulus, sublimates leaving behind an underlying water ice cap (the northern residual cap). This residual cap will then interact with the atmosphere in the annual water cycle. The southern residual cap, on the other hand, is composed of CO_2 ice (Haberle, Clancy, Forget, Smith, & Zurek, 2017).

Table 2.5: CO_2 reservoirs and the relative size of the reservoir compared to the current size of the atmosphere. Source: (Titus et al., 2017).

Reservoir	**Amount (%)**	**Reference**
Seasonal caps	≈ 25	Leighton R. and Murray B. (1966), Tillman J. et al. (1993), Kelly E. (2006)
South polar residual cap	≈ 3	Byrne S. and Ingersoll I. (2003), Bibring J. et al. (2004), Thomas P. et al. (2009)
Buried south polar CO_2 ice	≈ 80	Phillips R. et al. (2011)
Adsorbed within regolith	$\approx 100 - 1000$	Fanale F. and J. Salvail (1994), Manning C. et al. (2006)
Clathrates in polar layered deposits	≈ 0	Mellon M. (1996), Nye J. et al. (2000)
Carbonates		

The structure of the poles is quite complex. Both polar caps sit on layered deposits which are composed of layers of a mix of dust (lest than $\approx 5\%$ according to Grima et al. (2009)) and water ice (several kilometers in depth). Between this deposit and the southern residual caps, there is a thin water-ice layer which stands on top of a CO_2 deposit with a volume of $\approx 9500 - 12,500 km^3$ and a thickness of a few hundred meters which would correspond to $\approx 80\%$ of the current atmosphere (Phillips et al., 2011).

This recently found buried deposit is one of the several relevant carbon dioxide reservoirs that are thought to exist (see Table 2.5). While the southern caps interact with the atmosphere on shorter time-scales, Mars' obliquity variation allows for different reservoirs to interact with the atmosphere on longer time-scales. The buried CO_2 deposit is thought to have interacted with the atmosphere somewhere in the past $600,000$ years (Phillips et al., 2011). Carbonates are present in surface rocks but their contribution to the current cycle is negligible. Apart from these, there are two unconfirmed reservoirs: it is possible that a large amount of CO_2 has been absorbed by regolith grains and CO_2 clathrates could have been stored in the polar layered deposits in a minimal amount (Titus et al., 2017).

The southern residual cap is the few meters thick layers of a high albedo CO_2 ice that persists throughout the summer after the retreat of the seasonal cap and contains $\approx 3\%$ of the current atmosphere. It distances around $200km$ from the pole as it sits on the topographically highest point of the south pole. It is only able to survive during the southern summer by maintaining a high albedo throughout the season. This does not always happen as lower albedo regions can occur (particularly at the edges), defrosting the ice and revealing the underlying water ice layer. The exposure of lower layers can be critical as stored heat can reduce the condensation in winter and ensure the defrosting of the CO_2 on the following summer. It remains unclear whether the cap has significant interannual variability but it is possible that it is disappearing, maybe even in a cyclic fashion (Titus et al., 2017).

2.4.2 Water Cycle

The Martian northern summer is characterized by the waning of the CO_2 cap at the pole, leaving behind a perennial water ice cap that is then able to interact with the atmosphere. Sublimation of the perennial cap sets off the year-long Martian hydrological cycle. The water cycle is perhaps the least understood of all three (dust, water, and carbon dioxide) but it is nothing more than a sequence of exchanges between different water reservoirs, each with its consequences and effects on the global climate. These reservoirs fall into three different categories: atmospheric, surface, and subsurface.

The atmospheric reservoir contains both water ice clouds ($\approx 15\%$) and water vapor ($\approx 85\%$). The surface holds most of the water on Mars, its main deposits include the perennial polar caps ($\approx 67\%$ of Martian global inventory of water), the polar layered deposits and some southern (winter) mid-latitude deposits mostly associated with topography. Water is stored underground first and foremost as ground ice (believed to be ubiquitous at middle to high latitudes), vapor and liquid.

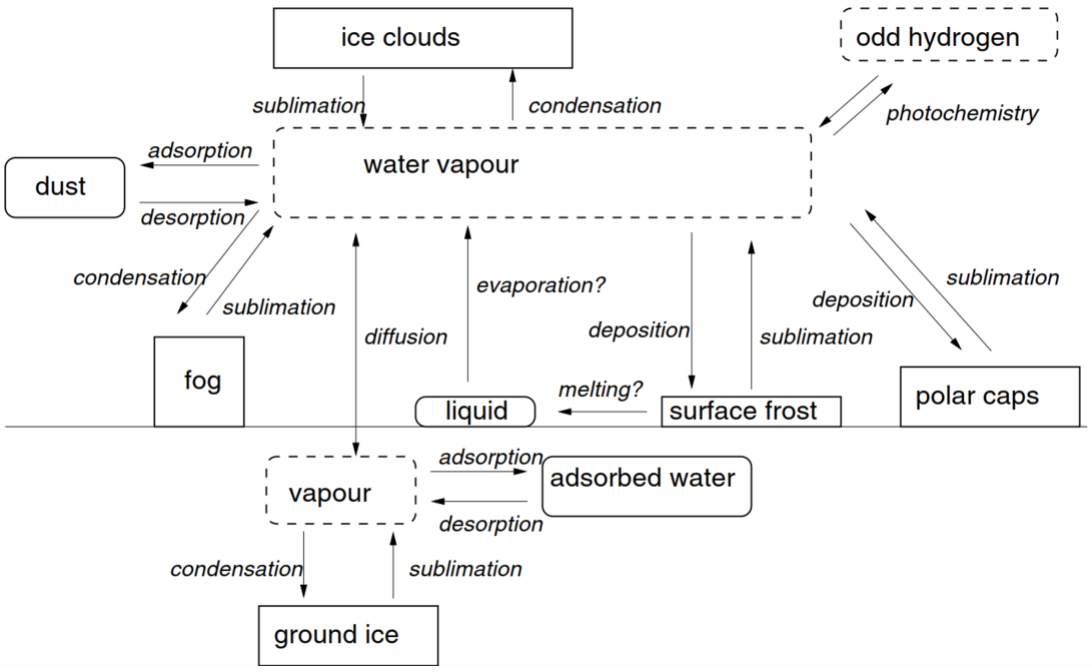

Figure 2.9: Schematic diagram showing the different reservoirs of exchangeable water in the atmosphere and shallow subsurface as well as the fluxes between them. Source: Tokano (2005).

The surface reservoir includes both perennial polar caps however these are non-identical. While the northern water ice perennial cap becomes largely exposed during summer after the sublimation of the CO_2 seasonal cap, the southern perennial cap remains predominately covered by a thin layer ($< 3m$) of carbon dioxide ice for almost its entire summer season which prevents it from efficiently interacting with the atmosphere (Montmessin, Smith, Langevin, Mellon, & Fedorova, 2017). Furthermore, the southern cap is much smaller in areal extent. It is then no surprise that the dominant contribution to the hydrological cycle comes from the northern cap.

It is worth noting that there are some water ice deposits in the CO_2 dominated southern cap which are thought to be associated with subsurface water ice. Furthermore, recent radar observations have found a shallow lying stable liquid water body under the south polar layered deposit (Orosei et al., 2018).

Due to the cold temperatures, the top few kilometers of the Martian surface have frozen, having temperatures well under $0°C$. Subsurface water can be trapped in the pores (in the solid or gaseous form), adsorbed by coating individual grains soil (the negatively charged mineral grains attract dipolar water molecules) or chemically bound within minerals. Despite having the lower relative abundance of the three phases, the vapor is detrimental in diffusing into the top meters of the regolith and collect as adsorbate or ground ice (Mellon & Jakosky, 1993). The ground ice is geologically young ($< 500kyr$) and is located where stability conditions are or have been met, being present from middle latitudes to the pole with increasing depth (Mellon, Feldman, & Prettyman, 2004).

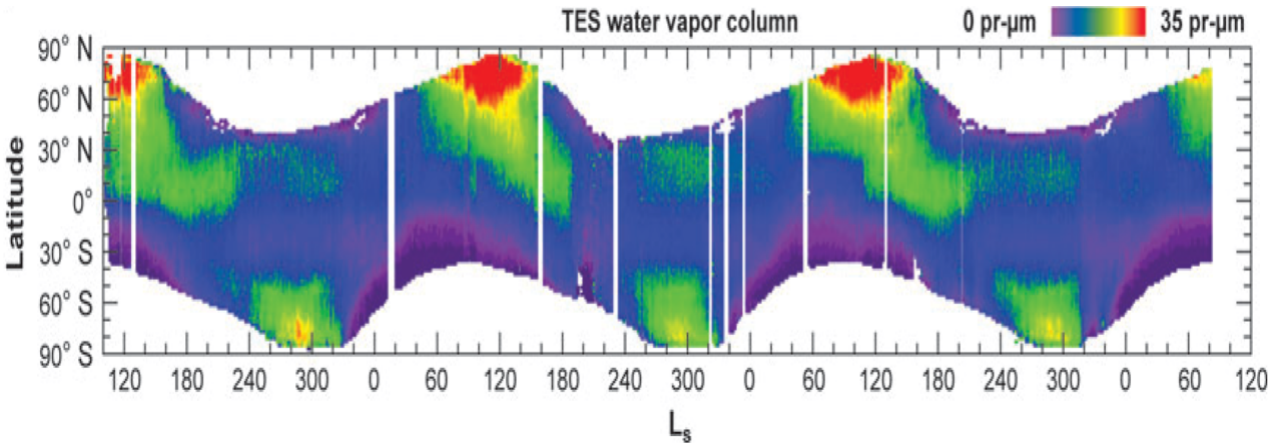

Figure 2.10: An overview of TES atmospheric daytime observations showing the seasonal and latitudinal variation of water vapor column abundance in precipitable microns. Source: (Smith, 2008).

The cyclic manner in which the atmospheric water behaves on Mars stands out in Figure 2.10. There is little inter-annual variability on both the distribution of water vapor and on the water cycle itself. Seasonally, according to Smith (2002), the cycle evolves in the following fashion: from $L_s \approx 40°$ to $L_s \approx 110° - 120°$ the north polar water cap sublimates leading to the highest annual atmospheric water abundance; from $L_s \approx 120° - 170°$ the vapor is transported to equatorial latitudes creating a monotonic decrease in the abundance in the northern pole and gradually increasing the southern hemisphere water content; the southern hemisphere's water content increases until maximum abundance occurs at the pole around $L_s = 290°$ (early southern summer); After $L_s \approx 300°$ the southern hemisphere starts losing water to the northern and shortly after condensation at the pole begins, leading to a global decrease in abundance, this situation endures until $L_s \approx 40°$ when sublimation of the northern cap restarts.

It is noteworthy the evident asymmetry between hemispheres that Figure 2.10 shows. First of all the southern hemisphere has a much lower annual mean atmospheric water abundance, secondly, the maximum abundances for both hemispheres differ by a factor of ≈ 2 and thirdly the southern hemisphere shows a lower minimum. Furthermore, we've already seen that the southern water cap is much smaller as a consequence of the orbital configuration of Mars which does not favor the stability of a summer exposed water ice cap (Richardson & Wilson, 2002). All these act to further enhance the hemispheric dichotomy.

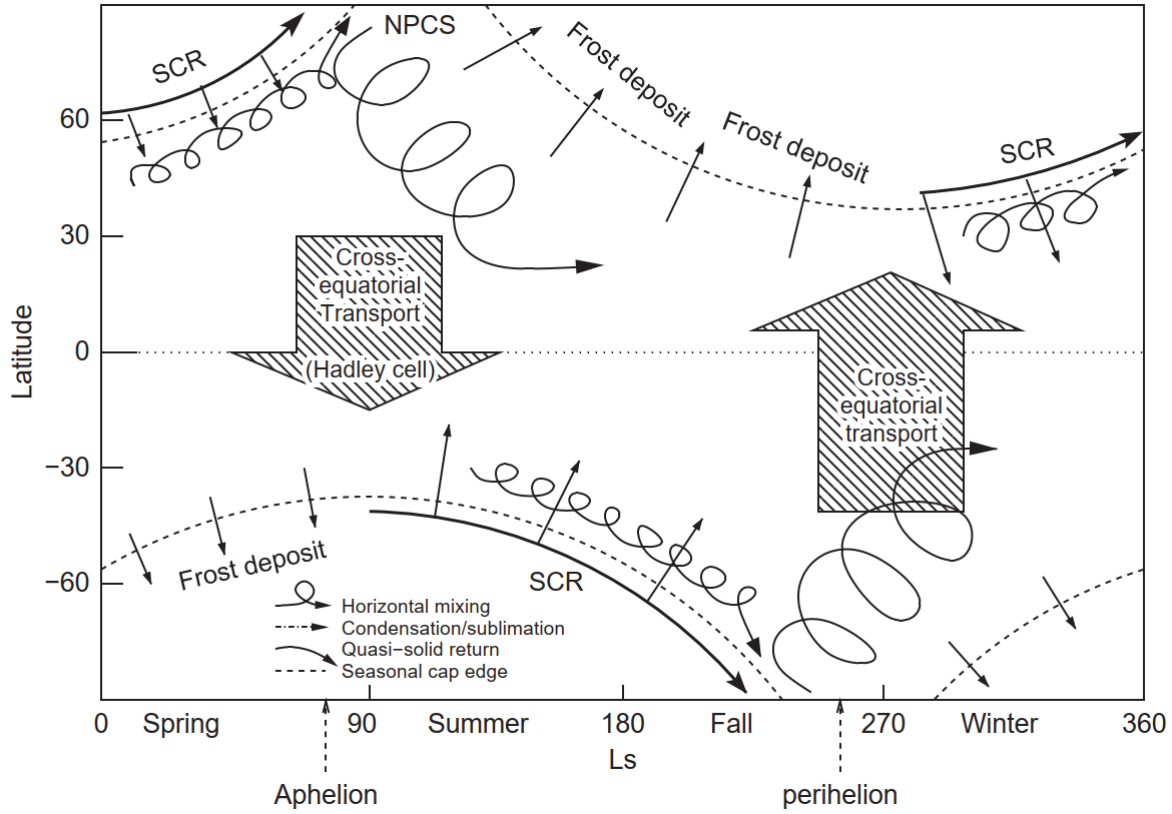

Figure 2.11: Chart describing the principal events affecting the Martian water cycle over the course of a year. NPCS stands for North Polar Cap Sublimation; SCR stands for Seasonal Cap Recession. Source: (Montmessin et al., 2004).

The water cycle has two important features that are worthy of further characterization: the sublimation of the caps and water transport.

The sublimation of the caps is a reaction to polar isolation, which is the primary driver of the water cycle. Thus waning starts to occur in late winter and lasts through early spring on both hemispheres. Through fall and winter, the circulation at the poles is dominated by a vortex. The recession occurs through successive sublimation, transport to higher latitudes and re-condensation (Houben, Haberle, Young, & Zent, 1997) which is possible by the polar vortex ability to allow intrusions of H_2O vapor rich air. This is how high southern latitudes achieve high water abundances without actually having a significant water reservoir. An observable consequence of the sublimation-condensation process is the ice annulus that surrounds the retreat of the season north polar cap (that grows in thickness until the 'ultimate' sublimation event) along with the elevated atmospheric abundance of water over the edges of the cap (Khayat, Smith, & Guzewich, 2019). This annulus has no parallel in the waning of the southern seasonal cap.

The latter mechanism means that when the recession phase is concluded most of the sublimated water will be at very high latitudes. The transport of water from the pole to lower latitudes is accomplished by several mechanisms. First and foremost the wave-3 polar circulation that develops in summer forced by both topography and thermal inertia variation allows meridional/longitudinal mixing in the three-wave regions (where transient eddy activity is enhanced). The pressure gradient created by the waning of the seasonal CO_2 cap induces a transport flux towards lower latitudes. Finally, a sea breeze circulation that develops near the edge of the cap also contributes to the equator-ward transport of water. It is worth noting that around this period in the north, a transient eddy located at mid-latitudes returns some of the sublimed water to the pole, restricting water transport to the south.

Further restriction of water transport to the southern hemisphere comes as a consequence of the effect described by Clancy et al. (1996): aphelion conditions place the water saturation level bellow the southward branch of the single-cell Hadley circulation that dominates in the summer. Above this level the water vapor condenses into clouds, creating the aphelion cloud belt described in the cloud section. Water ice clouds are essential, as they represent the main form in which water is transported across equatorial latitudes.

Nearly all mechanisms and effects we've discussed contribute to the hemisphere asymmetry. The global circulation allied with atmospheric conditions clearly favors tracer transport to the north. Furthermore, the perihelion conditions are much warmer (than aphelion) and ensure all exposed water ice sublimates and consequently has a better chance of getting transported elsewhere. All these factors result in an overall water abundance bias towards the northern hemisphere.

2.4.3 General Circulation

Our current understanding of Mars' global circulation comes mainly from global circulation models (GCM's). Its primary drivers of the Martian circulation are heat and momentum transfers between the atmosphere and surface. These exchanges are largely determined by three surface properties: albedo, thermal inertia, and topography.

Thermal forcing is essential to Mars' climate. The albedo determines how much radiation is absorbed by the surface while the thermal inertia defines how fast the energy is lost and both regulate the temperature of the surface. Sensible heat exchange between the surface and the atmosphere induced by turbulence contributes to the forcing of the lower atmosphere. Latent heat release from CO_2 is relevant, particularly at the poles where carbon dioxide condenses and sublimates.

However, it is radiative forcing that dominates on a global scale (Barnes et al., 2017). Globally the Martian atmosphere can be thought of as in radiative equilibrium since its radiative relaxation time is very short ($\approx 1day$). The $\approx 95\%$ CO_2 composed atmosphere is approximately transparent to visible radiation however allowing the radiation to reach and be absorbed by the surface which re-emits it in the thermal infrared. Carbon dioxide absorbs well in that range so the atmosphere is heated from below. Further radiative forcing occurs when aerosols like dust (highly absorbent in both the visible and the infra-red ranges) or water vapor are present in significant amounts. Since dust loading is considerably increased during the perihelion season (as is insolation), the southern summer atmosphere circulation is

stronger than its northern counterpart.

Topography has a significant influence on the circulation as well. Both surface wind stress and mountain torque are common mechanisms of momentum transfer on Mars. Furthermore, some topographic features can even create gravity waves. The topography differences between hemispheres (see Figure 2.2) contribute to further increase the hemispheric contrast of the summer circulation.

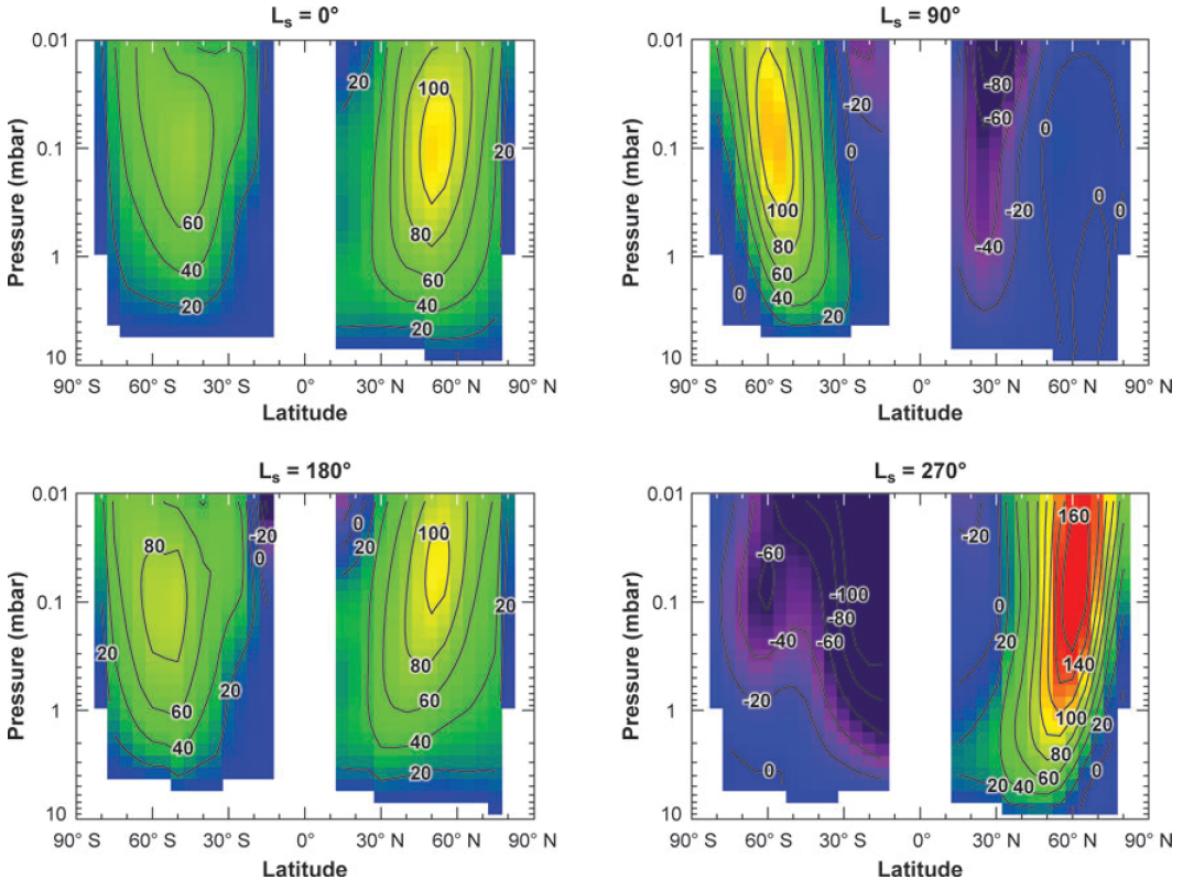

Figure 2.12: Mean daytime ($\approx 02:00pm$ local-time) zonal wind speed as a function of latitude and pressure (or height above the surface) as observed by TES (Thermal Emission Spectrometer instrument aboard the Mars Global Surveyor spacecraft) using the gradient wind approximation. Wind speeds are given in meters per second, with positive values indicating a wind blowing from west to east. Source: Smith (2008).

The global data set of measured winds on Mars is partial at best. Direct measurements of Martian winds are few and lack spatial, temporal and altitude coverage. There have been mainly four types of direct wind measurements performed until now:

– **In-Situ Measurements:** Wind measurements performed by landers like Viking Landers 1 and 2, Pathfinder, Phoenix and Mars Science Laboratory (Hess, Henry, Leovy, Ryan, & Tillman, 1977; Holstein-Rathlou et al., 2010; Schofield et al., 1997; Viúdez-Moreiras et al., 2019). Although they allow for continuous temporal coverage, they are limited to fixed locations. Furthermore, these measurements are restricted to near-surface winds which are largely determined by topography and surface properties and therefore may not reflect the global circulation pattern.

– **Cloud Tracking:** By using orbiting telescopes like the Hubble Space Telescope (Mischna, Bell, James, & Crisp, 1998; Kaydash et al., 2006) or instruments aboard orbiters (Wang & Ingersoll,

2003; Määttänen et al., 2010; McConnochie et al., 2010) to track cloud features we can measure wind velocities and directions. These provide us with the synoptic-scale general circulation pattern. They suffer from problems affecting all earth and orbiter based observations like, respectively, bias towards observations during opposition and lack of either local time coverage (sun-synchronous orbit) or daily global coverage. Additionally, the sparse cloud coverage and the difficulty associated with the determination of the altitude of the observed clouds add further complexity to this method.

– **Heterodyne Doppler Measurements:** By using carbon monoxide transition lines from ground-based telescopes (Lellouch, Goldstein, Bougher, Paubert, & Rosenqvist, 1991; Clancy, Sandor, Moriarty-Schieven, & Smith, 2006; Sonnabend, Sornig, Krötz, Schieder, & Fast, 2006; Cavalié et al., 2008; Moreno et al., 2009; Sonnabend, Sornig, Kroetz, & Stupar, 2012) we can obtain wind velocities at certain pressure levels. Once again these observations are seasonally biased as they require high resolution and consequently are taken close to the opposition. Also, they are limited to the middle atmosphere and therefore lack altitude coverage.

Despite all the limitations and complexity associated with direct wind measurements, these are extremely useful as they provide constraints for global circulation models which give us an overall picture of the Martian circulation. It is worth noting that there several other proxies for determining the wind fields like geological features' orientation (Kahn, 1983) or aero-braking measurements (Baird, 2006).

It is possible to derive wind speeds by considering some approximations. By considering a gradient wind which assumes the force excreted by the pressure gradient is in balance with both the Coriolis force and the centrifugal force. This, however, requires a boundary condition on the zonal wind speed which is assumed to be negligible at the surface. Using thermal data we can then estimate the zonal mean zonal winds (Figure 2.12).

The zonally averaged meridional circulation is, for most of the year, characterized by single-cell Hadley ($\approx 90°$ in extension) circulation that reverses itself around the equinoxes. Any Hadley circulation is driven by temperature gradients - low lying warm air rises and cold air drops creating pressure gradients which then move the air masses latitudinally - but Mars' low thermal inertia ensures the lower atmosphere maximum temperature is always found near sub solar latitudes (see Figure 2.14). This feature is responsible for the existence of opposite circulations during summer and winter (see Figure 2.13). Both Hadley cells are generally restricted to altitudes above $4km$ (see Figure2.13). The southern summer (perihelion $L_s \approx 270°$) cell is the strongest (see Figure 2.13) as a consequence of the greater thermal gradient (see Figure 2.14) caused by the increase in insolation. Very close to the equinoxes the zonal mean meridional winds assume an earth-like form with a weaker double Hadley cell circulation (see Figure 2.13).

The lower level of the Hadley circulation is not longitudinally uniform as is the upper branch. There are preferred cross-equatorial winds corridors - forced largely by topography - that are called western boundary currents.

The zonal circulation is composed by approximately gradient winds. Strong westerly jets - caused by the latitudinal temperature gradient between the warm air transported by the Hadley cell to middle-to-high latitudes and the cold polar night air - of $\geq 100ms^{-1}$ (Haberle et al., 1993; Smith, Pearl, Conrath,

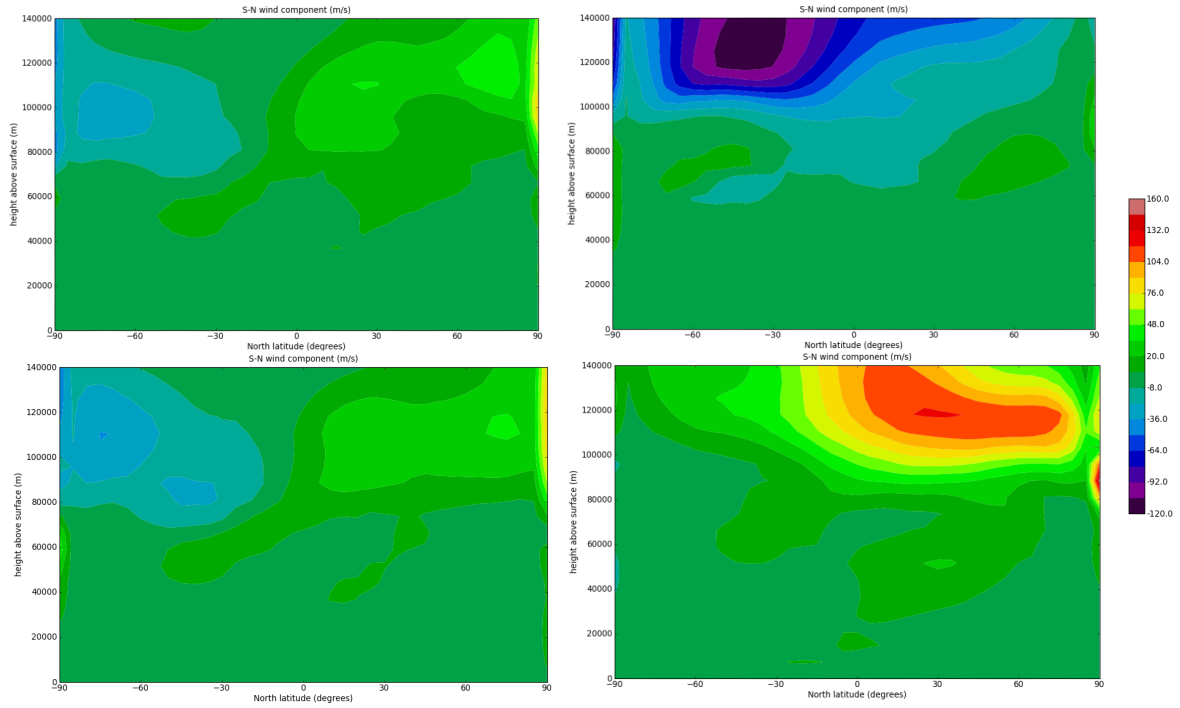

Figure 2.13: Zonally averaged meridional wind (meters per seconds) retrieved from LMD's (Laboratoire de Météorologie Dynamique) Mars Climate Database as a function of latitude (degrees) and height (meters) using the solar average climatology scenario for $L_s = 0°$, $L_s = 90°$, $L_s = 180°$ and $L_s = 270°$.

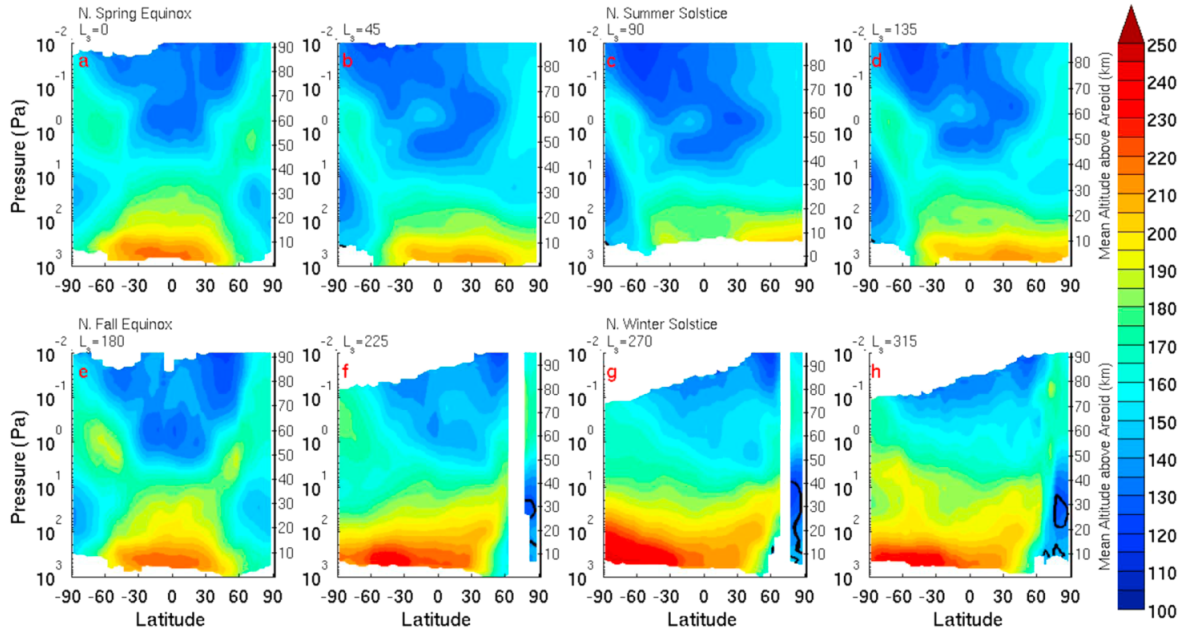

Figure 2.14: Zonally averaged temperature (Kelvin) night side retrievals of MY 29 for $L_s = 0°$, $L_s = 45°$, $L_s = 90°$, $L_s = 135°$, $L_s = 180°$, $L_s = 225°$, $L_s = 270°$ and $L_s = 315°$. Contours are every 5 K. The black contour indicates the CO2 frost point. Source: McCleese et al. (2010).

& Christensen, 2001; Smith, 2008) at middle and high latitudes are typical in the winter season in both hemispheres while weaker easterly jets of $\approx 60ms^{-1}$ (Haberle et al., 1993; Smith et al., 2001) characterize the summer hemisphere. The equator, however, is characterized by both westerly winds at lower altitudes and easterly at higher ones. The jets are stronger in the perihelion season. In equinoctial

seasons ($L_s \approx 0°, 180°$) weaker westerly jets form in both hemispheres.

Mars has a flow caused by the seasonal polar condensation and sublimation of CO_2 which is forced by the increase of the pressure gradient between the poles and lower latitudes. This flow contributes to the meridional wind a vertically averaged strength of $\leq 1ms^{-1}$ (Chow, Xiao, Chan, & Wong, 2019). However, through the action of the Coriolis force, the contribution of this flow to the zonal wind can reach values of $\approx 10 - 15ms^{-1}$ (Haberle et al., 1993).

Eddy activity is also present on Mars. It is significant in the lower atmosphere and has a more important role in the forcing of the circulation when the Hadley cell is at its weakest (Haberle et al., 1993). At $L_s = 180°$ transient eddy activity intensifies as a consequence of the baroclinic instability driven by the thermal gradient between polar and lower latitudes. This creates a low lying Ferrel cell circulation. Furthermore, there are also stationary eddies present that are essentially forced by the terrain properties as topography, thermal inertia or albedo.

2.4.4 Dust Cycle

Mars' atmosphere has a permanent layer of suspended dust. This dust is primarily composed of silicates such as gioclase, feldspar, and zeolite mixed with a much smaller portion of magnetic materials (Perko, Nelson, & Green, 2002). Figure 2.15 shows the dust optical depth and temperature for almost four Martian years. The recurrence of non-dusty ($L_s = 0° - 135°$) and dusty periods ($L_s = 135° - 360°$) in all Martian years is at the core of the dust cycle.

The martian atmosphere is extremely sensitive to the amount of dust in the atmosphere (Gierasch & Goody, 1972). Some of the consequences that increased dust loading imposes on the thermal state of the atmosphere are observable represented in Figure 2.15, the increase in temperature is a consequence of the increased dust optical depth. Airborne dust absorbs and scatters visible radiation which acts to heat itself and its surroundings. Furthermore, the heating of the atmosphere creates pressure gradients which in turn lead to winds. The dusty season on Mars has a much more vigorous circulation - the mass flux of the Hadley circulation can even double (Haberle et al., 1993).

The dust cycle has a strong impact on the water and carbon dioxide cycle. Airborne dust provides nuclei for heterogeneous nucleation, enhancing polar condensation. Furthermore, the deposition of dust on the polar caps dramatically changes the cap's emissivity and albedo, properties upon which the CO_2 sublimation and condensation rates are highly dependent (Pollack et al., 1990). These rates control the changes of the mass of the atmosphere which affect the atmosphere-surface momentum exchanges that lead to dust lifting. Similarly to what happens with CO_2, water particles use dust as seed nuclei in condensation (Brown, Wolff, & Scargle, 2015). Additionally, the presence of dust in the water ice particles significantly alters their radiative properties which affects the thermal and dynamical state of the atmosphere.

The exchange of dust between different accessible reservoirs is the mechanism that allows for the transition between different atmospheric dust loading levels. In the short-medium term, these exchanges happen, predominantly, between two reservoirs: the surface and the atmosphere. Most of the dust is

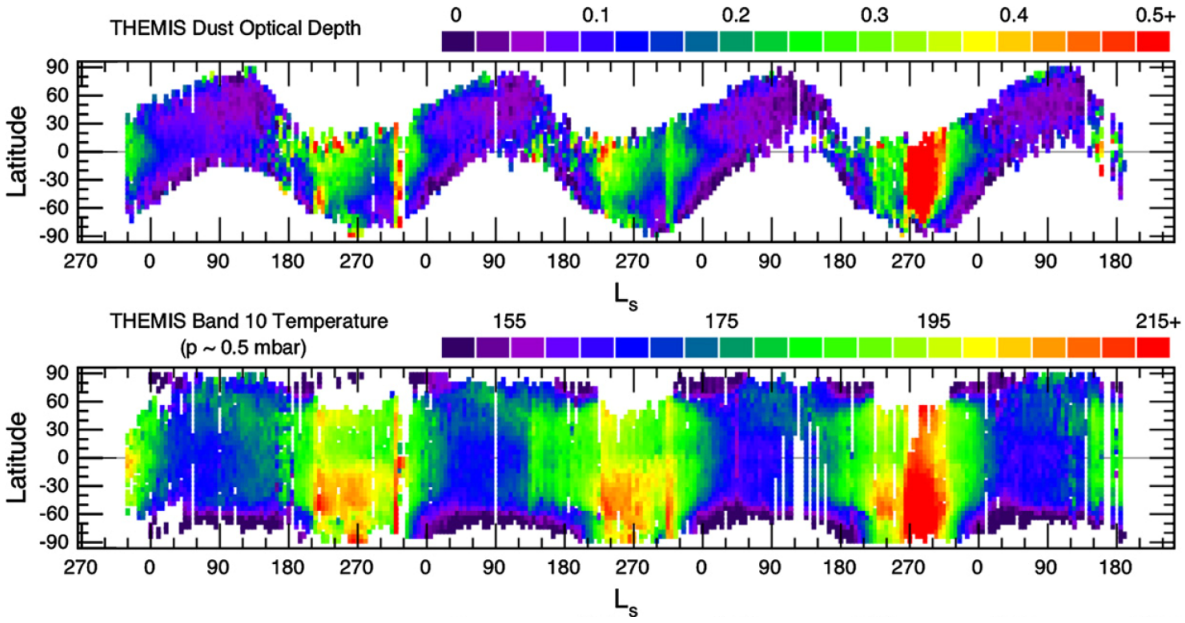

Figure 2.15: THEMIS retrieved aerosol optical depth and Band 10 temperature over ≈ 3.5 martian years. Shown is the zonal average of each quantity as a function of solar longitude (L_s) and latitude. (Top) Dust optical depth at 1075 cm-1 scaled to an equivalent 6.1-mbar pressure surface to remove the effect of topography. (Bottom) THEMIS Band 10 temperature, representative of a wide range of heights centred at about 0.5 mbar. Source: Smith (2009).

deposited in the surface in three separate regions: Tharsis ($20°S - 50°N$, $60° - 190°W$), Arabia ($5°S - 30°N$, $300° - 360°W$), Elysium ($10°N - 30°N$, $210° - 225°W$) (Christensen, 1986). A great amount of the Martian dust may have its origin in deflation and abrasion processes in the Medusae Fossae Formation (Ojha, Lewis, Karunatillake, & Schmidt, 2018). The exchanges from the surface to the atmosphere happen, fundamentally, through two dust lifting mechanisms: convective vortices (dust devils) and wind stress (Mackwell, Simon-Miller, Harder, & Bullock, 2013).

Since surface winds are generally too weak to lift dust particles, sand particles saltation is the chief contributor to the suspension of dust. By being greater in size these particles are easier to lift, however when lifted they tend to saltate and upon their return to the surface, they impart additional momentum onto the dust, allowing for its lifting (Mackwell et al., 2013). Direct suspension may also play a role, particularly in locations where sand is not abundant (Kahre et al., 2017).

Dust devils are ubiquitous on Mars, they form as a consequence of surface heating. The rising of warm air can produce an initial rotation that leads to a vertical stretching and an intensification of the rotation forming a convective vortex which is referred to as a dust devil when it incorporates dust into its form. Dust devil dust lifting is dominated by the suction, existent, as a consequence of the pressure gradient, inside the vortex (Neakrase & Greeley, 2010), however, the strong tangential winds can provide sufficient wind stress to lift relevant amounts of dust (Kahre et al., 2017). Dust devils are thought to be responsible for the background haze that is present outside the increased dust loading seasons.

The dust cycle is composed of yearly repeatable periods of higher and lower dust loading. The non-dusty season ($L_s \approx 0° - 135°$) occurs in the northern spring and summer (aphelion season) when Mars is furthest from the Sun. This period is characterized by decreased column dust opacity (see Table 2.15) and the absence of large scale dust events (Montabone et al., 2015). The dusty season is

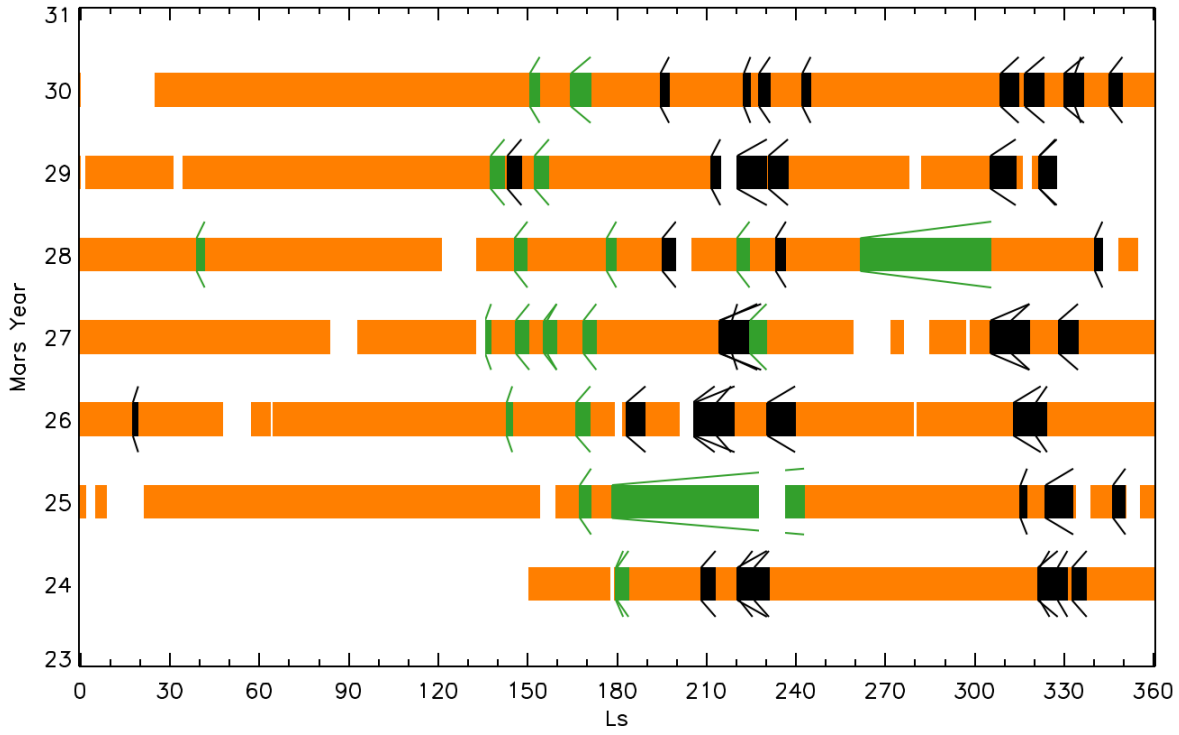

Figure 2.16: Seasonal distribution of dust storm sequences observed in MGS MOC (Mars years 24–28) and MRO MARCI (Mars years 28–30) Mars Daily Global Maps (MDGM). Periods with data but without any dust storm sequences are indicated by orange bars. Each identified sequence is indicated by a left bracket with the vertical line corresponding to the beginning and the other two sloped lines corresponding to the duration of the sequence. Each dust storm sequence is also indicated by a filled bar color-coded according to its origination hemisphere. Northern hemisphere originated sequences are in black and southern hemisphere originated sequences are in green. Source: Wang and Richardson (2015).

much more complex. It is distinguished by several different types of local-to-global dust events and a related increased overall dust loading. There are four different discernible periods - based on dust loading and dust event occurrence - within this season (Kahre et al., 2017): The $L_s \approx 135° - 180°$ period is characterized by an increase in the frequency of dust storm occurrence (see Figure 2.16) - mostly in the southern hemisphere - and consequently an increase in dust loading (see Figure 2.17). The $L_s \approx 180° - 236°$ period in which the dust loading increases further - and increases the most (Montabone et al., 2015) - as a result of the increase in dust storm activity in both hemispheres (see Figure 2.16 and Figure 2.17)) - southern storms generally lead to increased global levels of dust loading as a consequence of the type of Hadley circulation that is present throughout this season (see Section 2.4.3). The $L_s \approx 250° - 300°$, throughout which the dust loading globally decreases except for the south pole where the dust optical depth increases. The $L_s \approx 308° - 336°$ period where the last yearly peak in atmospheric dust loading occurs (see Figure 2.17), as a consequence of the occurrence of several southern and cross-equatorial dust storms (see Figure 2.16). Despite being repeatable year-to-year there is some inter-annual variation mainly in strength and duration of these seasons (Kahre et al., 2017).

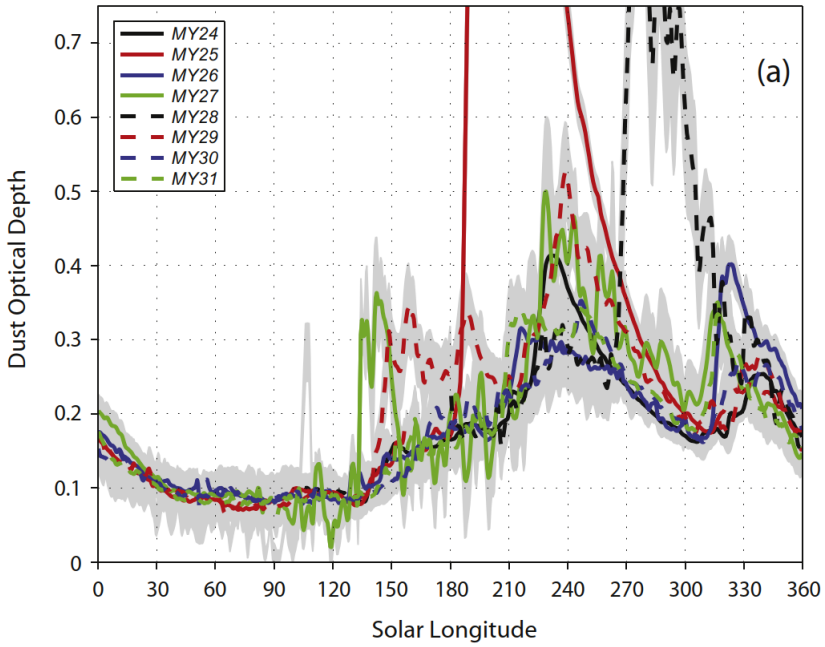

Figure 2.17: Plot of equatorial ($5°S$˘$5°N$) $9.3\mu m$ absorption column dust optical depth normalized to $610Pa$ (τ) as a function of solar longitude for all eight martian years, extracted from the gridded maps. Source: Montabone et al. (2015).

The dust vertical distribution is also relevant as the atmosphere's ability to transport dust upwards directly influences its ability to transport it horizontally and is, therefore, a key factor in both its spatial distribution (Kahre et al., 2017) and the adiabatic heating rates (Smith, Wolff, Clancy, Kleinböhl, & Murchie, 2013). At lower altitudes ($10 - 20km$) the dust is well-mixed (Lemmon et al., 2015), particularly in the low-to-middle latitudes. The vertical extent of the dust is highly variable with the season reaching altitudes of $\approx 50km$ at low latitudes during perihelion (Smith et al., 2013) but being confined near the surface during the non-dusty season (Kahre et al., 2017).

Historically two types of dust lifting events on Mars have been distinguished: dust devils and dust storms. Despite being ubiquitous and potentially vital in the maintenance of the background haze (Kahre, Murphy, & Haberle, 2006), dust devils are local-scale events, very much comparable to their terrestrial counterparts. On the other hand, dust storms are larger events that usually have optically thick clouds associated with them.

Dust storms are classified into three categories: local, regional and global dust storms. A regional dust storm has an areal extent of more than $1.6 \times 10^6 km^2$ and a temporal extent of more than 2 days (Cantor, James, Caplinger, & Wolff, 2001). The term "global dust storm" remains without an unambiguous definition however, many authors consider a storm to be global if it extends for an area greater than $5 \times 10^7 km^2$ (Gichu & Ogohara, 2019).

Local dust storms are very frequent - more than 2000 per year (R. Haberle, 2015) - have shorter lifetimes and can occur in both hemispheres across all seasons despite having statistically favoured locations and periods (Cantor, 2007). Figure 2.18 shows the latitudinal and seasonal distribution of dust storm occurrence on Mars for three Martian years. These local storms tend to develop near the waxing and waning polar caps due to increased surface wind stress - particularly in the receding cap (Kahre et

al., 2006) - consequence of the horizontal thermal gradient (see Figure 2.18). Local dust storm activity reaches a maximum around $L_s \approx 10° - 20°$ and $L_s \approx 135° - 140°$ in the northern hemisphere and $L_s \approx 205° - 250°$ and $L_s \approx 0° - 40°$ in the southern hemisphere (Kahre et al., 2017). Additionally local storms also develop in middle latitudes in both hemisphere peaking around $L_s \approx 200° - 235°$ and $L_s \approx 310° - 340°$ in the northern hemisphere and $L_s \approx 20° - 45°$ and $L_s \approx 135° - 179°$ in the southern hemisphere (Kahre et al., 2017).

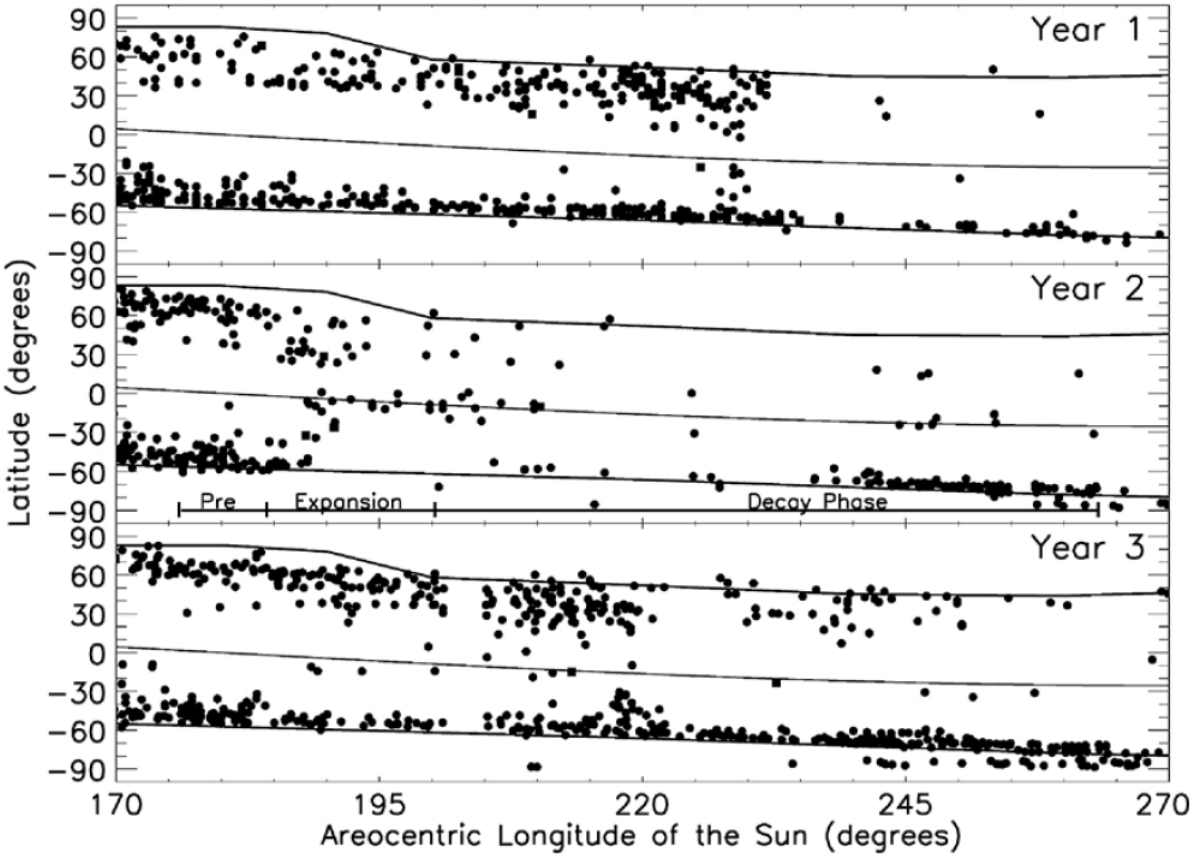

Figure 2.18: Latitudinal distribution of dust storms as a function of the areocentric longitude of the Sun ($L_s = 0°$ corresponds to the spring equinox) from $L_s = 170°$˘$270°$ during the first three Mars years: (top) mapping mission (1999), (middle) extended mission (2001), and (bottom) relay mapping mission (2003). The central curve in each plot corresponds to the sub-solar latitude. The top and bottom curves in each plot are the average latitude of the northern and southern polar cap/polar hood edge. Source: Kahre et al. (2017).

Regional dust events are far less common - few tens of occurrences per Martian year (Cantor, 2003) - but induce a much more significant atmospheric response. They occur throughout the whole year but have increased frequency in the dusty season ($L_s \approx 135° - 360°$; see Figure 2.16). Many regional dust storms are a product of the mergers of local storms (Cantor et al., 2001). Some develop from local storms associated with frontal weather activity (Wang, Zurek, & Richardson, 2005). Such are abundant at high northern latitudes - during $L_s \approx 320° - 130°$ - as they are related to the northern hemisphere's westerly jets (see Section 2.4.3; Kahre et al. (2017)). Some regional storms can propagate southward and cross the equator and even ignite other dust lifting events if under appropriate conditions (see Wang and Ingersoll (2003) for further details). Recently it has been proposed that Martian dust storms may have a threshold size and duration that if achieved can sufficiently thermodynamically perturb the atmosphere to induce a

positive feedback mechanism that allows the event to change size categories (Toigo, Richardson, Wang, Guzewich, & Newman, 2018).

Global dust storms are the more complex and least-understood events in what appertains to the dust cycle and perhaps even the whole climate. These events cover large fractions of the planet with optically thick dust ($\tau_{visible} \geq 3$) and can even envelop the entire planet. Global storms are rare and stochastic in nature - occurring in one out of three years (R. Zurek & J. Martin, 1993) - as their interannual variability is poorly understood (R. M. Haberle, 1986). There have been eight confirmed global dust storms observed (1956, 1971-1972, 1973, 1977, 2001, 2007, 2009 and 2018; Kahre et al. (2017); R. Haberle (2015); Sánchez-Lavega, del Río-Gaztelurrutia, Hernández-Bernal, and Delcroix (2019)). All of these events initiated during the aphelion season (southern spring and summer) when the insolation is near peak values and the circulation is most vigorous (see Section 2.4.3).

Our understanding of both the initiation and decline of global dust storms in only marginal, nevertheless we do know that such events probably originate from the superimposition of three circulation components: the Hadley cell, thermal tides, and topographically controlled circulations. This mechanism was suggested by Leovy, Zurek, and Pollack (1973) and relies on the seasonally increased insolation and dust loading coupled with the above-mentioned components to allow certain storms to become global in scale. The decay of dust storm is even more obscure as the cause for the halting of the dust lifting hasn't been unambiguously unidentified. Either the depletion of surface dust available for lifting shuts off the lifting events (which requires replenishment of the surface dust sources) or the decrease in intensity of the various components allows for the surface wind stress to drop below the required threshold for dust lifting (Kahre et al., 2017; Pollack et al., 1979).

2.5 History of Exploration

It was in the eastern Mediterranean region that the first civilizations to notice Mars as a planet (not a star) rose. However, despite Egyptians, Babylonians and Greeks sharing this accomplishment it was in Britain, more than a thousand years later (in the 18^{th} century), that Sir William Hershel - originally Friedrich Wilhelm Herschel - discovered that Mars had an atmosphere (Herschel (1784) as cited in Sheehan (1996b)).

The modern exploration of Mars did not start until the 20^{th} century. Boosted both by Percival Lowell's claims of evidence for intelligent life (Lowell, 1906) and by the on-going space race prompted by the cold war between the Soviet Union and the United States, several unsuccessful flyby attempts were made in the early 1960s (Table 2.6). It wasn't until 1965 that a successful flyby was accomplished by the Mariner 4 spacecraft, taking the first close-up photographs of Mars (figure 2.19) and marking the beginning of the space exploration of Mars.

This landmark success allowed for the following successes of several spacecraft - of the Mariner and Mars programs - in the late 1960s and early 1970s. The collection of data made by these programs allowed for the confirmation that Mars' polar caps were composed of CO_2 and buffered the atmosphere (Leighton and Murray (1966) as cited in James, Christensen, Clancy, Lemmon, and Withers (2017)), discovered the presence of O_3, the absence of an intrinsic magnetic field, among many other things

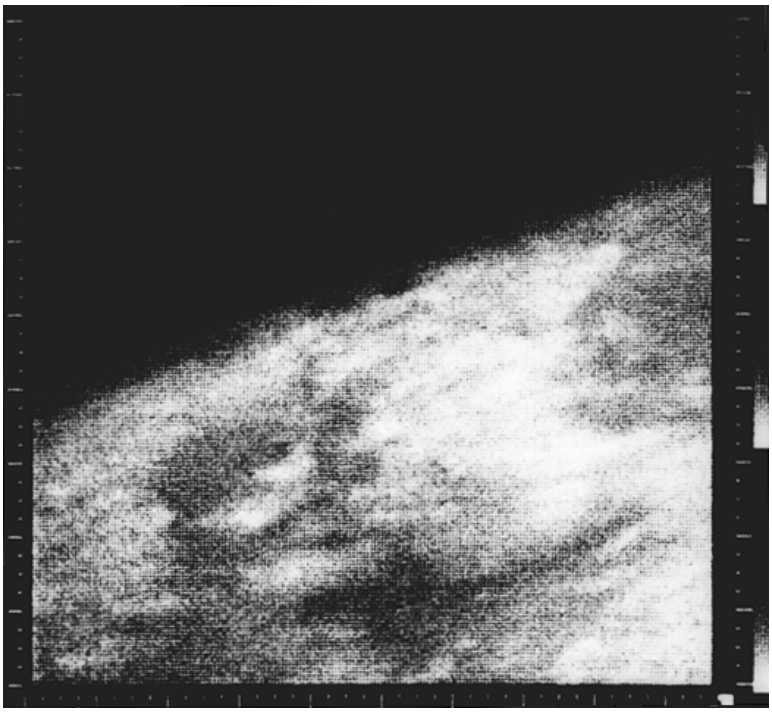

Figure 2.19: Mariner 4 image, the first close-up image ever taken of Mars. This shows an area about 330 km across by 1200 km from limb to bottom of frame, centred at 37 N, 187 W. Source: NASA Space Science Data Coordinated Archive (Williams, 2018a).

(Sheehan, 1996b). Mariner 9 was the first spacecraft to be put into an orbit of Mars and comprehensively characterize its surface properties - by obtaining 7239 images - and map out some of its more relevant geological features.

The current basis for the general understanding of the Martian global climate and atmosphere came from the Viking program data. The Viking missions consisted of two orbiters and two landers with the primary objective of obtaining high-resolution images of the Martian surface, characterize the structure and composition of the atmosphere and surface, and search for evidence of life (Williams, 2018b). The Viking Orbiters were able to detect dust and condensate clouds and map atmospheric temperatures and water vapor column abundances (James et al., 2017), having been considered two extraordinarily successful missions. A few weeks after reaching orbit both landers detached from the orbiters and proceed to land on the northern hemisphere becoming the second and third man-made objects to perform a soft landing on Mars (see Table 2.6). The landers were detrimental in detecting and retrieving chemical species abundances and ratios. Furthermore they provided continuous *in situ* pressure measurements (see Figure 2.2) which confirmed the existence of a carbon dioxide cycle (James et al., 2017).

As the 1990s and early 2000s progressed the focus of the Mars' missions shifted from obtaining more complete datasets of atmospheric and surface properties (Mars Observer, Mars Global Surveyor, Nozomi and Mars Climate Orbiter - see Table 2.6 and 2.7) to the investigation of the surface and sub-surface - particularly for signs of present or past water activity - and of the possible habitability of Mars (Mars Pathfinder, Sojourner, Deep Space 2, Mars Odyssey, Mars Express, Spirit, Opportunity, and Phoenix - see Table 2.7).

Instruments other than space probes have been used to study the Martian atmosphere. Ground-based

spectrographs have been extensively used to study the chemical composition and abundance of the atmosphere since the late 1960s. More recently they have also been used to perform middle atmosphere wind measurements (Lellouch et al., 1991; Clancy et al., 2006; Sonnabend et al., 2006; Cavalié et al., 2008; Moreno et al., 2009; Sonnabend et al., 2012). Other imaging instruments like the Hubble Space Telescope have also been able to measure winds and upper atmosphere chemical abundance measurements (James et al., 2017).

The exploration of the red planet has never been more exciting. There are currently seven missions being developed to be launched until 2024 including landers, orbiters, rovers and even a helicopter (Biswal M & Annavarapu, 2019). The primary scientific objectives for these missions include the search for past life, surface morphology characterization, composition determination (namely methane) and preparation for human exploration. Furthermore, there is a proposal for the human exploration of Mars in the next decade which would be a landmark achievement of the space exploration age.

Table 2.6: Comprehensive Summary of Planetary Missions to Mars. Source: Adapted from Biswal M and Annavarapu (2019).

Spacecraft	Type	Launch	Country	Mission Program	Outcome
1M No.1	Flyby	1960	USSR	Flight testing	Failure
1M No.2	Flyby	1960	USSR	Explore Mars from trajectory	Failure
2 MV-4 No 1	Flyby	1962	USSR	Study Mars from trajectory	Failure
2 MV-4 No 4	Flyby	1962	USSR	Photographing Mars	Failure
2 MV-3 No 1	Lander	1962	USSR	Descend on the surface of Mars	Failure
Mariner 3	Flyby	1964	USA	Examine Mars from trajectory	Failure
Mariner 4	Flyby	1964	USA	Examine Mars from trajectory	**Success**
Zond 2	Flyby	1964	USSR	Survey of Mars from flight path	Failure
Mariner 6	Flyby	1969	USA	Study and Imaging of Mars	**Success**
2M No 521	Orbiter	1969	USSR	Study Mars from Orbit	Failure
Mariner 7	Flyby	1969	USA	Study the surface and atmosphere	**Success**
2M No 522	Orbiter	1969	USSR	Imaging Martian Surface	Failure
Mariner 8	Orbiter	1971	USA	Study Mars from Orbit	Failure
Cosmos 419	Orbiter	1971	USSR	Overtake US Mars probes	Failure
Mars 2	Orbiter	1971	USSR	Imaging Martian surface and clouds	**Success**
Mars 2	Lander	1971	USSR	Landing attempt on Mars	Failure
Mars 3	Orbiter	1971	USSR	Study topography of soil	**Success**
Mars 3	Lander	1971	USSR	Landing attempt on Mars	Failure
Prop-M Rover	Rover	1971	USSR	To determine soil density	Failure
Mariner 9	Orbiter	1971	USA	Study Mars atmosphere	**Success**
Mars 4	Orbiter	1973	USSR	Study Mars from orbit	Failure
Mars 5	Orbiter	1973	USSR	Study Mars from orbit	Partial **Success**
Mars 6	Flyby	1973	USSR	Study Mars from orbit	**Success**
Mars 6	Lander	1973	USSR	Landing attempt on Mars	Failure
Mars 7	Flyby	1973	USSR	Study Mars from orbit	**Success**
Mars 7	Lander	1973	USSR	Landing attempt on Mars	Failure
Viking 1	Orbiter	1975	USA	Investigate Mars and search for life	**Success**
Viking 1	Lander	1975	USA	Search for life	**Success**
Viking 2	Orbiter	1975	USA	Investigate Mars and search for life	**Success**
Viking 2	Lander	1975	USA	Search for life	**Success**
Phobos 1	Orbiter	1988	USSR	Study the interplanetary environment	Failure
Phobos 1	Lander	1988	USSR	Study composition of Martian satellite	Failure
Phobos 2	Orbiter	1988	USSR	Study the interplanetary environment	**Success**
Phobos 2	Lander	1988	USSR	Study the composition of Phobos	Failure
Mars Observer	Orbiter	1992	USA	Study the Martian magnetic field	Failure
Mars Global Surveyor	Orbiter	1996	USA	Monitoring atmospheric and surface features	**Success**
Mars 96	Orbiter	1996	USSR	Study the evolution of Mars	Failure
Mars 96	Lander	1996	USSR	Study the evolution of Mars	Failure
Mars 96	Penetrator	1996	USSR	Surface Soil Penetration	Failure

Table 2.7: (Continued) Comprehensive Summary of Planetary Missions to Mars. Source: Adapted from Biswal M and Annavarapu (2019).

Spacecraft	Type	Launch	Country	Mission Program	Outcome
Mars Pathfinder	Lander	1996	USA	Investigate surface of Mars	**Success**
Sojourner	Rover	1996	USA	Roving the surface of Mars	**Success**
Nozomi	Orbiter	1998	Japan	Study the upper atmosphere of Mars	Failure
Mars Climate Orbiter	Orbiter	1998	USA	Study the Martian climate	Failure
Mars Polar Lander	Lander	1999	USA	Landing attempt on Mars	Failure
Deep Space 2	Penetrator	1999	USA	Soil Analysis by Penetrating	Failure
Mars Odyssey	Orbiter	2001	USA	Determine Mars Habitability	Operational
Mars Express	Orbiter	2003	Europe	Search for sub-surface water	Operational
Beagle 2	Orbiter	2003	Europe	Search for sub-surface water	Partial **Success**
Spirit	Rover	2003	USA	Search in possible evidence of past water activity	**Success**
Opportunity	Rover	2003	USA	Search in possible evidence of past water activity	Operational
Rosetta	Gravity Assist	2004	Europe	Study the origin of solar system and cometary matter	**Success**
Mars Reconnaissance Orbiter	Orbiter	2005	USA	Characterize climate on Mars	Operational
Phoenix	Lander	2007	USA	Search for Habitable zones	**Success**
Dawn	Gravity Assist	2007	USA	Characterize conditions of early solar system	**Success**
Fobos-Grunt	Orbiter	2011	USSR	Study Mars from orbit	Failure
Fobos-Grunt	Sample Return	2011	USSR	Sample return to Earth	Failure
Yinguo-1	Orbiter	2011	China	Investigate plasma environment	Failure
Curiosity	Rover	2011	USA	Exploring Mars Habitability	Operational
Mangalyaan	Orbiter	2013	India	Explore Mars and Surface	Operational
Mars Atmosphere and Volatile Evolution	Orbiter	2013	USA	Study the history of loss of Mars atmosphere	Operational
ExoMars Trace Gas Orbiter	Orbiter	2016	Europe	Measure the abundance of Methane and other gases	Operational
Schiaparelli Descent and Landing Demonstrator Module	Lander	2016	Europe	Validate and demonstrate EDL for ExoMars 2020	Partial **Success**
InSight	Lander	2018	USA	Study planets early geological evolution	Operational

2.5.1 Mars Express

The Mars Express mission is a European Space Agency mission to Mars - which includes the Mars Express orbiter and the Beagle 2 lander - launched in the 2^{nd} of June 2003. It entered the Martian orbit on December 2003 intending to study the Martian atmosphere and climate, the planet's structure, mineralogy and geology, and to search for traces of water. It has completed more than 5000 orbits in its eccentric polar trajectory ($250 - 300km$ at pericentre and $10.000 - 12.000km$ at apocentre).

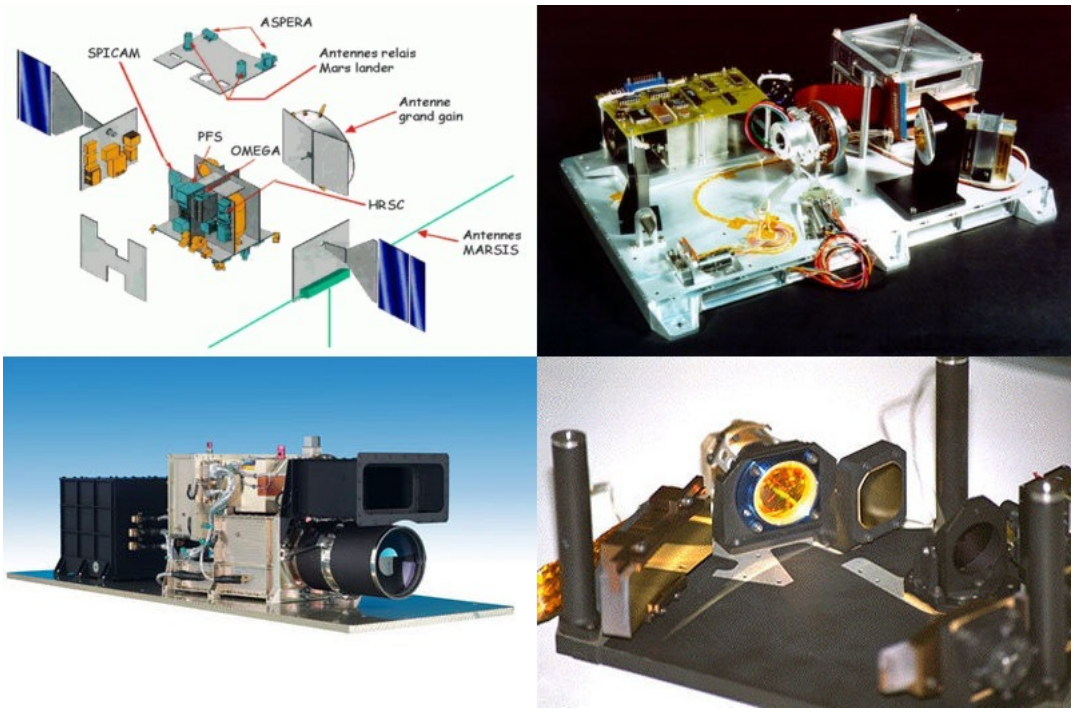

Figure 2.20: From up and left to the right and down: Mars Express spacecraft schematic, SPICAM (Ultraviolet and Infrared Atmospheric Spectrometer), HRCS (High Resolution Stereo Camera) and OMEGA (Visible and Infrared Mineralogical Mapping Spectrometer). Source: Mars Express European Space Agency Page (ESA, 2017).

Mars Express is equipped with eight different instruments on-board:

– **SPICAM (SPectroscopy for the Investigation of the Characteristics of the Atmosphere of Mars):** SPICAM consists of two spectrometers - ultraviolet and infrared - aimed at the investigation of the atmospheric chemical stability, atmospheric escape, surface/atmosphere interaction, wave activity in the middle atmosphere and the impact of aerosols on the climate (Bertaux et al., 2004).

– **ASPERA-3 (Analyser of Space Plasmas and Energetic Ions for Mars Express):** ASPERA consists of four sensors - two energetic neutral atom sensors, electron spectrometer, and ion spectrometer - designed to study the interaction between the solar wind and the Martian atmosphere, the impact of plasma processes on atmospheric evolution and global plasma and neutral gas distributions in the near-Mars environment (Barabash et al., 2004).

– **PFS (Planetary Fourier Spectrometer):** The PFS covers the infrared range ($1.2 - 45\mu m$) in two channels - and performs real-time on-board Fast Fourier Transform - to study primarily the atmospheric temperature, its coupling with the surface and chemical species abundance (Formisano et

al., 2004).

- **OMEGA (Observatoire pour la Minéralogie, l'Eau, les Glaces et l'Activité):** OMEGA is a near-infrared and visible spectrometer aimed at the study of the surface mineralogical and molecular composition and spatial and temporal distribution of some atmospheric constituents and aerosols (Bibring, 2004).

- **HRSC (High Resolution Stereo Camera):** HRSC is an imaging instrument aimed at geological investigation (through high-resolution mapping of the surface structure and morphology), atmospheric phenomena characterization and support for exobiological studies (Neukum & Jaumann, 2004).

- **MARSIS (Mars Advanced Radar for Subsurface and Ionosphere Sounding):** MARSIS is a radar developed to use long-wavelength wide-band pulses to detect and map subsurface structures (particularly in the search for solid and liquid water reservoirs) and surface topographic features and properties along with ionospheric studies (Picardi et al., 2004).

- **MaRS (Mars Radio Science):** MaRs is a radio emitter that uses the effects that the propagation of the signals through different mediums have on its properties to investigate the ionosphere, atmosphere, surface, and interior (Patzold et al., 2004).

- **VMC (Visual Monitoring Camera):** VMC is an engineering camera used to confirm the Beagle-2 lander separation that got reactivated for outreach purposes (in 2007) and re-purposed to complement both HRSC and OMEGA instruments (in 2016) by using it to monitor aerosols and characterize surface features.

The Mars Express mission - named after the expeditious manner in which it was assembled - was originally intended to last 1 Martian year (≈ 687 Earth days) with another of extension possible but it has now been active for more than 15 years. Throughout all these years it kept collecting data and enabling incredible discoveries and advancements: evidence for the existence of liquid water, detection of methane in the atmosphere, atmospheric escape rate estimation or unambiguously detecting CO_2 clouds. It is the second-longest surviving spacecraft orbiting around a planet other than Earth and is generally regarded as one of the most successful missions ever.

3 VLT Observations

3.1 UVES Description

Figure 3.1: ESO VLT facility in Chile. Source: ESO images.

UVES is an Ultraviolet and Visual Echelle Spectrograph (Dekker, D'Odorico, Kaufer, Delabre, & Kotzlowski, 2000) which is mounted at the Nasmyth B focus of the Unit Telescope 2 (also known as Kueyen) of the ESO's (European Southern Observatory) VLT (Very Large Telescope) facility located in the Atacama Desert in Cerro Paranal, Chile. It has been operational since 1999 and was built with the following scientific objectives (Dekker et al., 2000):

- Study the structure, physical conditions and abundances of interstellar and intergalactic gas at early epochs from the absorption spectra of high red-shift Quasi Stellar Objects.
- Study the kinematics of gas and stars in galactic nuclei.
- Study the kinematics and mass distribution of star clusters.
- Study the position, kinematics and physical conditions of the interstellar medium in the galaxy and nearby systems.
- Study of the chemical composition and atmospheric models of galactic and extragalactic stars.
- Study of sub-stellar companions of nearby stars (high-precision radial velocity studies over long time scales).
- Study of stellar oscillations.

At its construction date, UVES *echelle* grating was the largest monolithic diffraction device developed. The importance of this technological development resided in the possibility to increase the spectrograph spectral resolution to resolve stellar absorption lines. In 2002, the high-precision HARPS (High Accuracy Radial Velocity Planetary Search object) spectrograph became operational at La Silla (Chile), to find extrasolar planets, it uses an *echelle* of the same kind that had been chosen for UVES.

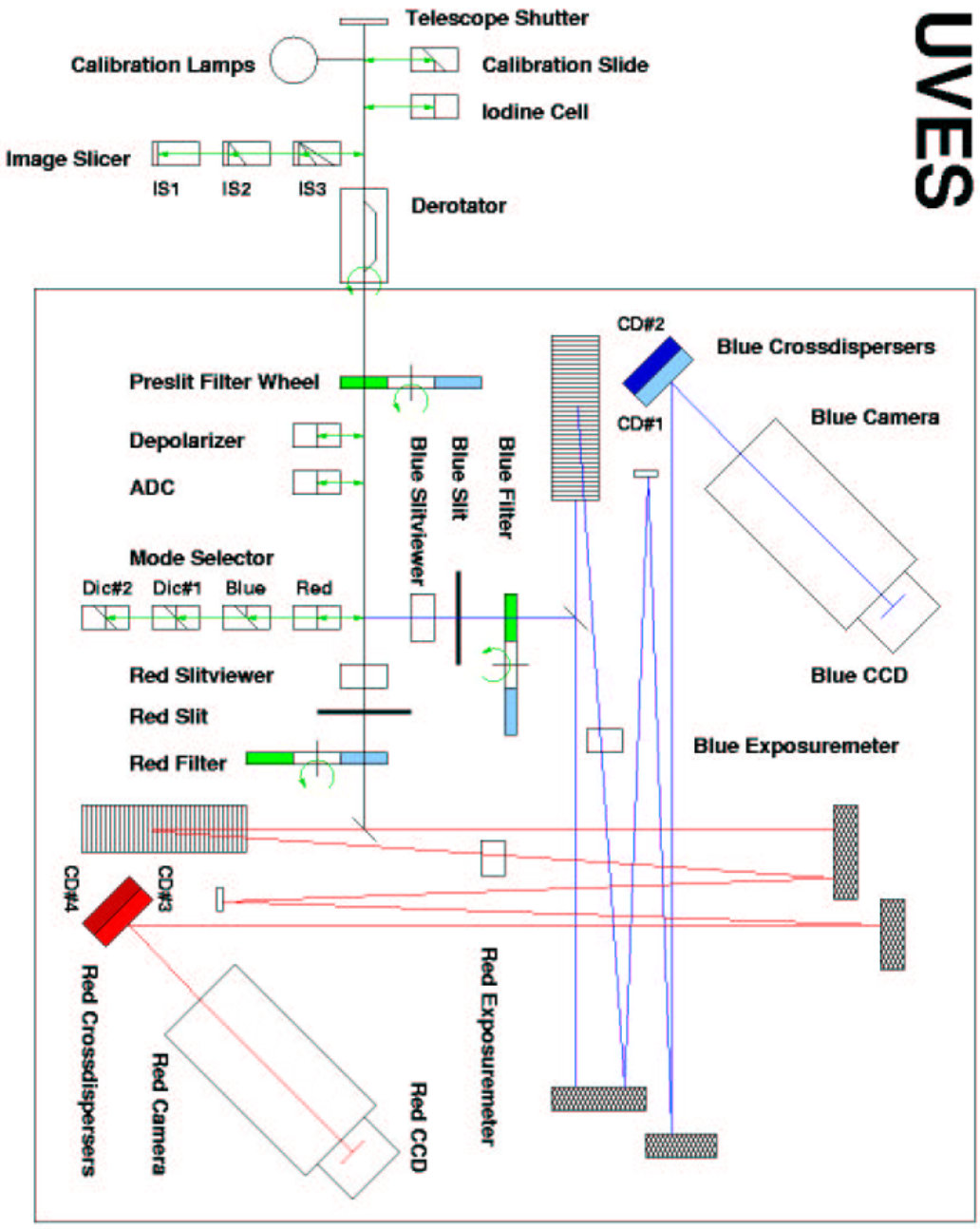

Figure 3.2: UVES schematic. Source: Sbordone and Ledoux (2017).

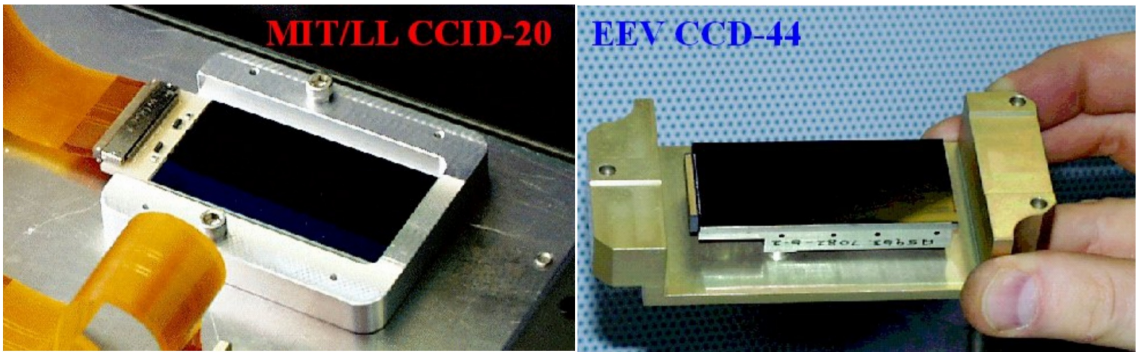

Figure 3.3: The two CCD detectors in UVES. Source: Dorn et al. (2000).

The spectral resolution (nominal) designed for this unit, with an $1''$ slit was 40,000 (D'Odorico et al., 2000). *Echelle* spectrographs are very important instruments in projects involving large telescopes since high-resolution spectroscopy is one of the observation modes that can most benefit from a large light-collecting area. This makes the telescope resolve the absorption lines and helps to detect the chemical species present in the atmospheres, allowing them to map its composition with high detail.

UVES is a cross dispersed *echelle* spectrograph that produces an order separation higher than $10''$ which allows semi-long slit spectroscopy of compact objects such as Mars ((Sbordone & Ledoux, 2017)). This is relevant because this separation allows for a good sampling of the sky's scattered light at red wavelengths, enabling a fairly accurate estimation of the background radiation at spectral inter-orders. To maximize efficiency it is equipped with two arms: the blue arm (covers the wavelength range $\lambda = 300 - 500nm$) and the red arm ($\lambda = 420 - 1100nm$). Furthermore, the versatility of this instrument allows the use of either arm individually or both in parallel through the application of a dichroic beam splitter which separates the light into both wavelength ranges. The maximum resolution that can be attained is $\approx 80,000$ in the blue wavelength range (using a $0.4''$ slit) and $\approx 110,000$ in the red wavelength range (using a $0.3''$ slit). In this case, the numerical resolution of the instrument is of 2 pixels.

When the light enters the telescope (see Figure 3.2) it is split by the diachronic prism, it then follows an identical path on both arms: First, it passes through collimator mirrors designed to align the beam perpendicular to the *echelle*. Then it goes through the *echelle* gratings ($21 \times 84cm$) which separate the light beam into several orders. These orders, however, overlap and need to be separated by two cross dispersers (CD#1 and CD#2 in the blue arm and CD#3 and CD#4 in the red arm) and then the light beam is ready to be directed towards the CCD (Charge-Coupled Device) detectors (see Figure 3.3).

UVES's blue arm is equipped with single 2K x 4K, $15\mu m$ pixel EEV CCD-44 detector while the red arm is equipped with a mosaic of two CCD's - a EEV CCD-44 (identical to the one used for the blue arm) and a MIT/LL CCD-20 chip (see Figure 3.3). The readout noise is less than 3 electrons for the MIT-LL detector and less than 2 for the EEV (for slow readout with high gain) (see Table 3.1). While the EEV CCD has a capacity for 225.000 electrons and high quantum efficiency at ultraviolet ranges the MIT type CCD has a capacity for 130.000 electrons and high efficiency in the near infra-red (see Table 3.1). The first 50 pixels, at each CCD output gate, are assigned to pre-scan operations. To minimize the dark current noise the CCD's are kept in a vacuum chamber cooled by liquid nitrogen until a temperature of $\approx 130°K$ (Machado, 2014). This cryostat unit has an autonomy range of approximately 2 weeks allowing for continuous thermal stability through long periods ($\leq 1°$ C according to Machado (2014))

Table 3.1: Measured properties of UVES scientific CCD's. Source: Adapted from Sbordone and Ledoux (2017).

	Blue, EEV	**Red, Mosaic**
Quantum efficiency	49% at $320nm$ 56% at $350nm$ 82% at $400nm$ 88% at $500nm$	89% at $450nm$ (EEV) 89% at $600nm$ (EEV) 84% at $800nm$ (MIT-LL) 64% at $3900nm$ (MIT-LL) 18% at $1000nm$ (MIT-LL)
Number of pixels	2048×3000 (2048×4096, used in windowed readout)	4096×4096 (2048×4096 2×1 mosaic)
Pixel size	$15\mu m$	$15\mu m$
Gain (MIT-LL values in brackets)	low: 1.84 e^-/ADU high: 0.54 e^-/ADU	low: 1.5 (1.4) e^-/ADU high: 0.52 (0.46) e^-/ADU
Read-out noise fast read-out, low gain (slow read-out, high gain) Ultrafast readout, low gain	4.1 (2.1) e^- rms	EEV 4.2 (2.8) e^- rms MIT 3.7 (2.1) e^- rms EEV 4.3 e^- rms MIT 4.7 e^- rms
Dark current levels	0.4 e^-/pix/h at $120°C$	EEV 0.5, MIT 1.5 e^-/pix/h at $120°C$
Charge transfer efficiency	> 0.99993	> 0.99995

which may be required for extended observations. Additionally, the blue arm has an optical field of $30.7 \times 30.7mm$ while the red arm has one of $61,4 \times 61,4mm$. Since most of the CCD pixels are going to receive radiation they must act in the readout mode.

The pivotal parameters in assessing the instrument overall efficiency are the detection efficiency and the spectral range that is covered by a single exposure. UVES has two basic configurations: The first covers $90nm$ in the blue arm (centred on $\lambda_{center} = 346nm$) and covering $200nm$ in the red arm (centred on $\lambda_{center} = 580$) and the second covers $100nm$ in the blue arm (centred on $\lambda_{center} = 437nm$) and covering $860nm$ in the red arm (centred on $\lambda_{center} = 580$) for a single exposure. Except for a $5 - 10nm$ loss in between the CCDs in the red arm (for the first and second configuration respectively), there is no wavelength loss as the wavelength ranges overlap (Sbordone & Ledoux, 2017).

UVES has a calibration unit that contains, among other things, a wavelength calibration lamp - of

Thorium-Argon or Deuterium - and an Iodine cell that allow a dense - well known and referenced - absorption line rich range superimposed on the spectrum which can be an inconvenience. The Iodine cell absorption features only cover the wavelength range $490 - 640nm$ while the lamps have more comprehensive ranges. Furthermore, the Iodine cell may absorb up to 50% of the incoming radiation which excludes its use when observing weak targets (Machado, 2014).

It also contains a slit unit which consists of two aluminum blades whose separation is defined as the slit width (can be adjusted within the range $0.15'' - 20''$) while the slit length can vary up to $30''$. The acquisition and tracking of targets is done using the slit viewer which is a camera that sees through the slit blades and thus provides images of the slit on the target (Sbordone & Ledoux, 2017).

There are several other additional relevant features that may be required for the telescope to operate effectively. First of all, the image slicers allow to obtain high resolution with unfavorable seeing conditions, secondly the optical derotator can be used to provide compensation for the field rotation and thirdly the atmospheric dispersion corrector (ADC) unit inserts two counter-rotating prisms in order to correct for the atmospheric dispersion up to zenith angles of $\approx 65°$. Additionally, the Depolarizer can insert a rotating plate to cancel the intrinsic polarization that might be affecting the signal. UVES also contains a pre-slit wheel with 16 positions, 15 of which correspond to filters (either neutral density or Johnson broad-band filters) (Dekker et al., 2000).

The instrument is separated into two sections. The first, containing the calibration system the image slicers, and the derotator is mounted on the rotor, remaining stationary, while the telescope adapter moves to track the target in the sky. The second section consists of the *echelle* and the cross-disperser arms. For the purposes of minimizing the perturbations, the only moving parts in the optical path are the slit blades, the cross-disperser, and the cameras (Sbordone & Ledoux, 2017).

The signal-to-noise ratio increases with the square of the diameter of the telescope, thus choosing a large telescope as is the VLT was important for these observations to be successful. Even in the case where very bright sources are used, large telescopes are preferred as they enable us to achieve high signal-to-noise ratios in short integration times.

The correct use of all of UVES features, combined with our Doppler velocimetry method and our investigation group's expertise on the matter, allows us to retrieve planetary wind velocities with incredible precision. The combination between comprehensive wavelength coverage, large collecting area (approximately 8 m) and small pixel size - which allow for high-velocity measurement precision, good signal-to-noise ratio and good spatial resolution - make UVES an optimal spectrograph for Doppler velocity measurements (Machado, 2014).

3.2 The 2018 global dust storm

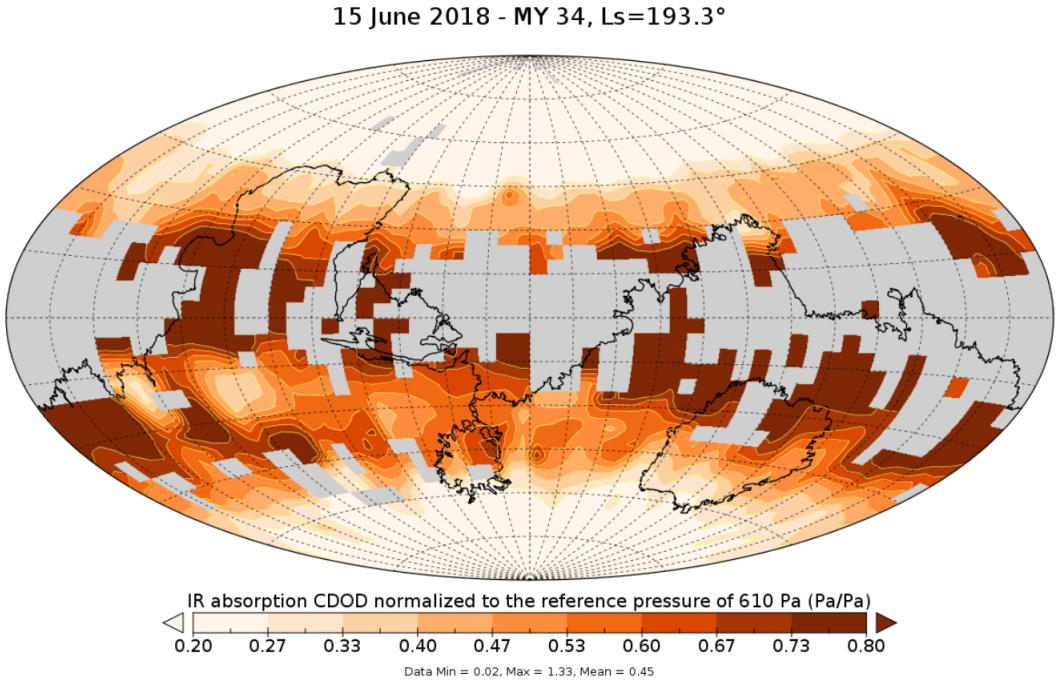

Figure 3.4: Map of dust opacity retrieved from Mars Climate Sounder infrared observations on 11^{th} June 2018 (+/-1 day), showing the dust storm under development on Mars, in the Martian Year (MY) 34, started at $L_s = 185°$ (30 May 2018). Credits: Luca Montabone.

On the 30^{th} of May of 2018 ($L_s \approx 185°$ of the Martian Year 34) a frontal-like local dust storm was noticed on Mars centred around $35°N - 12°W$ - in the Acidalia Planitia. It covered an area of approximately $1.4 \pm 0.3 \times 10^5 km^2$ but in one day this value almost quadrupled to reach $5.1 \pm 0.3 \times 10^5 km^2$ (Sánchez-Lavega et al., 2019). Over the next few weeks (during the growth stage) the storm expanded to cover most of the northern hemisphere and propagated southward, crossing the equator at one of the three proffered longitudinal corridors - the Acidalia corridor - activating independent dust lifting events in the southern hemisphere (which later merged with the global dust storm). It reached a planet-encircling stage on June, 17^{th} ($L_s \approx 195°$) ending its growth phase shortly after (Kass et al., 2019). The Curiosity rover measured an atmospheric optical opacity of 8.5 around $L_s \approx 196°$ (Guzewich et al., 2019). The growth pattern followed by this storm fits well on the described pattern of other non-global storms that developed in the same region (Sánchez-Lavega et al., 2019; Wang & Richardson, 2015). It is visible in Figure 3.4 that the opacity values across the storm show variability.

Despite having some "well behaved" traits, the 2018 Martian global dust storm had some very extraordinary aspects as well. The onset of the storm ($L_s \approx 185°$) was, along with the 2001 event, the earliest on record (Sánchez-Lavega et al., 2019; Wang & Ingersoll, 2003). Despite being a common ground for the initiation of regional storms, never has a global dust storm been observed to initiate in the Acidalia Planitia nor in the Northern Hemisphere (Sánchez-Lavega et al., 2019; Kahre et al., 2017).

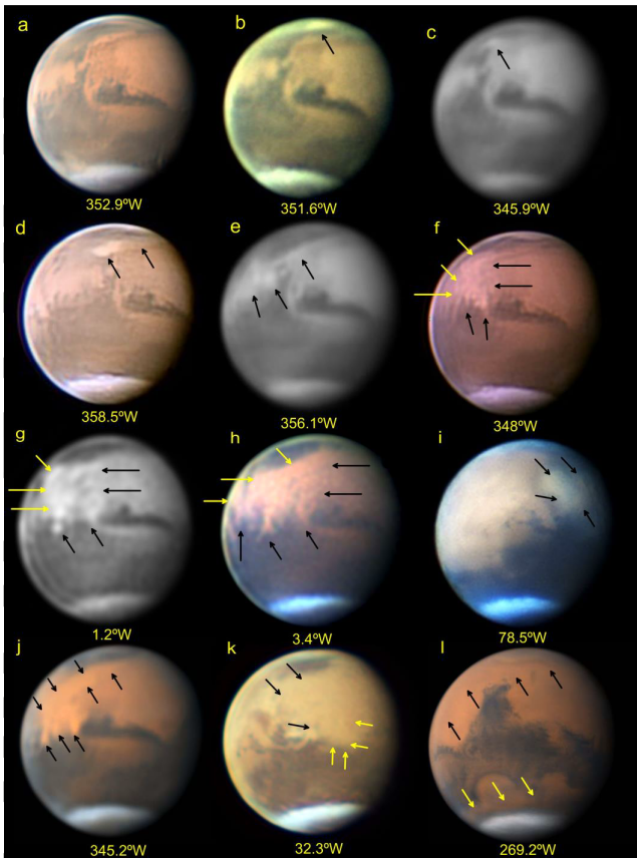

Figure 3.5: Image (a) shows the region free of storms (12 May, 20:51 UT, T. Olivetti) and (b) shows a precursor storm (arrow) centred at $346.7°W$ and $56°N$ (27 May, 05:42 UT, G. Grassmann). Images (c)-(l) show the onset and initial daily expansion phase of the GDS2018 (the arrows identify the area of the expanding storm). (c) 30 May, 7:25 UT, E. Morales; (d) 31 May, 08:55 UT, J. Rueck; (e) 1 June, 09:24 UT, E. Morales; (f) 2 June, 09:29 UT, J. Rueck; (g) 3 June, 11:02 UT, P. Maxon; (h) 4 June, 11:49 UT, K. Beverage; (i) 4 June, 16:57.9 UT, D. Millika and Nicholas; (j) 5 June, 11:13.4 UT, D. Peach; (k) 6 June, 15:05 UT, A. Casely; (l) 8 June, 07:55.9 UT,D. Peach. The Central Meridian (CM) is given in the west longitude system below each image. Source: (Sánchez-Lavega et al., 2019).

Like the 2001 global dust storm, this storm was equinoctial, meaning it formed in non-dusty conditions when the Hadley circulation is roughly symmetric around the equator and is at its weakest. As a consequence Sánchez-Lavega et al. (2019) argues that the onset of the storm was more likely due to interference between different nodes of the thermal tides. Simulations using NASA Ames Mars GCM confirm that the coupling of thermal tides and the Hadley circulation could produce enough dust transport to explain its onset and early expansion (Bertrand, Wilson, & Kahre, 2019).

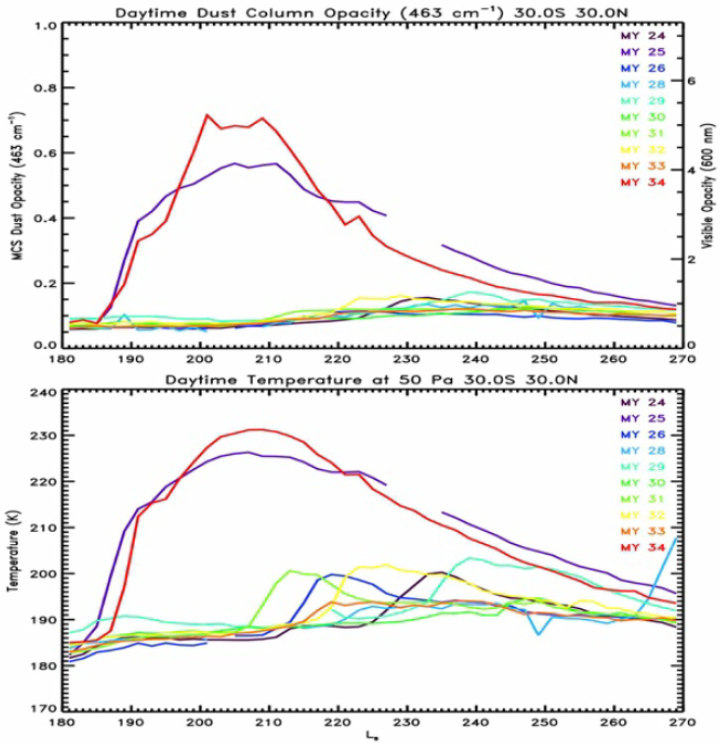

Figure 3.6: Daytime tropical zonal mean dust column opacity (top) and 50 Pa (25 km) temperatures (bottom) during MCS and TES years. Source: Kass et al. (2019).

The storm reached its decay phase at $L_s \approx 213°$ (Kass et al., 2019). Figure 3.6 (a) shows the dust column opacity during the day for several Mars years. The Martian year 25 (2001 global dust storm) and 34 (2018 global dust storm) show similar overall behavior, particularly in the growth and decay phase. The dust opacity decline measured from the Curiosity rover was also similar to previous observations (Guzewich et al., 2019). Furthermore, GCMs simulating the storm indicate that surface stress increases in many locations during the decay phase, suggesting that the surface dust supply may be limited (Bertrand et al., 2019).

3.3 Our observations

As the global dust storm started developing on Mars (May of 2018) - $L_s \approx 185°$ of the Martian year 34 - our team submitted a last-minute proposal to observe Mars during this event. The final objective was to retrieve wind velocities, in the middle atmosphere, with our Doppler velocimetry method developed and fine-tuned by Machado et al. (2012) to the case of Venus.

Unlike Venus, Mars' atmosphere is very transparent in the visible and ultraviolet ranges and the radiation in those wavelength ranges that is back-scattered in the atmosphere is negligible which precludes the application of our method. However, during global dust storms, the opacity of the atmosphere increases and allows for the scattering of enough light in the suspended dust in the middle atmosphere for the application of our method to be feasible.

Table 3.2: North Pole position angle, apparent size of Mars, latitude of sub-solar point and phase angle at the date of the observation (25^{th}, June, 2018). Source: NASA Jet Propulsion Laboratory's (JPL) HORIZONS web-interface system.

Position Angle	Apparent Radius	Sub-solar Latitude	Phase Angle
$3.03°$	$19.77''$	$-8.25°$	$24.6°$

The preparation and submission of the observation proposal was done by the principal investigator Pedro Machado (Instituto de Astrofísica e Ciências do Espaço) along with Emmanuel Lellouch (Observatoire de Paris), Luca Montabone (Space Science Institute), Alejandro Cardesin-Moinelo (European Space Agency), Gabriella Gilli (Instituto de Astrofísica e Ciências do Espaço), Thomas Widemann (Observatoire de Paris), Olivier Vitasse (European Space Agency), José Silva (Instituto de Astrofísica e Ciências do Espaço) and Ruben Gonçalves (Instituto de Astrofísica e Ciências do Espaço).

The exposure time was calculated by providing UVES Exposure Time Calculator (Version P102.5) with highly accurate ephemerides data which approximated Mars' flux as a continuum of $4.24 magnitude\ arcsec^{-2}$. The observations were made using UVES' red arm's CD#3 cross disperser with a central wavelength of $580nm$ along with a $12''$ long and $0.3''$ wide slit (Sbordone & Ledoux, 2017). 16 sets of 5 exposures of 15 seconds each - with an estimated signal-to-noise ratio of $100 - 120$ - were requested for a total run time of $\approx$ 2 hours. Additionally, we required exposures of the Thorium-Argon (Th-Ar) lamp for precise wavelength calibration required for the velocity precisions we intended to obtain, so any instrumental drift during the measurement process will equally affect the Th-Ar lamp spectra.

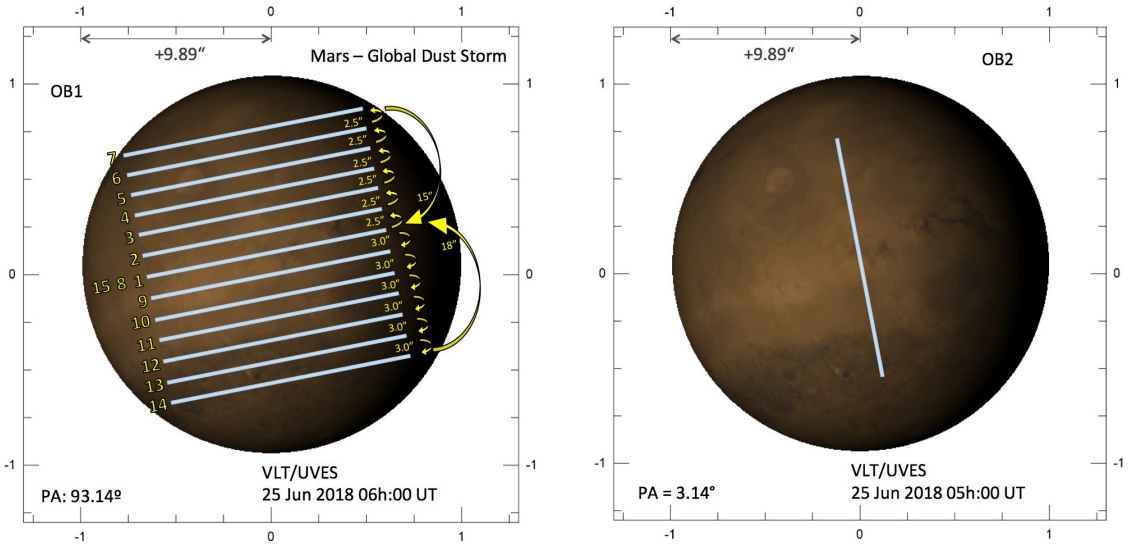

Figure 3.7: Scheme with the slit positions of the observations in relation to Mars.

The observations were carried out on the 25^{th} of June of 2018 using the UVES instrument at the ESO's Very Large Telescope facility in Chile - in service mode - for approximately 2 hours ($\approx$ 5-7 a.m. local time). The conditions were optimal for observations as the seeing was $\approx 0.7 - 1.1$, the sky was clear, the planet's elevation was $\approx 60° - 80°$ and its angular size was approximately $19.8''$. A long and narrow slit ($12'' \times 0.3''$) was used, along with the derotator - to obtain 2 different observational configurations - one with the slit aligned perpendicularly (PP) to the rotation axis and another with the slit aligned in parallel with the same axis (PL). In the PP configuration the slit was moved along the

rotation axis (from the equator to the north-most latitudes and the south-most latitudes) at intervals of $\approx 2.5'' - 3''$ (see Figure 3.7). We observed Mars on 15 different latitudinal offsets and 1 longitudinal (see Figure 3.7), obtaining 5 sets of observations at each position. Table 3.3 summarizes the circumstances of these observations.

Table 3.3: Summary of the geometry and circumstances of the observations. The cases PL and PP correspond to slit orientations parallel and perpendicular to Mars' rotation axis, respectively. The offset number represents a position on the disk, N is the number of exposures taken for each offset and the times are given at the start of the first exposure. The integration time for all exposures was 15 seconds. Lat and Long are the coordinates of the slit's central point on the disk for each offset. The latitude and longitude values given are affected by the VLT/UVES nominal pointing and offset uncertainty, with a total uncertainty $\simeq 0.14$".

Slit	Offset	Time UT	N	Lat(°)	Long(°)	Airmass	Seeing(")
PP	1	05:06	5	14.7 S	48.9 W	1.163	0.79
PP	2	05:12	5	8.7 S	42.7 W	1.148	0.79
PP	3	05:17	5	2.6 S	39.7 W	1.135	0.75
PP	4	05:23	5	3.6 N	38.6 W	1.122	0.82
PP	5	05:28	5	10.1 N	39.0 W	1.110	0.89
PP	6	05:34	5	16.9 N	41.1 W	1.099	0.79
PP	7	05:39	5	24.3 N	41.1 W	1.088	0.77
PP	8	05:45	5	14.7 S	41.1 W	1.078	0.72
PP	9	05:50	5	20.8 S	41.1 W	1.069	1.00
PP	10	05:56	5	26.9 S	41.1 W	1.061	1.09
PP	11	06:01	5	33.1 S	41.1 W	1.053	0.91
PP	12	06:06	5	39.6 S	41.1 W	1.046	0.81
PP	13	06:12	5	46.4 S	41.1 W	1.039	0.94
PP	14	06:17	5	53.8 S	41.1 W	1.033	0.89
PP	15	06:23	5	14.7 S	41.1 W	1.028	0.76
PL	1	06:44	5	-	0	1.012	0.74

VLT pointing and UVES offset uncertainties are both equal to $0.1''$ (nominal value) and we consider the global positioning error of the slit to be $\sigma_{total} = \sqrt{\sigma^2_{pointing} + \sigma^2_{offset}} = 0.14''$. The detector pixel dimension is $15\mu m$ and the pixel scale in our observations is 0.182, this corresponds to a ground-based spatial resolution of $\approx 63km$ on the planetary surface at disk center.

The narrow slit and the pixel projected field of view (relative to the apparent size of the planet) is essential to achieve high spatial resolution. Since instantaneous spatial information is preserved along the slit, a latitudinal and longitudinal set of spectra is acquired. This will allow for latitudinal and longitudinal profiles of the winds.

4 Doppler Velocimetry Method

There are systematic problems with the measurement of absolute wavelengths and Doppler shifts using a grating spectrograph because maintaining a stable velocity reference is a challenge. This is so because the best accuracies achievable when considering the dispersion law and instrumental uncertainties for single line shifts, are of the order of $100ms^{-1}$ while the wind amplitude variations we intend to sound are considerably smaller.

One solution lies in the measurement of relative Doppler shifts between two sets of absorption lines. This technique is fundamentally based on the measuring and weighting of Doppler shifts between the solar Fraunhofer lines of two spectra - of solar radiation backscattered in the middle atmosphere - obtained simultaneously at different points of the slit. The results are relative line-of-sight velocities between different pixels of the slit (points of the disk).

The Doppler velocimetry method used in this work was adapted - to the case of Mars - from the method fine-tuned by Machado et al. (2012), used to derive wind velocities on Venus. This method is based on a technique originally designed for absolute stellar accelerometry by Connes (1985). This work is preceded by several successful applications of this method (Civeit et al., 2005; Luz et al., 2005, 2006; Widemann, Lellouch, & Campargue, 2007; Widemann, Lellouch, & Donati, 2008; Machado et al., 2012; Machado, 2014; Machado et al., 2014, 2017).

For purposes of data treatment and analysis, I used and adapted a software package developed by our investigation unit (in Matlab programming language) used to retrieve wind velocities on Venus (Machado et al., 2012; Machado, 2014; Machado et al., 2014, 2017). This algorithm is composed of essentially three stages: Data reduction, Doppler measurements and Corrections, and coordinate determination.

I adapted the method to the case of long-slit Mars' observations and to perform several corrections, in particular:

- By introducing a geo-referencing correspondence between pixel location and geographic coordinates
- To change the size of the active sounding window of the slit.
- To evaluate for the systematic shift known as the Young effect.
- To correct for the specific geometry of the observations.
- To remove the planetary rotation contribution to the overall Doppler shift.

4.1 Data Reduction

The first step in any method which uses observations is the data reduction process - in which we transform the raw data into a corrected, ordered and simplified form - that allows the application of our Doppler velocimetry method. The end product of this stage is the corrected and calibrated spectrum.

VLT/UVES' raw data files are produced in FITS format (Flexible Image Transport System). In addition to the science type files, there are calibration files - bias frames, flat frames, order definition frames and lamp format check frames - and viewer files that confirm the slit's position on the target. Figure 4.1 shows one of the science files (*echellogram* of Mars).

Figure 4.1: Example of one of the echellograms of Mars that we obtained using VLT/UVES. The dark stripes indicate absorption features.

The calibration files include (Sbordone & Ledoux, 2017; Clayton, 1996):

- **Bias (Type = BIAS):** 5 zero-second exposure frames taken, every night the telescope is operational, with no light entering the instrument to be subtracted to the science frame. This addresses the problem of removing the detector status bias level by removing effects associated with the pixel-to-pixel variations of the offset level and the read-out-noise.
- **Flat (Type = FLAT):** 5 frames taken with a uniform light source - from 4 lamps - to measure the pixel relative sensitivity to the incoming light and ultimately account for it in the spectrum. These act to remove several effects: certain dark features that arise from the presence of dust particles on the CCD chips or on the filter, vignetting effects (likely caused by out of focus objects in the light path), fringing interference (that arise from the use of narrow filter and the wave-like nature of waves that create patterns of multiple reflections within the CCD chip or filter), slit function effect (consequence of small variations of the slit's width) and the *echelle* blaze function (characteristic efficiency along an order).
- **Order Definition Flat (Type = LAMP,ORDERDEF):** Frame taken with a short slit and a continuum flat lamp to identify the central positions of each *echelle* order and of the inter-order background.
- **Format Check (Type = LAMP,FMTCHK):** Frame taken with a Thorium-Argon lamp exposure which guarantees the presence of a few hundred well separated and well-known lines. This allows for very accurate and precise wavelength calibration.

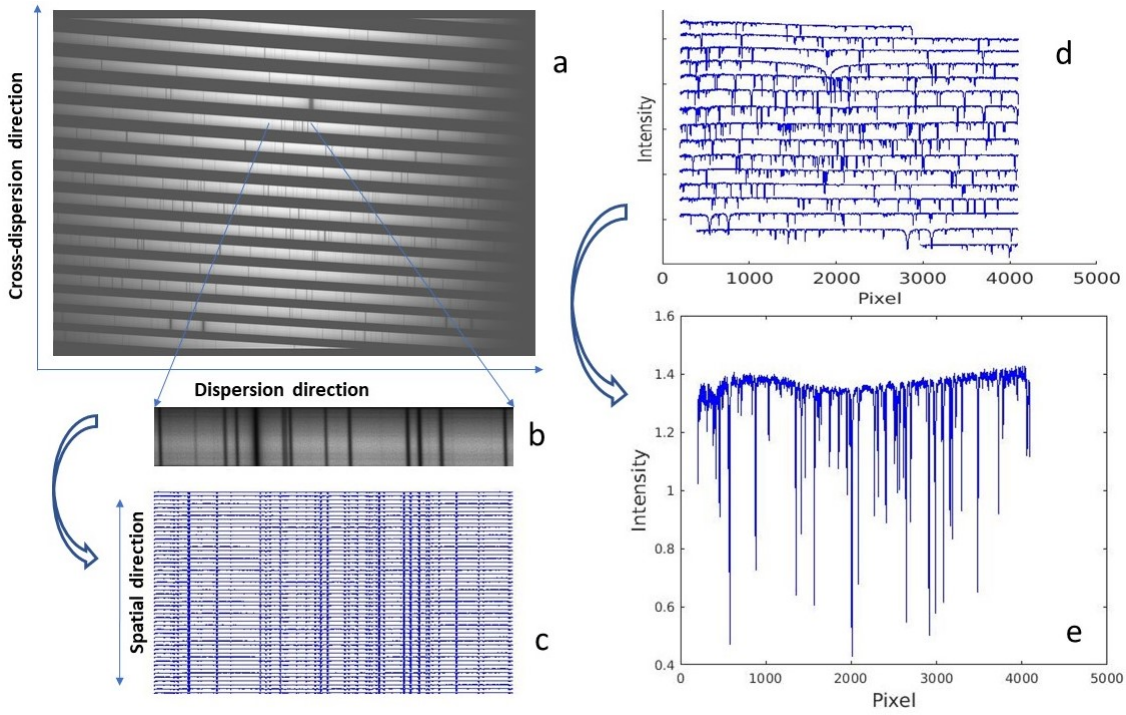

Figure 4.2: Steps for obtaining spectra from a UVES echellogram (example). (a) Raw echellogram showing the spectral orders for one of the detectors. (b) Magnification of part of one order, where absorption lines (dark vertical bands) are visible. From each order, a stack of 53 spectra are extracted (the active window of the slit). (c) Set of 53 spectra, with each one corresponding to one pixel in the slit's active window. (d) Each spectrum is divided into 16 orders in the MIT detector and 23 orders in the EEV detector. The plot shows an example of the 16 components of an MIT spectrum, each coming from one spectral order. (e) Example spectrum from one order and one location in the Martian disk.

The first step of this algorithm is to construct both the Mater bias and Master Flat, by computing the median of the 5 files of each type. The de-biasing is done intermediately upon reading the science file.

The next stage is the mapping of the orders. This is done by using the order definitions files that allow us to find the central position of each order and then estimate the slope at its center. Then the cross-order profile is centered along the order and a polynomial fit is performed.

Next, the data is flat fielded (divided by the Master flat) and the spectra (science) are extracted. The extraction was performed by a piecewise cubic Hermitian polynomial interpolation. Spectra from different spectral orders are extracted separately. Additionally, since there is a $10nm$ gap between the EEV and MIT detector, each detector spectra is also extracted and treated separately so that the final spectrum shows no discontinuities (Machado, 2014). Some of the bad pixels are identified and removed in this stage, using a pre-prepared-mask. The slit's window was restricted to 53 pixels. The primary steps of the spectrum extraction process are shown in Figure 4.2.

Finally, wavelength calibrations are performed by using the Thorium-Argon exposure (format check file). These files' spectra are extracted similarly to the science files. Additionally, a dispersion relation is obtained - through an interpolating process and a polynomial fit to identify the Thorium-Argon line positions - to produce a very accurate correspondence between each pixel in the *echellogram* and its respective wavelength.

A final correction is required for the image curvature. In *echelle* spectroscopy we require that the dispersion and spatial direction be perpendicular, this facilitates immeasurably the processing of the data as is shown in figure 4.2. But due to the different optical path taken by the light at each point of the (long) slit, the lines have a non-negligible curvature along the spatial direction. This curvature can induce relevant errors in our precise Doppler measurements and as such, it is corrected for.

4.2 Doppler Shifts

This section will list and explain the various steps required for the application of the Doppler velocimetry wind retrieval method.

As mentioned above, this technique relies on the measurement of Doppler shifts between absorption lines of simultaneously obtained spectra, so we are measuring relative velocities. This is so because absolute Doppler measurements require a stable velocity reference during acquisition with a grating spectrograph such as UVES, we cannot achieve the required accuracies (Machado et al., 2017).

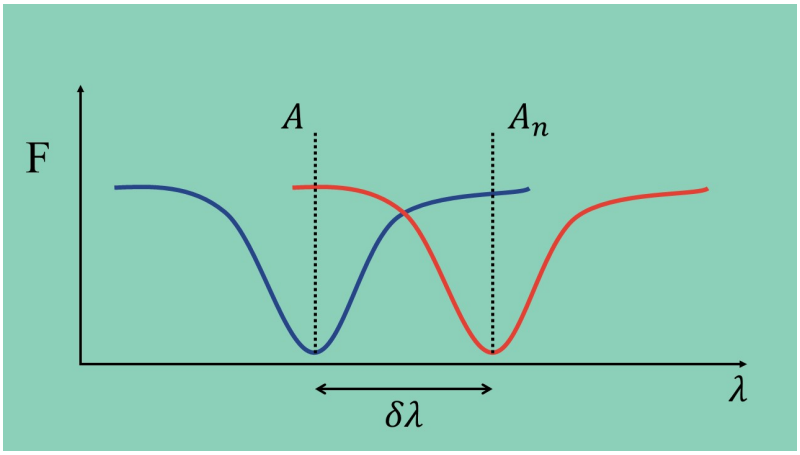

Figure 4.3: Algorithm for obtaining the radial velocity using only a single spectral line shift. Source: Machado (2014).

Assuming the Doppler shifts were retrieved based on one line's Doppler deviation, the basic Doppler shift equation is:

$$\frac{\delta V_n}{c} = \frac{\delta\lambda}{\lambda} \tag{4.1}$$

where δV_n is the Doppler velocity between the shifted and reference line, c is the speed of light in vacuum and λ is the wavelength of the deviated line. Since the shift $I_n - I$ - where I_n is the location of the shifted line and I the position of the same line in the reference spectrum - is much smaller than the line width we can take Taylor's first-order approximation:

$$I_n - I = \frac{\partial I}{\partial\lambda}\delta\lambda \tag{4.2}$$

Combining equation 4.1 and 4.2 yields the relative velocity between the reference and shifted line:

$$\frac{\delta V_n}{c} = \frac{I_n - I}{\lambda \frac{\partial I}{\partial \lambda}} \tag{4.3}$$

Since the Doppler shifts are relative - obtained between two spectra retrieved at the same time at different pixels of the slit - it is convenient to express the above result (4.3) as a function of the slit's pixels:

$$\delta v_i = \frac{c}{\lambda(i)} \delta \lambda_i = \frac{I(i) - I_o(i)}{\frac{\lambda(i)}{c} (\frac{\partial I_o}{\partial \lambda})_{\lambda = \lambda(i)}} \tag{4.4}$$

The i index refers to the pixel of the shifted spectrum along the slit, o refers to the reference pixel. All the Doppler measurements in this work were made using the 39^{th} pixel/spectrum as the reference pixel/spectrum. This pixel corresponds to the closest position of the slit to the half phase angle point $(\Phi/2)$.

The procedure described above can retrieve relative velocities by measuring the Doppler shift of one absorption line. However with single line fitting, for the velocities that we are trying to measure (of the order of $10ms^{-1}$) we would require a spectral resolution of approximately 10^6 to obtain the appropriate accuracies of the measured velocities.

The solution is the application of this procedure to a set of absorption lines (the Fraunhofer lines) over the wavelength ranges $480 - 570nm$ (blue region) and $580 - 680nm$ (red region) instead of a single line. The visible solar spectrum contains approximately 4400 solar lines.

The various measured single-line Doppler shifts are then averaged:

$$\delta v = \frac{\sum_i \delta v_i \omega_i}{\sum_i \omega_i} \tag{4.5}$$

Where the weights ω_i are are the inverse of each individual line velocity contribution variance:

$$\omega_i = \frac{1}{\sigma^2(\delta v_i)} \tag{4.6}$$

We must assume that the noise is only of photogenic origin (due to the poissonian nature of photons) so the we can determinate each line's velocity variance contribution $\sigma(\delta v_i)$. We can then calculate the overall uncertainty of the Doppler velocity determination - comes mainly from the dispersion relation uncertainty - to be:

$$\sigma(\delta v_i) = \frac{1}{\sqrt{\sum_i \omega_i}} \tag{4.7}$$

For each exposure, the velocity profile has been measured as a weighted average of shifts for the various spectral orders. Hence, through this procedure, we can determine the Doppler velocity due to shifts of lines between different points of the disk. These Doppler shifts do not, however, represent wind velocities as there are several effects and observational biases that need to be accounted for and corrected.

4.3 De-projection and Removal of Spurious Doppler Shifts

Doppler shifts are measured between different spectra, however, these still have to be corrected and localized within the planet in order to provide useful information about relative wind speeds. As wind Doppler measurements on Mars in the visible wavelength range have never been done before we relied on the experience of the Solar System's group in applying this method to other planets (Machado, 2014; Silva et al., 2018).

There are two major observational biases that need to be taken into account: the geometric de-projection factor and the Young effect. The geometric de-projection factor originates from the geometry of the observations as the Doppler velocity that we measure is a projection of the real velocity. The Young effect is a bias that arises from the fact that the Sun has a finite angular size when seen from almost any planet (including Mars) combined with the rotation velocity of the Sun ($\approx 2kms^{-1}$ at the equator). This means that the points we observe along the Martian disk may not be equally illuminated since the approaching and receding sides of the solar disk do not illuminate in an equal fashion (Gabsi, Bertaux, Hauchecorne, Schmitt, & Guibert, 2008).

The spectrum absorption lines are shifted by processes other than wind. The velocity between the Earth and Mars (orbital motion), the rotational velocity of the planet ($\approx 240ms^{-1}$) and the motion of the dust (wind) all contribute to the line-of-sight Doppler shift:

$$\Delta V = F \cdot (WS + RS) + Y + OS \tag{4.8}$$

Equation 4.8 shows the Doppler shift measured along the line of sight at any point of the slit. ΔV is the total measured Doppler shift, F is the geometric de-projection factor, WS is the shift caused by relative motion of the dust, RS is the shift due to the planetary rotation, Y is the shift due to the Young effect and OS is the shift that arises from the relative motion between Mars and Earth. However the orbital shift - which is induced by the relative motion between Mars and Earth - is the same for any two spectra that were obtained simultaneously. Consequently, it needs no correction as it is canceled out when measuring relative Doppler shifts.

The Young effect was first reported in Young (1975) as he noticed that points near the terminator of Venus were affected by a systematic effect as a consequence of not being equally illuminated by both the approaching and receding side of the Sun. Gabsi et al. (2008) approximated this effect empirically by:

$$Y \approx \frac{V_o D_o}{\sin\theta} \tag{4.9}$$

Where V_o is the solar equatorial velocity, D_o is the solar angular diameter and θ the angular distance between the point being observed and the terminator (centered on the center of Mars).

For our observations of Mars, the smallest angular distance between the point being observed and the terminator was of approximately $60°$. For these ($\theta = 60° - 90°$) values I computed equation 4.9 and estimated the Young effect affecting our Doppler shifts. The Young effect affecting the observations is always less than $1m/s$ and therefore can be considered negligible for the purposes of this work and warrants no correction.

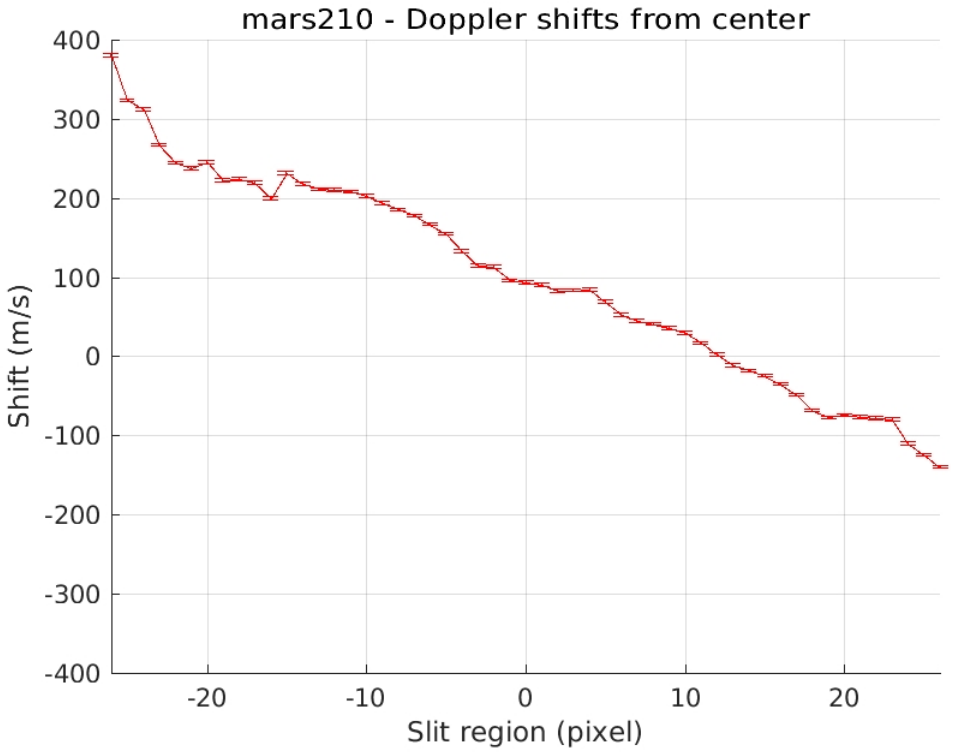

Figure 4.4: Raw Doppler velocities (MIT) retrieved using the Doppler velocimetry method as a function of pixel.

In this point of the algorithm, we have isolated the projected velocities which include the wind and rotation velocities and require de-projection (see Figure 4.4).

The Doppler shifts are computed between two points of the same slit (the chosen pixel and the reference pixel). However, due to the spherical geometry of Mars, points belonging to the same slit will fall on different latitudes. A direct consequence of this is that every pixel has a different rotation velocity and therefore contributes differently to the total shift. Thus this effect is not canceled when measuring the shift between spectra obtained simultaneously on different points of the slit and requires correction.

The approach used to remove the rotation velocity was one of the statistical nature. The first step was to perform a linear regression of the Doppler velocities to find the straight line that best fits the data and to estimate the rotation velocity. Through this process we computed the wind velocity for each pixel. This was completed for each of the exposures.

Additionally, we computed the rotation velocity, under the assumption of rigid body rotation and sub-

tracted them to the Doppler shift. The resulting velocities were in general agreement with our previously obtained results, validating our approach.

As we are trying to measure Doppler shifts induced by the motion of dust particles in the middle atmosphere of Mars. By assuming the single scattering approximation and considering the scattering process as a sequence of absorption and re-emission by dust particles in the upper dust cloud deck we can compute a correction factor as a function of longitude.

As a simplification, we assume, as a first approximation, that the motion is parallel to the equator and a $90°$ phase angle, two extreme cases can be considered (see Figure 4.5). One, at the sub-solar point, where there is no Doppler shift in the absorption (null incidence angle) but there is a blue-shift in re-emission towards Earth. The other, at the sub-terrestrial point, is the converse situation where there is a red-shift at absorption ($90°$ incidence angle), but no shift in the emission towards the Earth (in the direction normal to the surface).

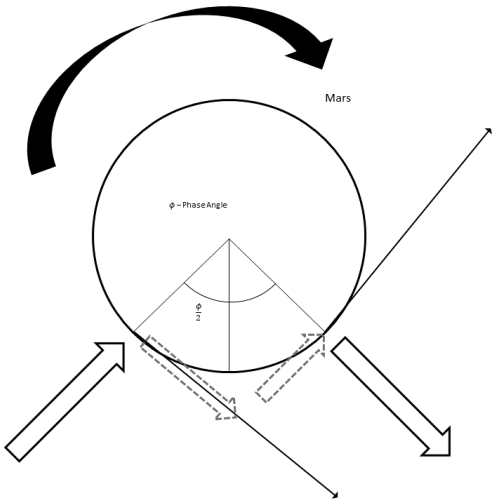

Figure 4.5: Schematics of the Doppler effect in the single scattering approximation. The dotted arrow at the sub terrestrial point indicates a red-shift in the absorption of solar radiation by the atmospheric aerosols in this region, due to the atmosphere's retrograde rotation. The dashed arrow at the sub-solar point indicates a blue-shift in the solar radiation scattered towards the observer. Thin arrows indicate the direction of the zonal wind.

According to Machado (2014); Gabsi et al. (2008), the exact geometric de-projection factor affecting the Doppler shift can be calculated by using the bisector theorem (see Equation 4.10). The line-of-sight Doppler shift is proportional to the projection of wind velocity on the bisector phase angle:

$$F = 2 \cdot cos(\frac{\Phi}{2}) sin(\phi - \frac{\Phi}{2}) cos(\beta) \tag{4.10}$$

Where Φ is the phase angle at the time of the observation, ϕ is the longitude of the point being measured, β is the latitude of the sub-terrestrial point. The line of sight Doppler shifts are proportional to the projection of the wind on the bisector of the phase angle. The phase angle Φ and the subterrestrial longitude β were retrieved from highly accurate ephemerides using NASA Jet Propulsion Laboratory's (JPL) HORIZONS web-interface system.

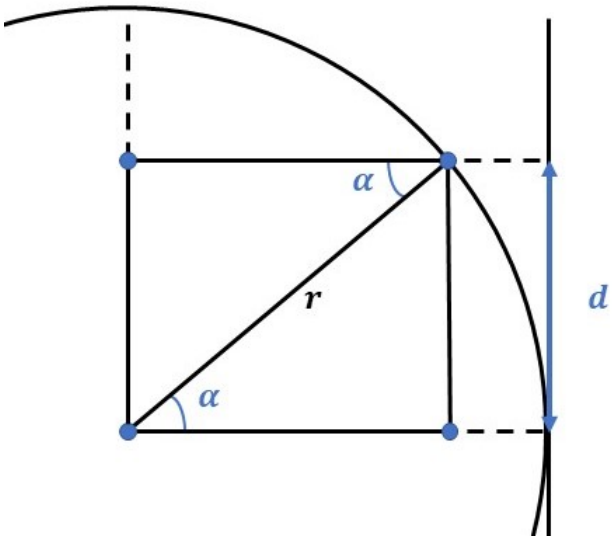

Figure 4.6: Representation of the determination of the longitude of our observations.

Each pixel's longitude (relative to the sub-earth point) was determined geometrically. Figure 4.6 shows a schematic of the geometry of the observation to determine the longitude of the observed points. Mars' angular radius on the night of the observation was $\approx 9.9''$ (see Table 3.2) and the our observations' pixel scale is 0.182. Assuming a radius of $r = 3396.19 \pm 0.1$ (Archinal et al., 2018) and using linear proportionality we can derive the distance between pixels (points observed) projected onto to a line tangent to the sub-terrestrial point to be $d \approx 62.5km$. The longitude - represented by α on Figure 4.6 - can then be determined using Tales theorem: $\alpha = arcsin(d/r)$.

For each observation and each pixel we computed the geometric de-projection factor and divided the line-of-sight Doppler shifts to obtain the true shifts (under the assumptions made). An example of the resulting velocities is shown in Figure 4.7. Next using the longitudes calculated following the scheme in Figure 4.6, we present the results as a function of longitude (see Figure 4.8).

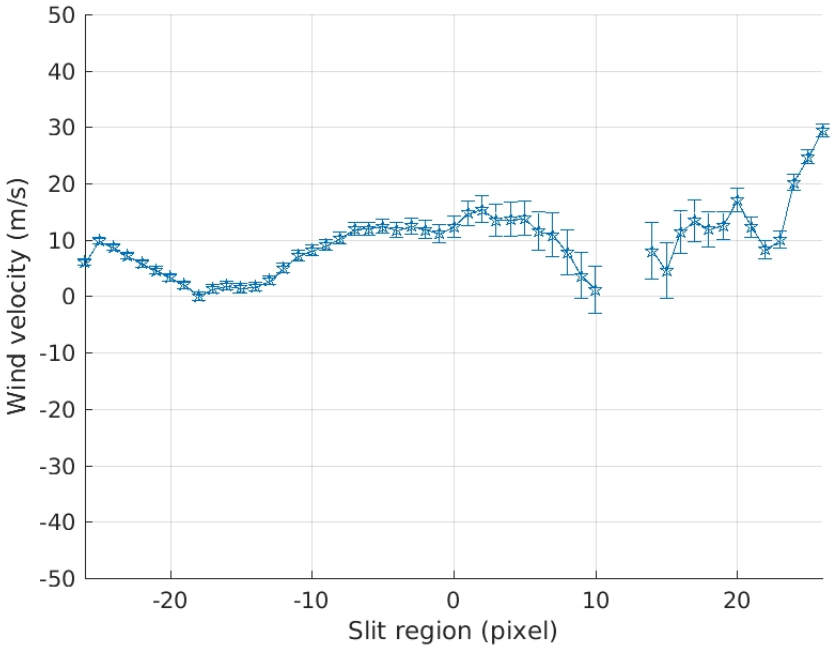

Figure 4.7: Example of measured Doppler wind velocities (MIT and EEV average) for one exposure as a function of the slit's pixel.

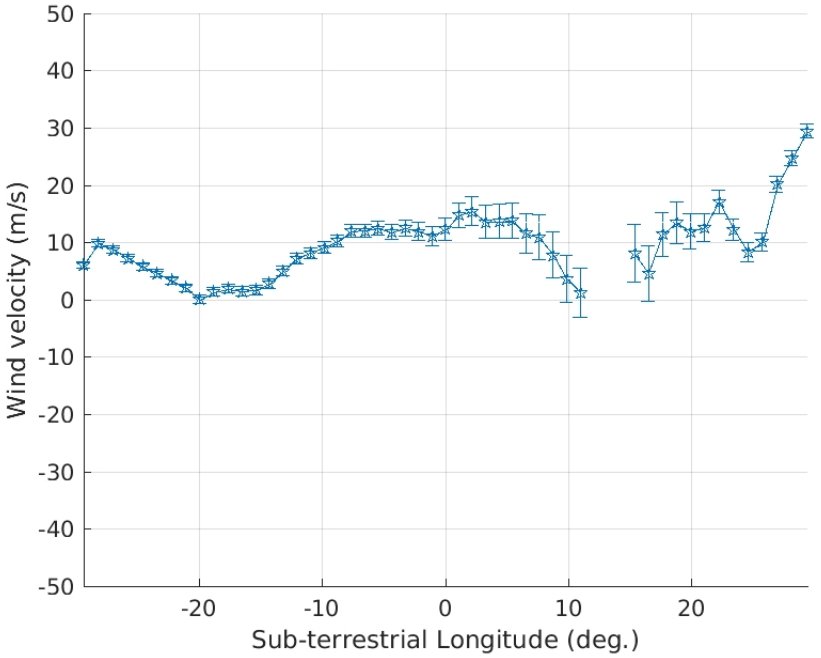

Figure 4.8: Example of measured Doppler wind velocities (MIT and EEV average) for one exposure as a function of sub-terrestrial longitude.

4.4 Results

This section is dedicated to the presentation of the wind velocity results that the aforementioned procedure has as an outcome.

The results presented are the average of the Doppler wind velocities retrieved through five consecutive exposures for the same positioning of the slit on the planetary disk (see Figure 4.9 (a), Figure 4.10 (a) and Figure 4.11 (a)). Furthermore, we present, along with the wind velocities, the positioning of the slit on the planetary disk for the 15 positions observed (see Figure 4.9 (b), Figure 4.10 (b) and Figure 4.11 (b)). Note that for reasons of space efficiency we present only three results in these sections and the remainder of the results in the Appendix A.

In general, the data shows internal consistency, as the velocities retrieved from each of the 5 observations made in the same position are consistent with each other. On the equatorial and subtropical latitudes, the wind velocities average around $1ms^{-1}$ increasing in magnitude towards higher latitudes in the northern hemisphere. This shows that there is some inter-latitudinal variability, this could be a consequence of the geometry of the observations (since the sub-terrestrial latitude was $-14.74°$). Furthermore, there is also a variation of magnitude and direction with longitude, implying some degree of local hour variability. This could be related to some residual planetary rotation contribution to the measured Doppler shift.

For the most part, the retrieved velocities lie in the range 10 - $30ms^{-1}$ however, the maximum velocity measured (in absolute value) was $116ms^{-1}$. However, it is likely that such elevated values are due to instrumental problems rather than actual wind.

On the equatorial and northern latitudes, the errors average approximately $2ms^{-1}$ however they increase substantially in the measurements made over the southern latitudes.

There is an identifiable structure to the Doppler velocities, showing similarities between closely positioned observations. This structure becomes increasingly erratic towards the southern latitudes.

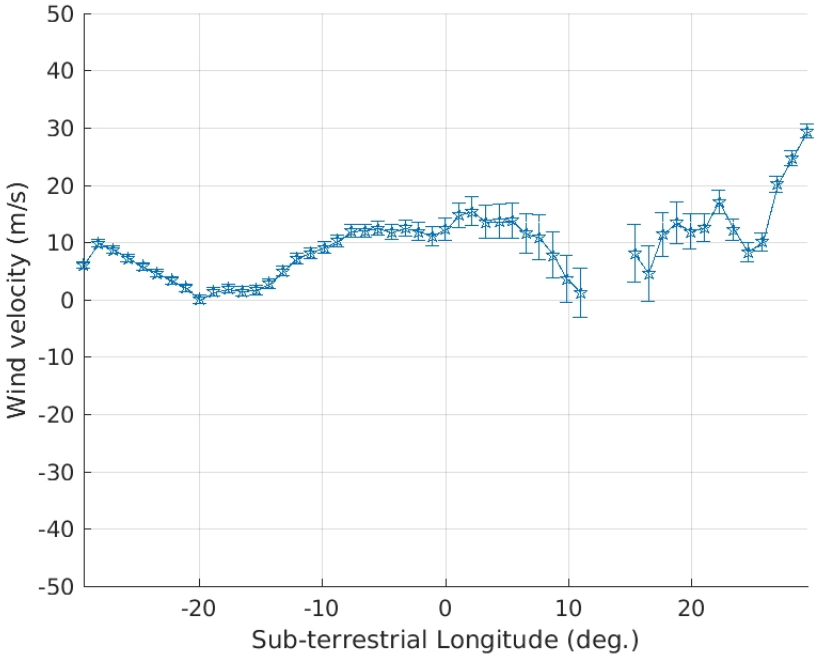

(a)

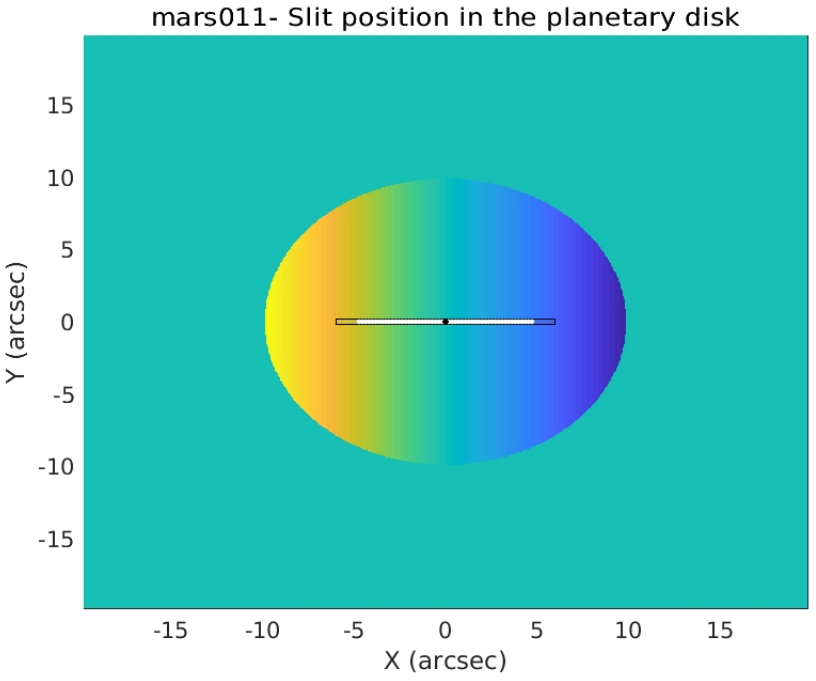

(b)

Figure 4.9: (a) Wind velocities along the slit position 1 ($Lat = -14.74°$). (b) Slit's position scheme on the planetary disk.

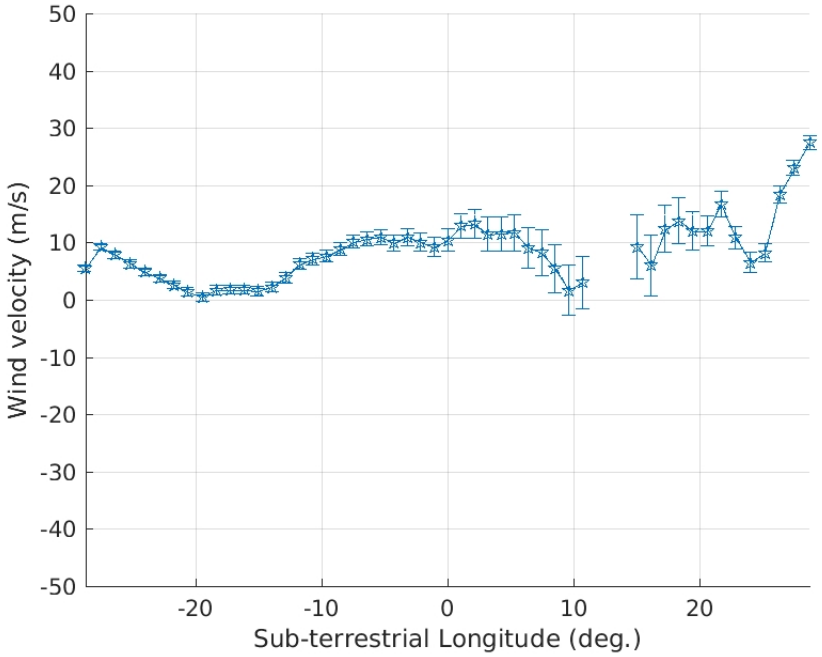

(a)

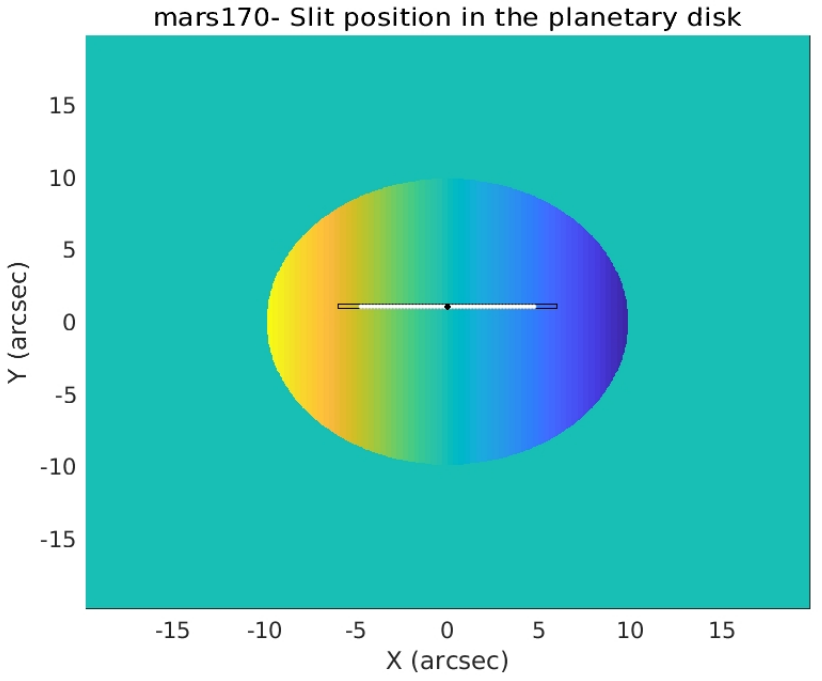

(b)

Figure 4.10: (a) Wind velocities along the slit position 2 ($Lat = 8.81°$). (b) Slit's position scheme on the planetary disk.

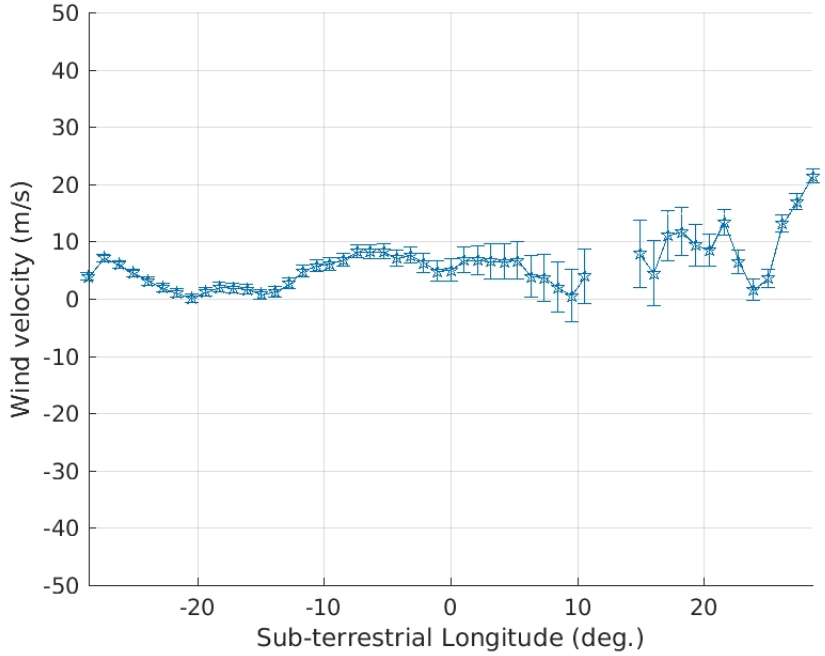

(a)

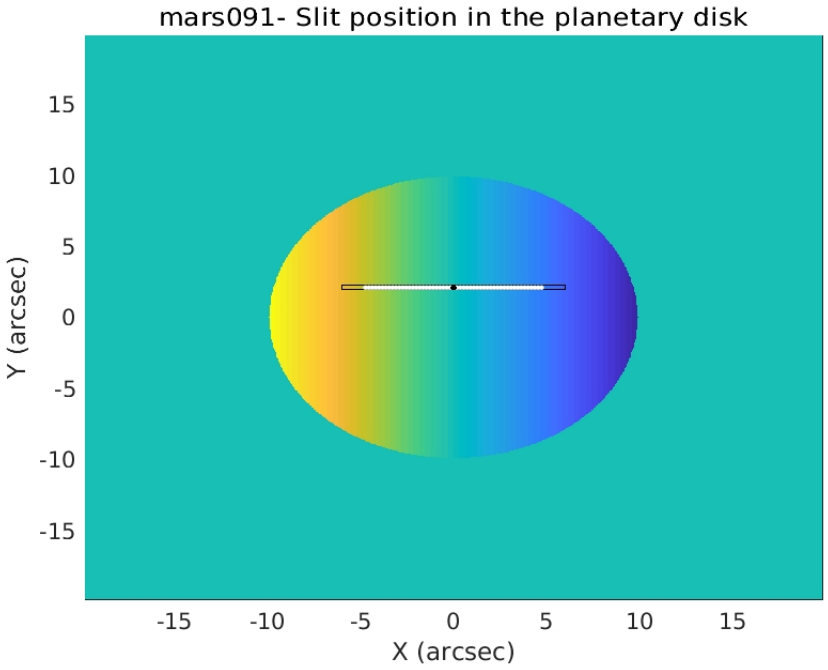

(b)

Figure 4.11: (a) Wind velocities along the slit position 3 ($Lat = -2.61°$). (b) Slit's position scheme on the planetary disk.

5 Conclusions and Prospects

For the first time a Doppler velocimetry method, based on ground-based long-slit high-resolution spectroscopy in the visible wavelength range, was applied to the study of the Martian atmosphere. We made the first attempt, ever, to measure instantaneous winds across an array of latitudes and longitudes with the intent of finding latitudinal and local time variability during a Martian global dust storm.

For this purpose we made use of the high-resolution spectrograph UVES at the VLT to perform our observations with the required resolution for this method to be effective ($\approx 100,000$). Our results are consistent with previous model results (Gilli et al., 2011) and show the potential this technique has, to improve and facilitate the study of global dust events on Mars. This is particularly significant since these events are still poorly understood in many aspects and are hard to investigate without using models, since the Mars' cloud coverage is sparse. However, it is important to note these results could be improved upon to be considered true accurate wind velocities.

The presented results shows some variability in the error's magnitude and the general structure of the wind velocities, particularly towards the southern latitudes. We have seen that the storm started and developed in the northern hemisphere, the opacity of the atmosphere was much greater than it was in the south. This could mean that there was insufficient suspended dust in the atmosphere for the light to effectively scatter. Therefore an increment in the error values and velocity structural variations may result from this.

The future work on this project contemplates several enhancements. A first priority is to use radiative transfer models to further constrain the altitude that we are sounding. Additionally, I will improve the subtraction of the planetary rotation's contribution to the total Doppler shifts.

In the next steps, I will pursue the identification and removal of pixels that have shown to be suffering from systematic problems. I also intend to seek the identification of the observations that are sounding different altitude (pressure) levels, this could add an additional dimension of data that can provide very valuable information. When all these steps are complete, our results will be prepared to be published and compared with global circulation models data.

References

Aoki, S., Giuranna, M., Sato, Y., Nakagawa, H., Sato, T. M., Wolkenberg, P., ... Kasaba, Y. (2016, Apr). Mesospheric CO2 ice clouds on Mars observed by Planetary Fourier Spectrometer onboard Mars Express. In *Egu general assembly conference abstracts* (Vol. 18, p. EPSC2016-8330).

Archinal, B. A., Acton, C. H., A'Hearn, M. F., Conrad, A., Consolmagno, G. J., Duxbury, T., ... Williams, I. P. (2018, Mar). Report of the IAU Working Group on Cartographic Coordinates and Rotational Elements: 2015. *Celestial Mechanics and Dynamical Astronomy*, *130*(3), 22. doi: 10.1007/s10569-017-9805-5

Atreya, S. K., & Gu, Z. G. (1995, Aug). Photochemistry and stability of the atmosphere of Mars. *Advances in Space Research*, *16*(6), 57-68. doi: 10.1016/0273-1177(95)00250-I

Baird, D. T. (2006, Dec). Zonal Winds at Reference Altitudes From MGS Aerobraking Data. In *Agu fall meeting abstracts* (Vol. 2006, p. P23A-0038).

Barabash, S., Lundin, R., Andersson, H., Gimholt, J., Holmström, M., Norberg, O., ... Bochsler, P. (2004, 07). Aspera-3: analyser of space plasmas and energetic ions for mars express. , *1240*, 121-139.

Barnes, J. R., Haberle, R. M., Wilson, R. J., Lewis, S. R., Murphy, J. R., & Read, P. L. (2017). The global circulation. In R. M. Haberle, R. T. Clancy, F. Forget, M. D. Smith, & R. W. Zurek (Eds.), *The atmosphere and climate of mars* (p. 229–294). Cambridge University Press. doi: 10.1017/9781139060172.009

Bertaux, J.-L., Fonteyn, D., Korablev, O., Chassefre, E., Dimarellis, E., P. Dubois, J., ... Stern, A. (2004, 08). Spicam: studying the global structure and composition of the martian atmosphere. *European Space Agency, (Special Publication) ESA SP*, 95-120.

Bertrand, T., Wilson, R. J., & Kahre, M. A. (2019, Jul). Simulation of the 2018 Global Dust Storm on Mars Using the NASA Ames Mars GCM: A Multi-Tracer Approach. *LPI Contributions*, *2089*, 6284.

Bibring, J.-P. (2004, 01). Omega: Observatoire pour la minéralogie, l'eau, les glaces et l'activité. *Mars Express: The Scientific Payload*, 37-49.

Biswal M, M. K., & Annavarapu, R. N. (2019, 01). *Chronology of mars exploration missions.* doi: 10.13140/RG.2.2.36435.22560

Bougher, S. W., Brain, D. A., Fox, J. L., Francisco, G.-G., Simon-Wedlund, C., & Withers, P. G. (2017). Upper neutral atmosphere and ionosphere. In R. M. Haberle, R. T. Clancy, F. Forget, M. D. Smith, & R. W. Zurek (Eds.), *The atmosphere and climate of mars* (p. 433–463). Cambridge University Press. doi: 10.1017/9781139060172.014

Brown, A. J., Wolff, M. J., & Scargle, J. D. (2015, Jan). Correlations of atmospheric water ice and dust in the Martian Polar regions. *arXiv e-prints*, arXiv:1501.03802.

Cantor, B. A. (2003, Jul). MGS-MOC Observations of Martian Dust Storm Activity. In A. L. Albee & H. H. Kieffer (Eds.), *Sixth international conference on mars* (p. 3166).

Cantor, B. A. (2007, Jan). MOC observations of the 2001 Mars planet-encircling dust storm. *Icarus*, *186*(1), 60-96. doi: 10.1016/j.icarus.2006.08.019

Cantor, B. A., James, P. B., Caplinger, M., & Wolff, M. J. (2001, Oct). Martian dust storms: 1999 Mars Orbiter Camera observations. *Journal of Geophysical Research (Planets)*, *106*(E10), 23653-23688. doi: 10.1029/2000JE001310

Cavalié, T., Billebaud, F., Encrenaz, T., Dobrijevic, M., Brillet, J., Forget, F., & Lellouch, E. (2008,

Oct). Vertical temperature profile and mesospheric winds retrieval on Mars from CO ;millimeter observations. Comparison with general circulation model predictions. *Astronomy & Astrophysics*, *489*(2), 795-809. doi: 10.1051/0004-6361:200809815

Chow, K.-C., Xiao, J., Chan, K. L., & Wong, C.-F. (2019). Flow associated with the condensation and sublimation of polar ice caps on mars. *Journal of Geophysical Research: Planets*, *124*(6), 1570-1580. doi: 10.1029/2018JE005848

Christensen, P. R. (1986, Mar). Regional dust deposits on Mars - Physical properties, age, and history. *Journal of Geophysics Research*, *91*, 3533-3545. doi: 10.1029/JB091iB03p03533

Civeit, T., Appourchaux, T., Lebreton, J. P., Luz, D., Courtin, R., Neiner, C., ... Gautier, D. (2005, Mar). On measuring planetary winds using high-resolution spectroscopy in visible wavelengths. *Astronomy and Astrophysics*, *431*(3), 1157-1166. doi: 10.1051/0004-6361:20041640

Clancy, R. T., Grossman, A. W., Wolff, M. J., James, P. B., Rudy, D. J., Billawala, Y. N., ... Muhleman, D. O. (1996, Jul). Water Vapor Saturation at Low Altitudes around Mars Aphelion: A Key to Mars Climate? *Icarus*, *122*(1), 36-62. doi: 10.1006/icar.1996.0108

Clancy, R. T., Montmessin, F., Benson, J., Daerden, F., Colaprete, A., & Wolff, M. J. (2017). Mars clouds. In R. M. Haberle, R. T. Clancy, F. Forget, M. D. Smith, & R. W. Zurek (Eds.), *The atmosphere and climate of mars* (p. 76–105). Cambridge University Press. doi: 10.1017/9781139060172.005

Clancy, R. T., Sandor, B. J., Moriarty-Schieven, G. H., & Smith, M. D. (2006, Feb). Mesospheric winds and temperatures from JCMT sub-millimeter CO line observations during the 2003 and 2005 Mars oppositions. In F. Forget et al. (Eds.), *Mars atmosphere modelling and observations* (p. 135).

Clayton, M. (1996, Dec). *Introduction to Echelle Spectroscopy.*

Colaprete, A., & Toon, O. B. (2000, Jun). The Radiative Effects of Martian Water Ice Clouds on the Local Atmospheric Temperature Profile. *Icarus*, *145*(2), 524-532. doi: 10.1006/icar.2000.6364

Connes, P. (1985, Mar). Absolute Astronomical Accelerometry. *Astrophysics & Space Science*, *110*(2), 211-255. doi: 10.1007/BF00653671

Dekker, H., D'Odorico, S., Kaufer, A., Delabre, B., & Kotzlowski, H. (2000, Aug). Design, construction, and performance of UVES, the echelle spectrograph for the UT2 Kueyen Telescope at the ESO Paranal Observatory. In M. Iye & A. F. Moorwood (Eds.), (Vol. 4008, p. 534-545). doi: 10.1117/12.395512

D'Odorico, S., Cristiani, S., Dekker, H., Hill, V., Kaufer, A., Kim, T., & Primas, F. (2000, Jun). Performance of UVES, the echelle spectrograph for the ESO VLT and highlights of the first observations of stars and quasars. In J. Bergeron (Ed.), *Proceedings of the spie* (Vol. 4005, p. 121-130). doi: 10.1117/12.390133

Dorn, R. J., Beletic, J. W., Cavadore, C., & Lizon, J.-L. (2000, Aug). Optical detector systems of UVES: the echelle spectrograph for the UT2 Kueyen Telescope at the ESO Paranal Observatory. In M. Iye & A. F. Moorwood (Eds.), *Proceedings of the international society for optical engineering* (Vol. 4008, p. 344-355). doi: 10.1117/12.395492

ESA. (2017). *Mars express european space agency page.* Retrieved 2019-07-21, from `http://www.esa.int/Our_Activities/Space_Science/Mars_Express`

Formisano, V., Grassi, D., Orfei, R., Biondi, D., Mencarelli, E., Mattana, A., ... Gobbi, P. (2004, 07). Pfs: the planetary fourier spectrometer for mars express. *European Space Agency, (Special Publication) ESA SP*, *1240*, 71-94.

French, R. G., Gierasch, P. J., Popp, B. D., & Yerdon, R. J. (1981, Feb). Global patterns in cloud forms on Mars. *Icarus*, *45*(2), 468-493. doi: 10.1016/0019-1035(81)90047-6

Gabsi, Y., Bertaux, J. L., Hauchecorne, A., Schmitt, J., & Guibert, S. (2008, Oct). Measuring Venus' winds using the Absolute Astronomical Accelerometer: Solid super-rotation model of Venus' clouds. *Planetary Space Science*, *56*(11), 1454-1466. doi: 10.1016/j.pss.2008.07.016

Gichu, R., & Ogohara, K. (2019, Feb). Segmentation of dust storm areas on Mars images using principal component analysis and neural network. *Progress in Earth and Planetary Science*, *6*(1), 19. doi: 10.1186/s40645-019-0266-1

Gierasch, P. J., & Goody, R. M. (1972, Jan). The effect of dust on the temperature of the Martian atmosphere. *Journal of Atmospheric Sciences*, *29*, 400-402. doi: 10.1175/1520-0469(1972)029<0400:TEODOT>2.0.CO;2

Gilli, G., López-Valverde, M. A., Funke, B., López-Puertas, M., Drossart, P., Piccioni, G., & Formisano, V. (2011, Aug). Non-LTE CO limb emission at 4.7μm in the upper atmosphere of Venus, Mars and Earth: Observations and modeling. *Planetary Space Science*, *59*(10), 1010-1018. doi: 10.1016/j.pss.2010.07.023

Giuranna, M., Viscardy, S., Daerden, F., Neary, L., Etiope, G., Oehler, D., ... Aoki, S. (2019, Apr). Independent confirmation of a methane spike on Mars and a source region east of Gale Crater. *Nature Geoscience*, *12*(5), 326-332. doi: 10.1038/s41561-019-0331-9

Grima, C., Kofman, W., Mouginot, J., Phillips, R. J., Hérique, A., Biccari, D., ... Cutigni, M. (2009, Feb). North polar deposits of Mars: Extreme purity of the water ice. *Geophysics Research Letters*, *36*(3), L03203. doi: 10.1029/2008GL036326

Guzewich, S. D., Lemmon, M., Smith, C. L., Martínez, G., de Vicente-Retortillo, Á., Newman, C. E., ... Zorzano Mier, M.-P. (2019, Jan). Mars Science Laboratory Observations of the 2018/Mars Year 34 Global Dust Storm. *Geophysics Research Letters*, *46*(1), 71-79. doi: 10.1029/2018GL080839

Haberle, R. (2015). Solar system/sun, atmospheres, evolution of atmospheres | planetary atmospheres: Mars. In G. R. North, J. Pyle, & F. Zhang (Eds.), *Encyclopedia of atmospheric sciences (second edition)* (Second Edition ed., p. 168 - 177). Oxford: Academic Press. Retrieved from `http://www.sciencedirect.com/science/article/pii/B9780123822253003121` doi: https://doi.org/10.1016/B978-0-12-382225-3.00312-1

Haberle, R. M. (1986). Interannual variability of global dust storms on mars. *Science*, *234*(4775), 459–461. doi: 10.1126/science.234.4775.459

Haberle, R. M., Clancy, R. T., Forget, F., Smith, M. D., & Zurek, R. W. (2017). *The atmosphere and climate of Mars*. doi: 10.1017/9781139060172

Haberle, R. M., Pollack, J. B., Barnes, J. R., Zurek, R. W., Leovy, C. B., Murphy, J. R., ... Schaeffer, J. (1993, Feb). Mars atmospheric dynamics as simulated by the NASA Ames General Circulation Model. 1. The zonal-mean circulation. *Journal of Geophysics Research*, *98*(E2), 3093-3123. doi: 10.1029/92JE02946

Herschel, W. (1784). Xix. on the remarkable appearances at the polar regions of the planet mars, and its spheroidical figure; with a few hints relating to its real diameter and atmosphere. *Philosophical Transactions of the Royal Society of London*, *74*, 233-273. doi: 10.1098/rstl.1784.0020

Hess, S. L., Henry, R. M., Leovy, C. B., Ryan, J. A., & Tillman, J. E. (1977, Sep). Meteorological results from the surface of Mars: Viking 1 and 2. *Journal of Geophysics Research*, *82*(B28), 4559-4574. doi: 10.1029/JS082i028p04559

Holstein-Rathlou, C., Gunnlaugsson, H. P., Merrison, J. P., Bean, K. M., Cantor, B. A., Davis, J. A., ... Taylor, P. A. (2010, 5). Winds at the phoenix landing site. *Journal of Geophysical Research: Planets (1991–2012)*, *115*(E5). doi: 10.1029/2009JE003411

Houben, H., Haberle, R. M., Young, R. E., & Zent, A. P. (1997, Apr). Modeling the Martian seasonal

water cycle. *Journal of Geophysics Research*, *102*(E4), 9069-9084. doi: 10.1029/97JE00046

Jakosky, B. M., Slipski, M., Benna, M., Mahaffy, P., Elrod, M., Yelle, R., ... Alsaeed, N. (2017, Mar). Mars' atmospheric history derived from upper-atmosphere measurements of ^{38}Ar/^{36}Ar. *Science*, *355*(6332), 1408-1410. doi: 10.1126/science.aai7721

James, P. B., Christensen, P. R., Clancy, R. T., Lemmon, M. T., & Withers, P. (2017). History of mars atmosphere observations. In R. M. Haberle, R. T. Clancy, F. Forget, M. D. Smith, & R. W. Zurek (Eds.), *The atmosphere and climate of mars* (p. 20–41). Cambridge University Press. doi: 10.1017/9781139060172.003

Kahn, R. (1983, Dec). Some observational constraints on the global-scale wind systems of Mars. *Journal of Geophysics Research*, *88*(A12), 10189-10209. doi: 10.1029/JA088iA12p10189

Kahre, M., Murphy, J., & Haberle, R. (2006, 06). Modeling the martian dust cycle and surface dust reservoirs with the nasa ames general circulation model. *Journal of Geophysical Research*, *111*. doi: 10.1029/2005JE002588

Kahre, M. A., & Haberle, R. M. (2010, Jun). Mars CO $_2$ cycle: Effects of airborne dust and polar cap ice emissivity. *Icarus*, *207*(2), 648-653. doi: 10.1016/j.icarus.2009.12.016

Kahre, M. A., Murphy, J. R., Newman, C. E., Wilson, R. J., Cantor, B. A., Lemmon, M. T., & Wolff, M. J. (2017). The mars dust cycle. In R. M. Haberle, R. T. Clancy, F. Forget, M. D. Smith, & R. W. Zurek (Eds.), *The atmosphere and climate of mars* (p. 295–337). Cambridge University Press. doi: 10.1017/9781139060172.010

Kass, D. M., Schofield, J. T., Kleinböhl, A., McCleese, D. J., Heavens, N. G., & Shirley, J. H. (2019, Jul). Mars Climate Sounder Observations of the 2018 Global Dust Event and Comparisons to Previous Events. *LPI Contributions*, *2089*, 6307.

Kaydash, V. G., Kreslavsky, M. A., Shkuratov, Y. G., Videen, G., Bell, J. F., & Wolff, M. (2006, Nov). Measurements of winds on Mars with Hubble Space Telescope images in 2003 opposition. *Icarus*, *185*(1), 97-101. doi: 10.1016/j.icarus.2006.07.017

Khayat, A. S. J., Smith, M. D., & Guzewich, S. D. (2019, Mar). Understanding the water cycle above the north polar cap on Mars using MRO CRISM retrievals of water vapor. *Icarus*, *321*, 722-735. doi: 10.1016/j.icarus.2018.12.024

Kloos, J. L., Moores, J. E., Whiteway, J. A., & Aggarwal, M. (2018, Jan). Interannual and Diurnal Variability in Water Ice Clouds Observed from MSL Over Two Martian Years. *Journal of Geophysical Research (Planets)*, *123*(1), 233-245. doi: 10.1002/2017JE005314

Krasnopolsky, V. A. (2010, Jun). Solar activity variations of thermospheric temperatures on Mars and a problem of CO in the lower atmosphere. *Icarus*, *207*(2), 638-647. doi: 10.1016/j.icarus.2009.12.036

Lefèvre, F., & Krasnopolsky, V. (2017). Atmospheric photochemistry. In R. M. Haberle, R. T. Clancy, F. Forget, M. D. Smith, & R. W. Zurek (Eds.), *The atmosphere and climate of mars* (p. 405–432). Cambridge University Press. doi: 10.1017/9781139060172.013

Leighton, R. B., & Murray, B. C. (1966, Jul). Behavior of Carbon Dioxide and Other Volatiles on Mars. *Science*, *153*(3732), 136-144. doi: 10.1126/science.153.3732.136

Lellouch, E., Goldstein, J. J., Bougher, S. W., Paubert, G., & Rosenqvist, J. (1991, Dec). First Absolute Wind Measurements in the Middle Atmosphere of Mars. *Astrophysical Journal*, *383*, 401. doi: 10.1086/170797

Lemmon, M. T., Wolff, M. J., Bell, I., James F., Smith, M. D., Cantor, B. A., & Smith, P. H. (2015, May). Dust aerosol, clouds, and the atmospheric optical depth record over 5 Mars years of the Mars Exploration Rover mission. *Icarus*, *251*, 96-111. doi: 10.1016/j.icarus.2014.03.029

Leovy, C. B., & Zurek, R. W. (1979, Jun). Thermal tides and Martian dust storms: direct evidence for coupling. *Journal of Geophysics Research*, *84*, 2956-2968. doi: 10.1029/JB084iB06p02956

Leovy, C. B., Zurek, R. W., & Pollack, J. B. (1973, Jan). Mechanisms for Mars dust storms. *Journal of Atmospheric Sciences*, *30*, 749-762. doi: 10.1175/1520-0469(1973)030<0749:MFMDS>2.0.CO;2

Lowell, P. (1906). *Mars and its Canals*.

Luz, D., Civeit, T., Courtin, R., Lebreton, J. P., Gautier, D., Rannou, P., ... Ferri, F. (2005, Dec). Characterization of zonal winds in the stratosphere of Titan with UVES. *Icarus*, *179*(2), 497-510. doi: 10.1016/j.icarus.2005.07.021

Luz, D., Civeit, T., Courtin, R., Lebreton, J. P., Gautier, D., Witasse, O., ... Kostiuk, T. (2006, Aug). Characterization of zonal winds in the stratosphere of Titan with UVES: 2. Observations coordinated with the Huygens Probe entry. *Journal of Geophysical Research (Planets)*, *111*(E8), E08S90. doi: 10.1029/2005JE002617

Määttänen, A., Montmessin, F., Gondet, B., Scholten, F., Hoffmann, H., González-Galindo, F., ... Neukum, G. (2010, Oct). Mapping the mesospheric CO $_2$ clouds on Mars: MEx/OMEGA and MEx/HRSC observations and challenges for atmospheric models. *Icarus*, *209*(2), 452-469. doi: 10.1016/j.icarus.2010.05.017

Machado, P. (2014). *Dynamics of Venus' Atmosphere: Characterization of its Global Circulation with Doppler velocimetry*.

Machado, P., Luz, D., Widemann, T., Lellouch, E., & Witasse, O. (2012, Sep). Mapping zonal winds at Venus's cloud tops from ground-based Doppler velocimetry. *Icarus*, *221*(1), 248-261. doi: 10.1016/j.icarus.2012.07.012

Machado, P., Widemann, T., Luz, D., & Peralta, J. (2014, Nov). Wind circulation regimes at Venus' cloud tops: Ground-based Doppler velocimetry using CFHT/ESPaDOnS and comparison with simultaneous cloud tracking measurements using VEx/VIRTIS in February 2011. *Icarus*, *243*, 249-263. doi: 10.1016/j.icarus.2014.08.030

Machado, P., Widemann, T., Peralta, J., Gonçalves, R., Donati, J.-F., & Luz, D. (2017, Mar). Venus cloud-tracked and doppler velocimetry winds from CFHT/ESPaDOnS and Venus Express/VIRTIS in April 2014. *Icarus*, *285*, 8-26. doi: 10.1016/j.icarus.2016.12.017

Mackwell, S. J., Simon-Miller, A. A., Harder, J. W., & Bullock, M. A. (2013). *Comparative Climatology of Terrestrial Planets*. doi: 10.2458/azu_uapress_9780816530595

McCleese, D. J., Heavens, N. G., Schofield, J. T., Abdou, W. A., Bandfield, J. L., Calcutt, S. B., ... Zurek, R. W. (2010). Structure and dynamics of the martian lower and middle atmosphere as observed by the mars climate sounder: Seasonal variations in zonal mean temperature, dust, and water ice aerosols. *Journal of Geophysical Research: Planets*, *115*(E12). doi: 10.1029/2010JE003677

McCleese, D. J., Schofield, J. T., Taylor, F. W., Abdou, W. A., Aharonson, O., Banfield, D., ... Kass, D. M. (2008, Nov). Intense polar temperature inversion in the middle atmosphere on Mars. *Nature Geoscience*, *1*(11), 745-749. doi: 10.1038/ngeo332

McConnochie, T. H., Bell, J. F., Savransky, D., Wolff, M. J., Toigo, A. D., Wang, H., ... Christensen, P. R. (2010, Dec). THEMIS-VIS observations of clouds in the martian mesosphere: Altitudes, wind speeds, and decameter-scale morphology. *Icarus*, *210*(2), 545-565. doi: 10.1016/j.icarus.2010.07.021

McElroy, M. B., & Donahue, T. M. (1972, Sep). Stability of the Martian Atmosphere. *Science*, *177*(4053), 986-988. doi: 10.1126/science.177.4053.986

Mellon, M. T., Feldman, W. C., & Prettyman, T. H. (2004, Jun). The presence and stability of ground ice in the southern hemisphere of Mars. *Icarus*, *169*(2), 324-340. doi: 10.1016/j.icarus.2003.10.022

Mellon, M. T., & Jakosky, B. M. (1993, Feb). Geographic variations in the thermal and diffusive stability of ground ice on Mars. *Journal of Geophysics Research*, *98*(E2), 3345-3364. doi: 10.1029/92JE02355

Mischna, M. A., Bell, I., James F., James, P. B., & Crisp, D. (1998, Jan). Synoptic measurements of Martian winds using the Hubble Space Telescope. *Geophysics Research Letters*, *25*(5), 611-614. doi: 10.1029/98GL50358

Montabone, L., Forget, F., Millour, E., Wilson, R. J., Lewis, S. R., Cantor, B., ... Wolff, M. J. (2015, May). Eight-year climatology of dust optical depth on Mars. *Icarus*, *251*, 65-95. doi: 10.1016/j.icarus.2014.12.034

Montmessin, F., Forget, F., Rannou, P., Cabane, M., & Haberle, R. M. (2004, Oct). Origin and role of water ice clouds in the Martian water cycle as inferred from a general circulation model. *Journal of Geophysical Research (Planets)*, *109*(E10), E10004. doi: 10.1029/2004JE002284

Montmessin, F., Smith, M. D., Langevin, Y., Mellon, M. T., & Fedorova, A. (2017). The water cycle. In R. M. Haberle, R. T. Clancy, F. Forget, M. D. Smith, & R. W. Zurek (Eds.), *The atmosphere and climate of mars* (p. 338–373). Cambridge University Press. doi: 10.1017/9781139060172.011

Moreno, R., Lellouch, E., Forget, F., Encrenaz, T., Guilloteau, S., & Millour, E. (2009, Jun). Wind measurements in Mars' middle atmosphere: IRAM Plateau de Bure interferometric CO observations. *Icarus*, *201*(2), 549-563. doi: 10.1016/j.icarus.2009.01.027

Nasa mars science laboratory landing press kit. (2012).

Neakrase, L. D. V., & Greeley, R. (2010, Mar). Dust devil sediment flux on Earth and Mars: Laboratory simulations. *Icarus*, *206*(1), 306-318. doi: 10.1016/j.icarus.2009.08.028

Neukum, G., & Jaumann, R. (2004, 01). Hrsc: The high resolution stereo camera of mars express. *Eur. Space Agency Spec. Publ.*, *1240*, 17-35.

Ojha, L., Lewis, K., Karunatillake, S., & Schmidt, M. (2018, Jul). The Medusae Fossae Formation as the single largest source of dust on Mars. *Nature Communications*, *9*, 2867. doi: 10.1038/s41467-018-05291-5

Orosei, R., Lauro, S. E., Pettinelli, E., Cicchetti, A., Coradini, M., Cosciotti, B., ... Pajola, M. (2018, Aug). Radar evidence of subglacial liquid water on Mars. *Science*, *361*(6401), 490-493. doi: 10.1126/science.aar7268

Paige, D. A., & Ingersoll, A. P. (1985, Jun). Annual Heat Balance of Martian Polar Caps: Viking Observations. *Science*, *228*(4704), 1160-1168. doi: 10.1126/science.228.4704.1160

Patzold, M., M. Neubauer, F., Carone, L., Hagermann, A., Stanzel, C., Hausler, B., ... Dehant, V. (2004, 08). Mars: Mars express orbiter radio science. *European Space Agency, (Special Publication) ESA SP*.

Perko, H., Nelson, J., & Green, J. (2002, 01). Review of martian dust composition, transport, deposition, adhesion, and removal..

Phillips, R. J., Davis, B. J., Tanaka, K. L., Byrne, S., Mellon, M. T., Putzig, N. E., ... Carter, L. M. (2011, May). Massive CO_2 Ice Deposits Sequestered in the South Polar Layered Deposits of Mars. *Science*, *332*(6031), 838. doi: 10.1126/science.1203091

Picardi, G., Biccari, D., Seu, R., Plaut, J., T. K. Johnson, W., Jordan, R., ... Calabrese, D. (2004, 08). Marsis: Mars advanced radar for subsurface and ionosphere sounding. *European Space Agency, (Special Publication) ESA SP*.

Pollack, J. B., Colburn, D. S., Flasar, F. M., Kahn, R., Carlston, C. E., & Pidek, D. G. (1979, Jun). Prop-

erties and effects of dust particles suspended in the Martian atmosphere. *Journal of Geophysics Research*, *84*, 2929-2945. doi: 10.1029/JB084iB06p02929

Pollack, J. B., Haberle, R. M., Schaeffer, J., & Lee, H. (1990, Feb). Simulations of the general circulation of the Martian atmosphere. 1. Polar processes. *Journal of Geophysics Research*, *95*, 1447-1473. doi: 10.1029/JB095iB02p01447

Read, P., & Lewis, S. (2006, 03). Book review: the martian climate revisited: Atmosphere and environment of a desert planet/springer, 2004. *Astronomy and Geophysics*, *46*, 39.

Richardson, M. I., & Wilson, R. J. (2002, May). Investigation of the nature and stability of the Martian seasonal water cycle with a general circulation model. *Journal of Geophysical Research (Planets)*, *107*(E5), 5031. doi: 10.1029/2001JE001536

Sbordone, L., & Ledoux, C. (2017, 08). Uv-visual echelle spectrograph user manual (VLT MAN ESO 13200 1825 Issue 101 ed.) [Computer software manual]. ESO - European Southern Observatory, Karl-Schwarzschild Str. 2, D-85748 Garching bei Munchen.

Schofield, J. T., Barnes, J. R., Crisp, D., Haberle, R. M., Larsen, S., Magalhaes, J. A., ... Wilson, G. (1997, Dec). The Mars Pathfinder Atmospheric Structure Investigation/Meteorology. *Science*, *278*, 1752. doi: 10.1126/science.278.5344.1752

Sheehan, W. (1996a). *The planet Mars: a history of observation and discovery*.

Sheehan, W. (1996b). *The planet Mars: a history of observation and discovery*.

Silva, M., Machado, P., Sánchez-Lavega, A., Hueso, R., Luz, D., & Peralta, J. (2018, Sep). Ground-based Doppler Velocimetry: wind measurements in Saturn's atmosphere with UVES/VLT. In *European planetary science congress* (p. EPSC2018-374).

Smith, D. E., Zuber, M. T., Solomon, S. C., Phillips, R. J., Head, J. W., Garvin, J. B., ... Neumann, G. A. (1999, May). The Global Topography of Mars and Implications for Surface Evolution. *Science*, *284*, 1495. doi: 10.1126/science.284.5419.1495

Smith, M., Wolff, M., Clancy, R., Kleinböhl, A., & Murchie, S. (2013, 02). Vertical distribution of dust and water ice aerosols from crism limb-geometry observations. *Journal of Geophysical Research (Planets)*, *118*, 321-334. doi: 10.1002/jgre.20047

Smith, M. D. (2002, Nov). The annual cycle of water vapor on Mars as observed by the Thermal Emission Spectrometer. *Journal of Geophysical Research (Planets)*, *107*(E11), 5115. doi: 10.1029/2001JE001522

Smith, M. D. (2008, May). Spacecraft Observations of the Martian Atmosphere. *Annual Review of Earth and Planetary Sciences*, *36*, 191-219. doi: 10.1146/annurev.earth.36.031207.124334

Smith, M. D. (2009). Themis observations of mars aerosol optical depth from 2002–2008. *Icarus*, *202*(2), 444 - 452. doi: https://doi.org/10.1016/j.icarus.2009.03.027

Smith, M. D., Bougher, S. W., Encrenaz, T., Forget, F., & Kleinböhl, A. (2017). Thermal structure and composition. In R. M. Haberle, R. T. Clancy, F. Forget, M. D. Smith, & R. W. Zurek (Eds.), *The atmosphere and climate of mars* (p. 42–75). Cambridge University Press. doi: 10.1017/9781139060172.004

Smith, M. D., Pearl, J. C., Conrath, B. J., & Christensen, P. R. (2001, 10). Thermal emission spectrometer results: Mars atmospheric thermal structure and aerosol distribution. *Journal of Geophysical Research: Planets*, *106*(E10), 23929–23945. doi: 10.1029/2000JE001321

Sánchez-Lavega, A., del Río-Gaztelurrutia, T., Hernández-Bernal, J., & Delcroix, M. (2019). The onset and growth of the 2018 martian global dust storm. *Geophysical Research Letters*, *46*(11), 6101-6108. doi: 10.1029/2019GL083207

Sonnabend, G., Sornig, M., Kroetz, P., & Stupar, D. (2012, Jan). Mars mesospheric zonal wind around

northern spring equinox from infrared heterodyne observations of CO $_2$. *Icarus*, *217*(1), 315-321. doi: 10.1016/j.icarus.2011.11.009

Sonnabend, G., Sornig, M., Krötz, P. J., Schieder, R. T., & Fast, K. E. (2006, Sep). High spatial resolution mapping of Mars mesospheric zonal winds by infrared heterodyne spectroscopy of CO_2. *Geophysics Research Letters*, *33*(18), L18201. doi: 10.1029/2006GL026900

Titus, T. N., Byrne, S., Colaprete, A., Forget, F., Michaels, T. I., & Prettyman, T. H. (2017). The co2 cycle. In R. M. Haberle, R. T. Clancy, F. Forget, M. D. Smith, & R. W. Zurek (Eds.), *The atmosphere and climate of mars* (p. 374–404). Cambridge University Press. doi: 10.1017/9781139060172.012

Toigo, A. D., Richardson, M. I., Wang, H., Guzewich, S. D., & Newman, C. E. (2018, Mar). The cascade from local to global dust storms on Mars: Temporal and spatial thresholds on thermal and dynamical feedback. *Icarus*, *302*, 514-536. doi: 10.1016/j.icarus.2017.11.032

Tokano, T. (2005). *Water on Mars and Life*. doi: 10.1007/b12040

Vandaele, A. C., Korablev, O., Daerden, F., Aoki, S., Thomas, I. R., Altieri, F., ... ACS Science Team (2019, Apr). Martian dust storm impact on atmospheric H_2O and D/H observed by ExoMars Trace Gas Orbiter. *Nature*, *568*(7753), 521-525. doi: 10.1038/s41586-019-1097-3

Viúdez-Moreiras, D., Gómez-Elvira, J., Newman, C. E., Navarro, S., Marin, M., Torres, J., ... MSL Team (2019, Feb). Gale surface wind characterization based on the Mars Science Laboratory REMS dataset. Part I: Wind retrieval and Gale's wind speeds and directions. *Icarus*, *319*, 909-925. doi: 10.1016/j.icarus.2018.10.011

Wang, H., & Ingersoll, A. P. (2003, Sep). Cloud-tracked winds for the first Mars Global Surveyor mapping year. *Journal of Geophysical Research (Planets)*, *108*(E9), 5110. doi: 10.1029/2003JE002107

Wang, H., & Richardson, M. I. (2015, May). The origin, evolution, and trajectory of large dust storms on Mars during Mars years 24-30 (1999-2011). *Icarus*, *251*, 112-127. doi: 10.1016/j.icarus.2013.10.033

Wang, H., Zurek, R. W., & Richardson, M. I. (2005, Jul). Relationship between frontal dust storms and transient eddy activity in the northern hemisphere of Mars as observed by Mars Global Surveyor. *Journal of Geophysical Research (Planets)*, *110*(E7), E07005. doi: 10.1029/2005JE002423

Widemann, T., Lellouch, E., & Campargue, A. (2007, Oct). New wind measurements in Venus' lower mesosphere from visible spectroscopy. *Planetary Space Science*, *55*(12), 1741-1756. doi: 10.1016/j.pss.2007.01.005

Widemann, T., Lellouch, E., & Donati, J.-F. (2008, Aug). Venus Doppler winds at cloud tops observed with ESPaDOnS at CFHT. *Planetary Space Science*, *56*(10), 1320-1334. doi: 10.1016/j.pss.2008.07.005

Williams, D. R. (2018a). *Nasa space science data coordinated archive.* Retrieved 2019-03-05, from `https://nssdc.gsfc.nasa.gov/planetary/factsheet/marsfact.html`

Williams, D. R. (2018b). *Viking mission to mars.* Retrieved 2019-07-21, from `https://nssdc.gsfc.nasa.gov/planetary/viking.html`

Wilson, C. F. (2003). *Measurement of wind on the surface of mars* (Unpublished doctoral dissertation). Linacre College, University of Oxford.

Wilson, R. J., & Richardson, M. I. (2000, Jun). The Martian atmosphere during the Viking mission. I. Infrared measurements of atmospheric temperatures revisited. *Icarus*, *145*(2), 555-579. doi: 10.1006/icar.2000.6378

Young, A. T. (1975, Jun). The clouds of Venus. *Journal of Atmospheric Sciences*, *32*, 1125-1132. doi:

10.1175/1520-0469(1975)032<1125:TCOV>2.0.CO;2

Yung, Y., & DeMore, W. (1998). *Photochemistry of planetary atmospheres*. Oxford University Press.

Zurek, R., & J. Martin, L. (1993, 03). Interannual variability of planet-encircling dust storms on mars. *Journal of Geophysical Research*, *98*. doi: 10.1029/92JE02936

Zurek, R. W. (2017). Understanding mars and its atmosphere. In R. M. Haberle, R. T. Clancy, F. Forget, M. D. Smith, & R. W. Zurek (Eds.), *The atmosphere and climate of mars* (p. 3–19). Cambridge University Press. doi: 10.1017/9781139060172.002

A Appendix A - Data Results

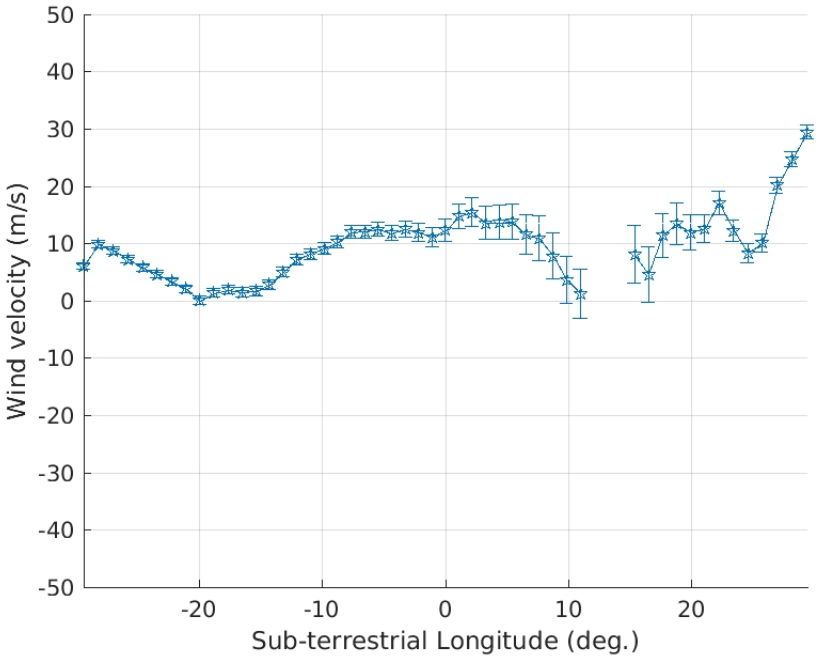

(a)

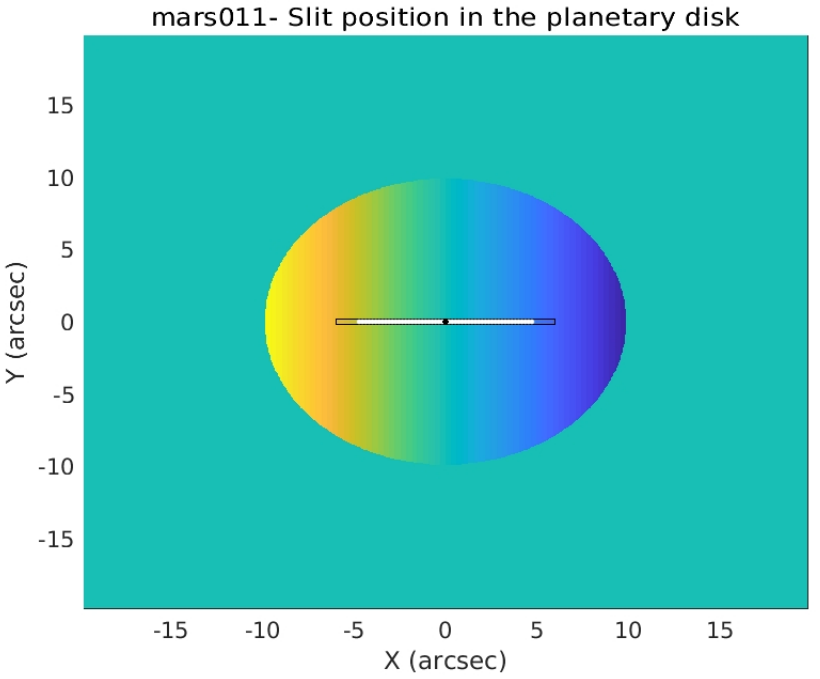

(b)

Figure A.1: (a) Wind velocities along the slit position 1 ($Lat = -14.74°$). (b) Slit's position scheme on the planetary disk.

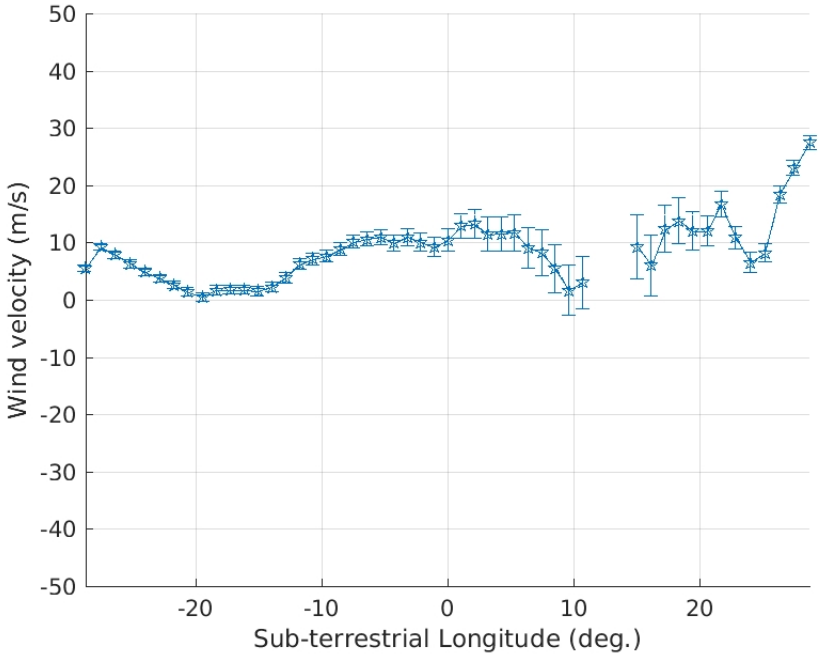

(a)

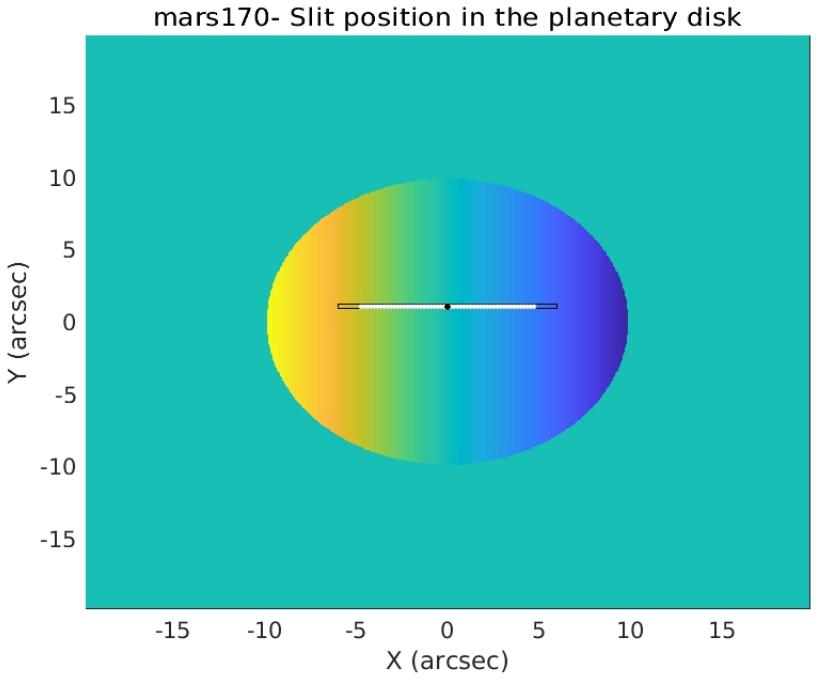

(b)

Figure A.2: (a) Wind velocities along the slit position 2 ($Lat = 8.81°$). (b) Slit's position scheme on the planetary disk.

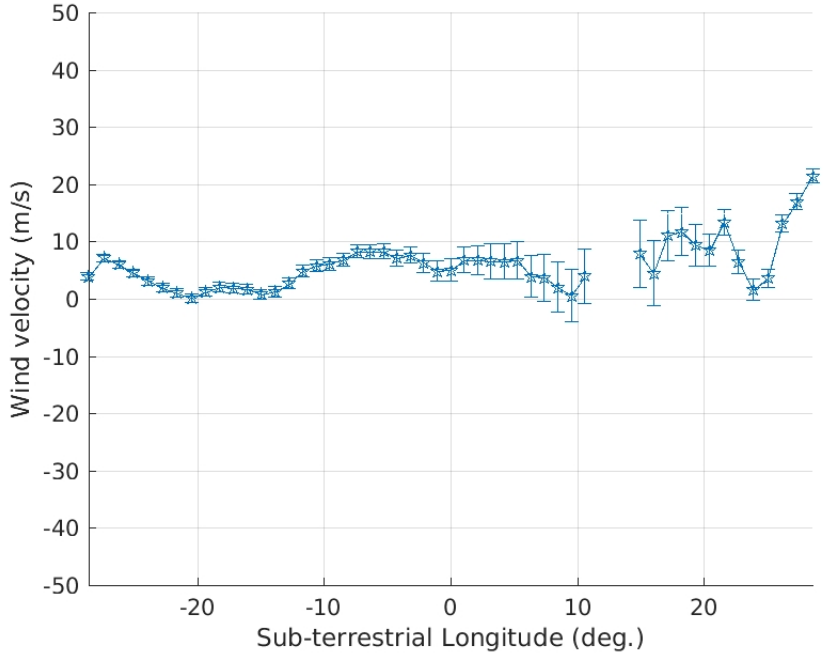

(a)

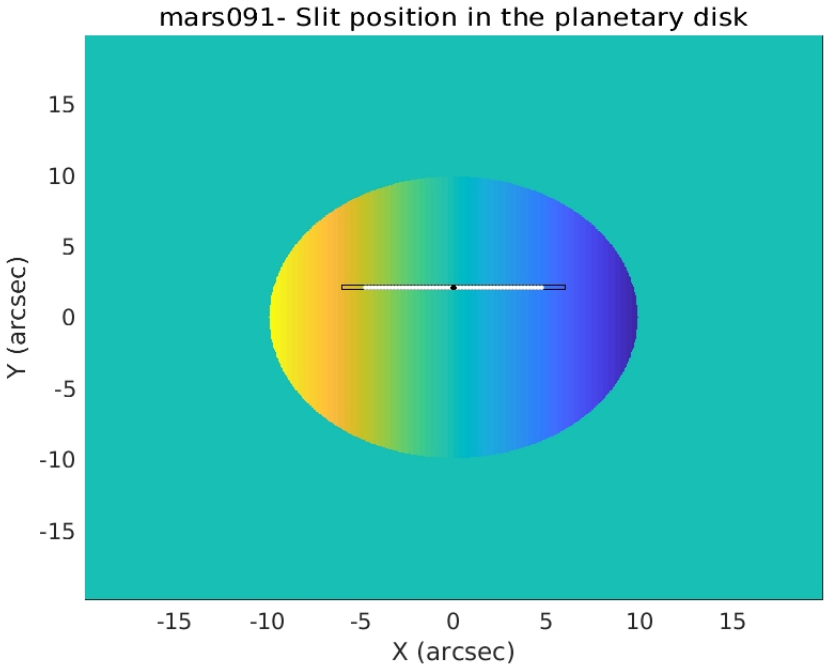

(b)

Figure A.3: (a)Wind velocities along the slit position 3 ($Lat = -2.61°$). (b) Slit's position scheme on the planetary disk.

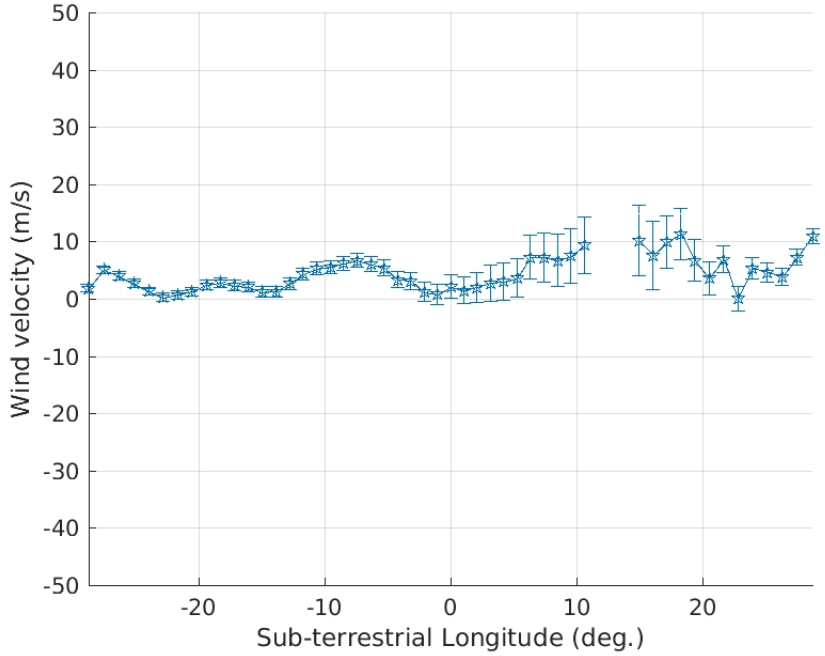

(a)

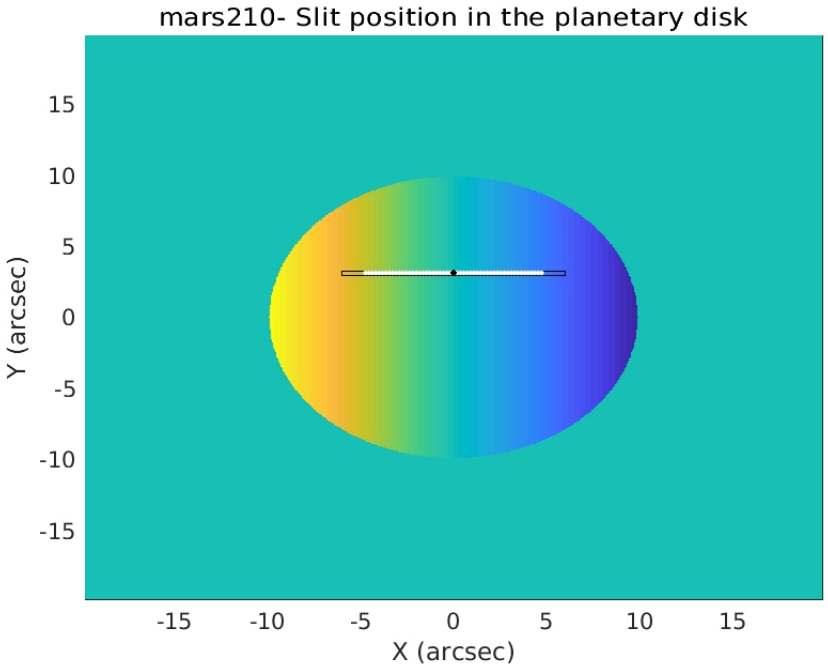

(b)

Figure A.4: (a)Wind velocities along the slit position 4 ($Lat = 3.63°$). (b) Slit's position scheme on the planetary disk.

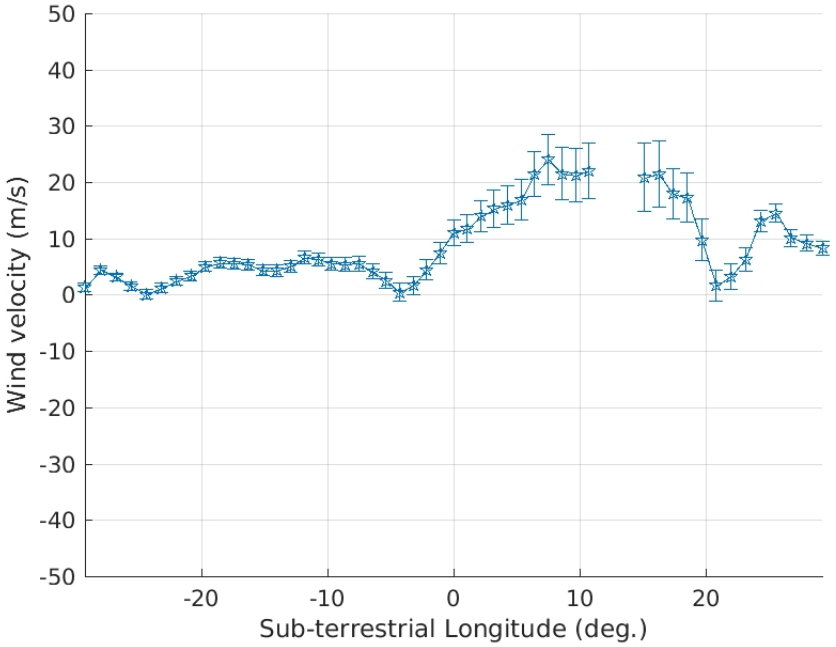

(a)

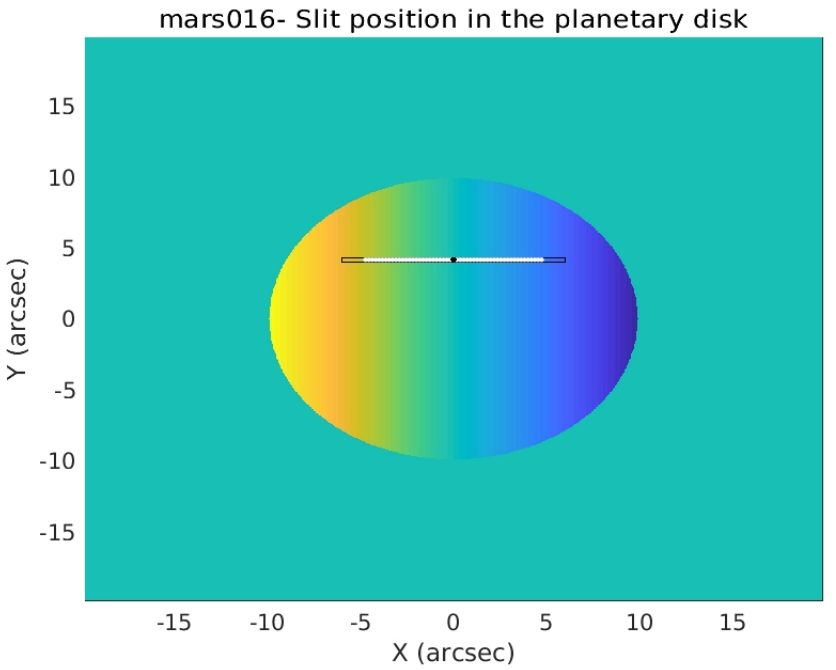

(b)

Figure A.5: (a) Wind velocities along the slit position 5 ($Lat = 10.12°$). (b) Slit's position scheme on the planetary disk.

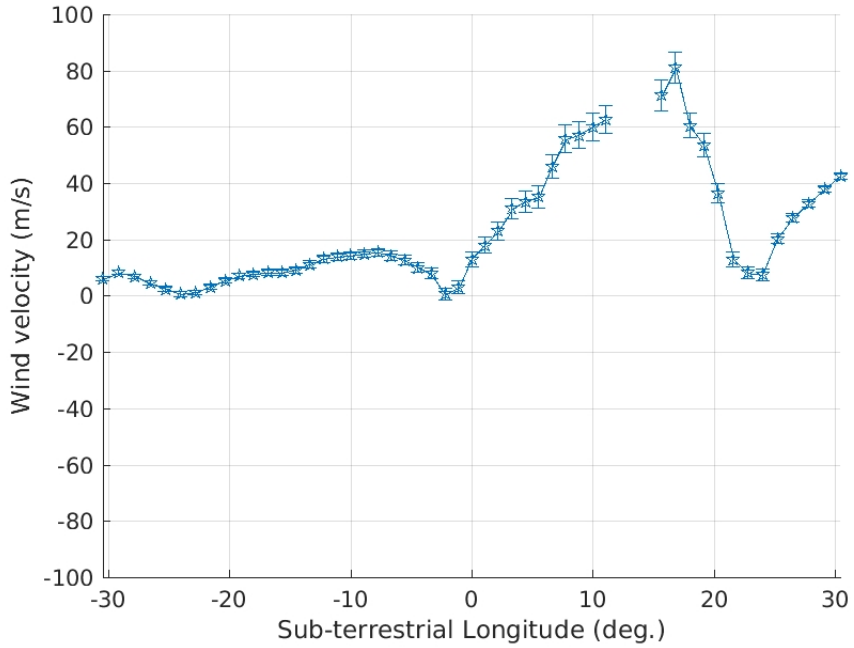

(a)

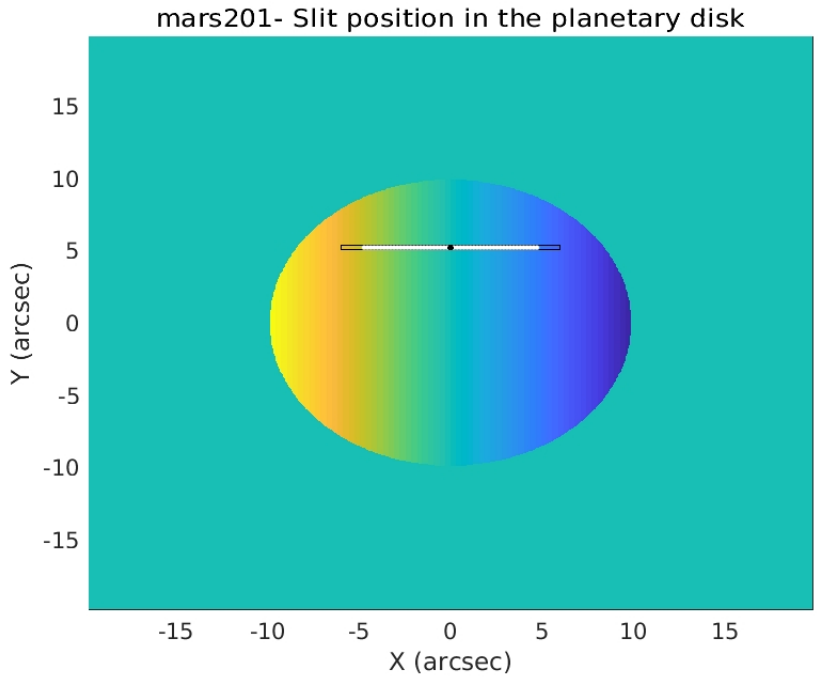

(b)

Figure A.6: (a) Wind velocities along the slit position 6 ($Lat = 16.95°$). (b) Slit's position scheme on the planetary disk.

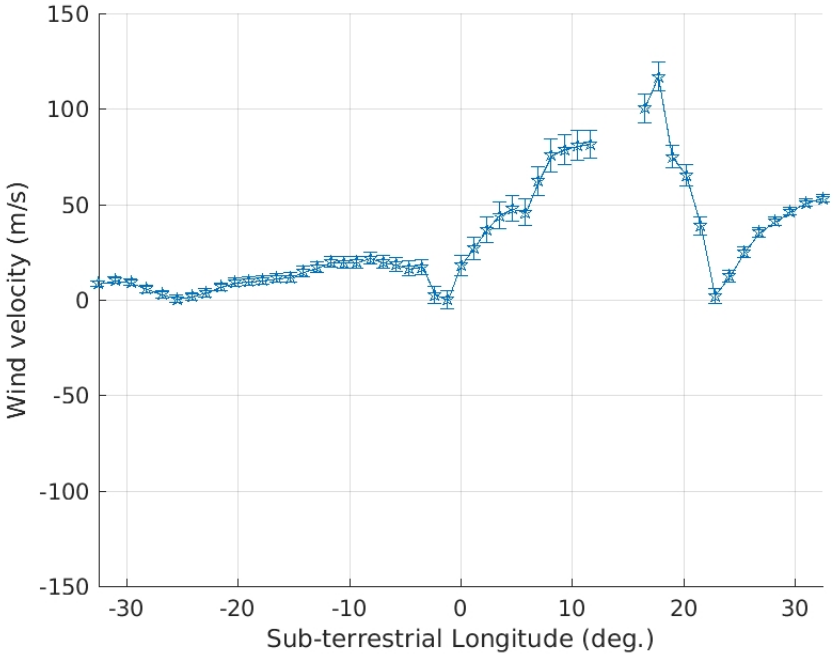

(a)

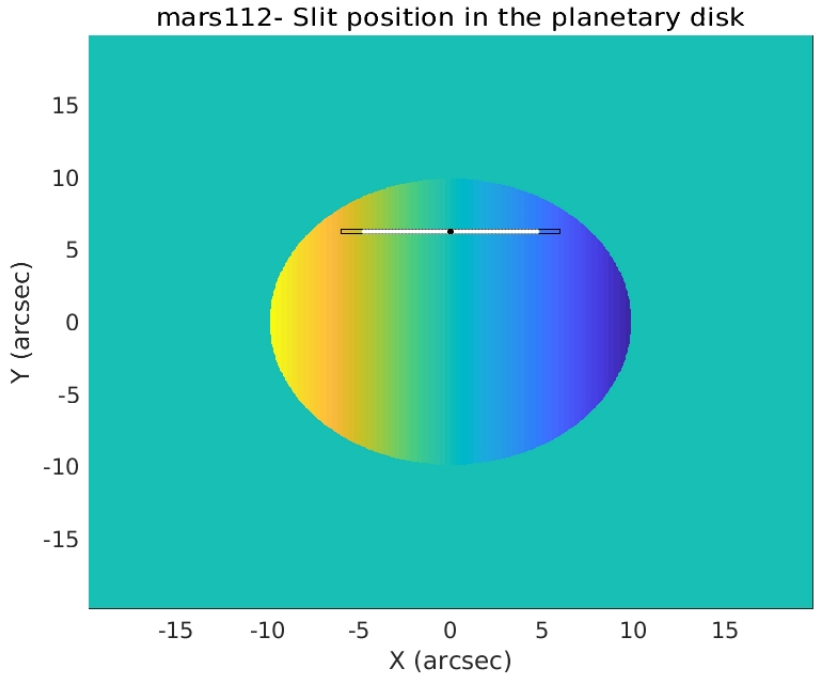

(b)

Figure A.7: (a) Wind velocities along the slit position 7 ($Lat = 24.33°$). (b) Slit's position scheme on the planetary disk.

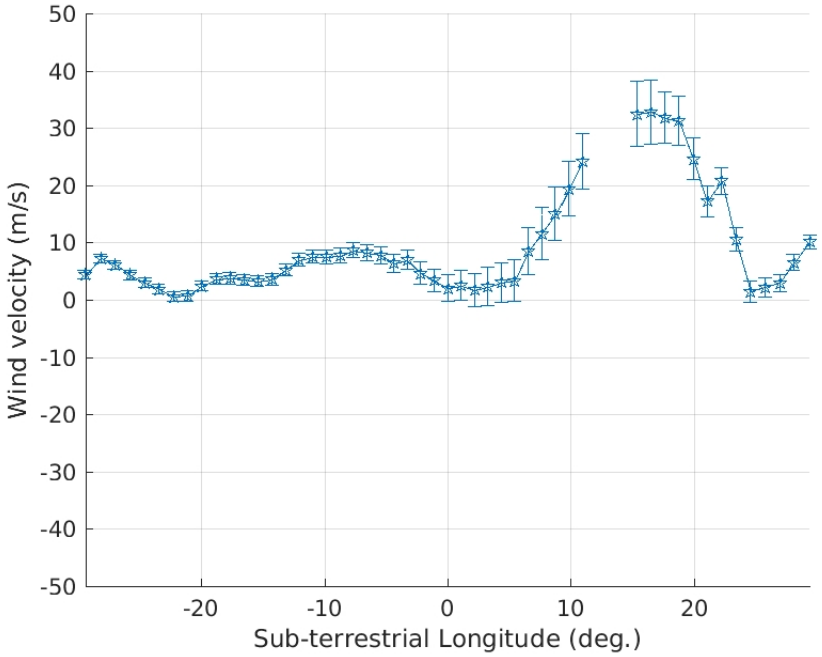

(a)

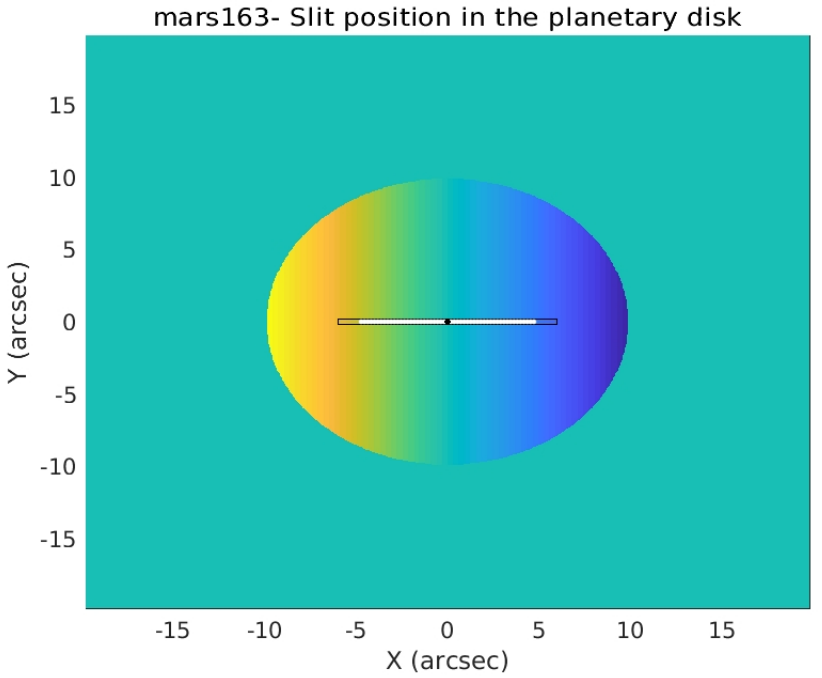

(b)

Figure A.8: (a) Wind velocities along the slit position 8 ($Lat = -14.74°$). (b) Slit's position scheme on the planetary disk.

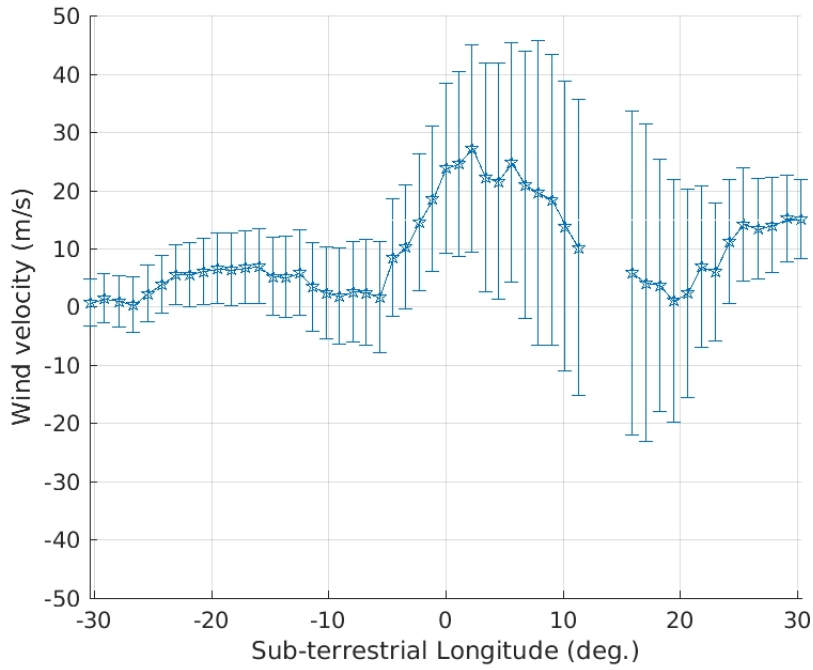

(a)

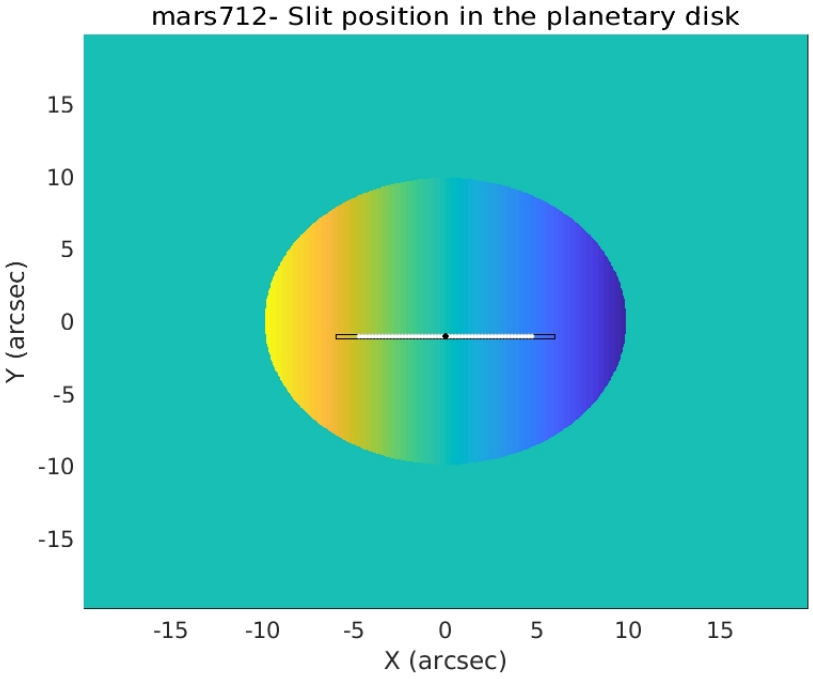

(b)

Figure A.9: (a)Wind velocities along the slit position 9 ($Lat = -20.77°$). (b) Slit's position scheme on the planetary disk.

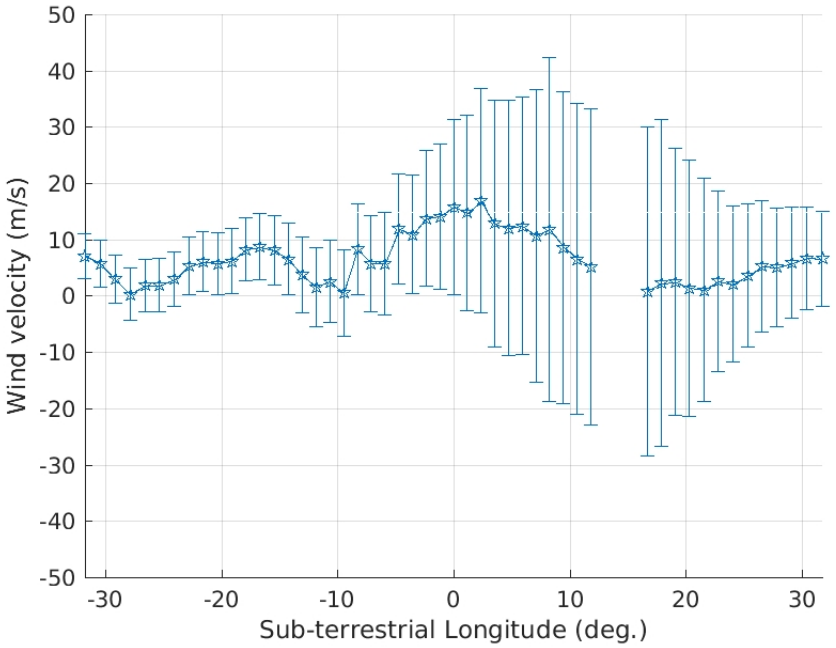

(a)

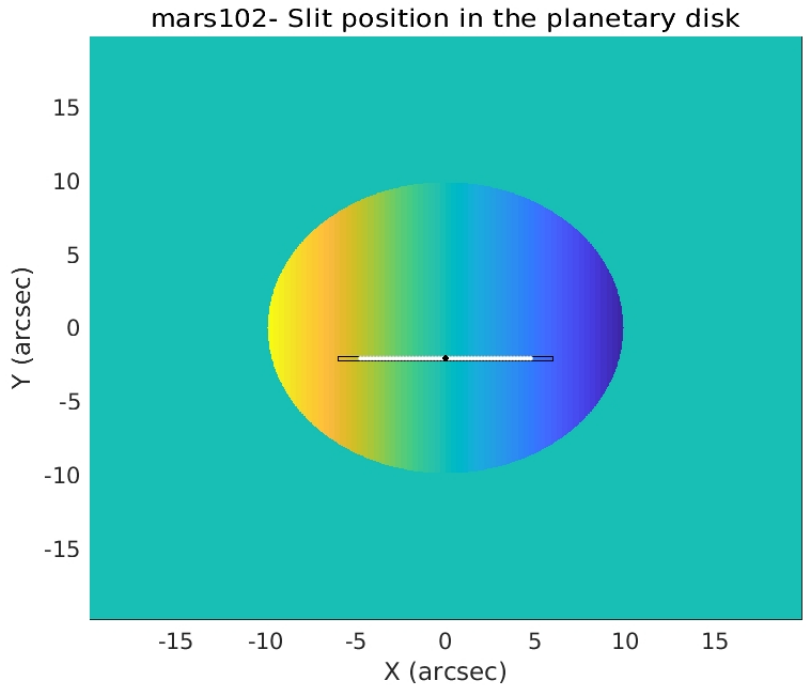

(b)

Figure A.10: (a) Wind velocities along the slit position 10 ($Lat = -26.87°$). (b) Slit's position scheme on the planetary disk.

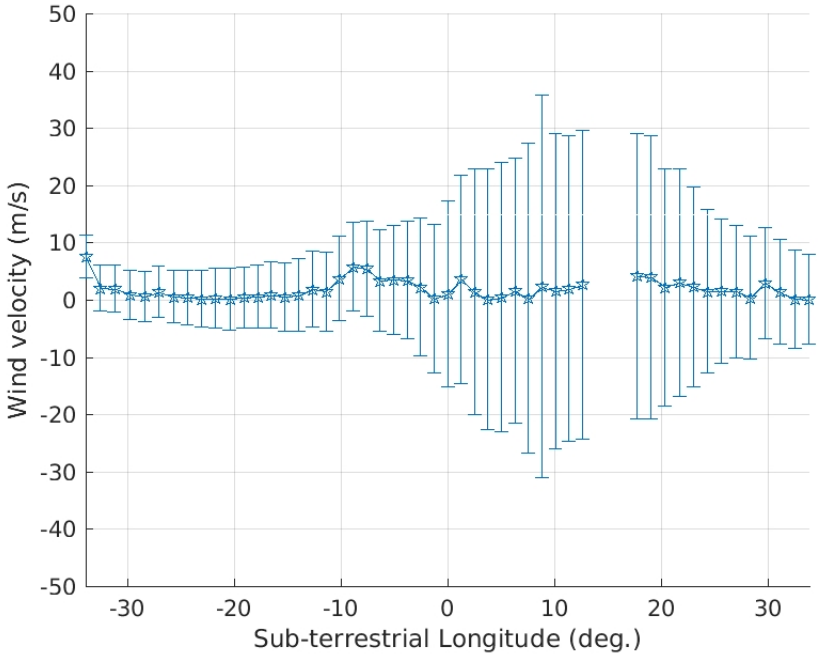

(a)

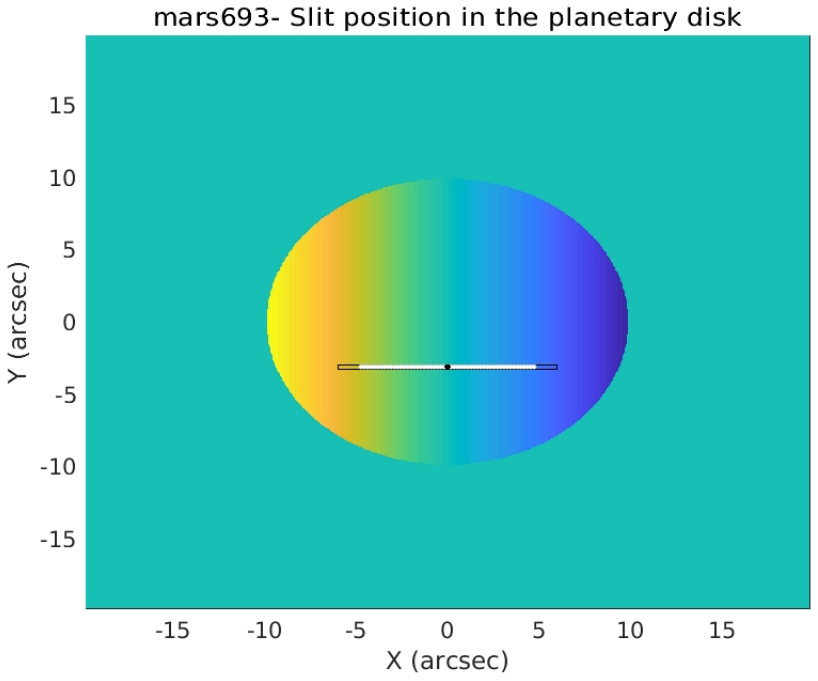

(b)

Figure A.11: (a) Wind velocities along the slit position 11 ($Lat = -33.11°$). (b) Slit's position scheme on the planetary disk.

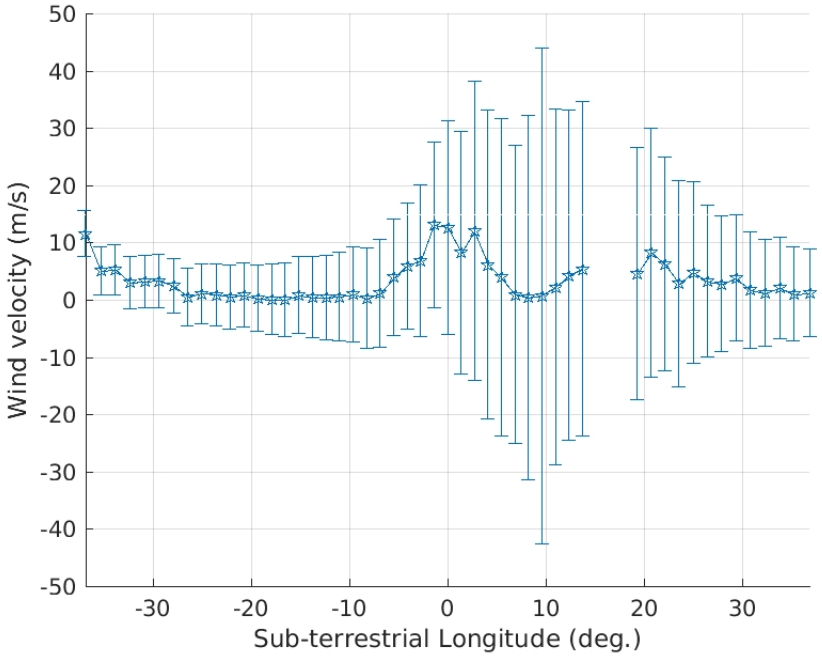

(a)

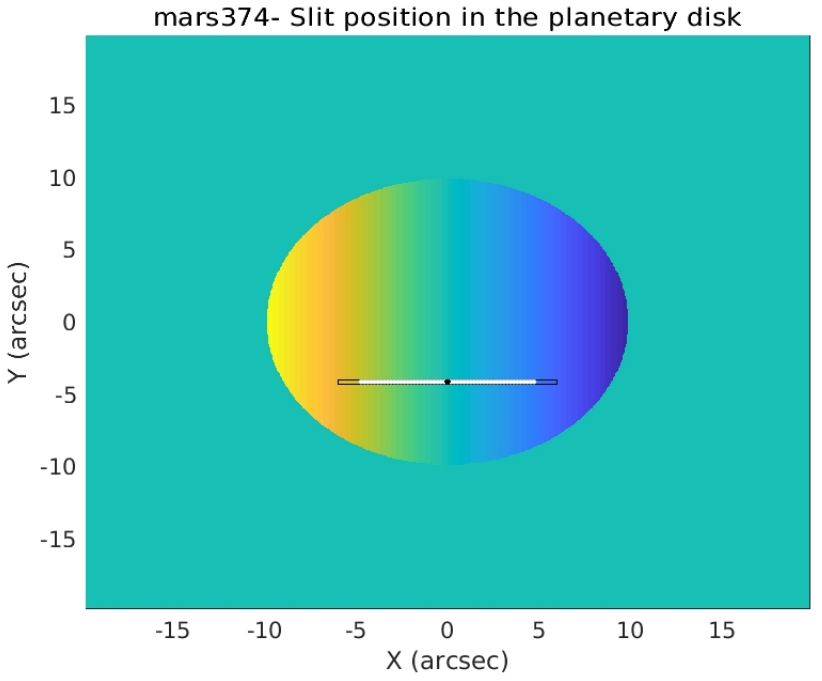

(b)

Figure A.12: (a) Wind velocities along the slit position 12 ($Lat = -39.59°$). (b) Slit's position scheme on the planetary disk.

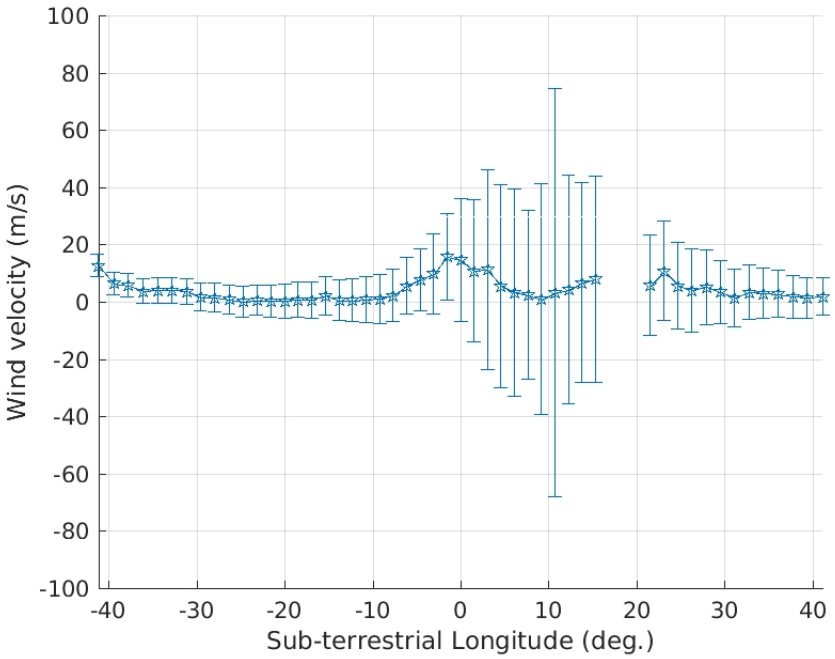

(a)

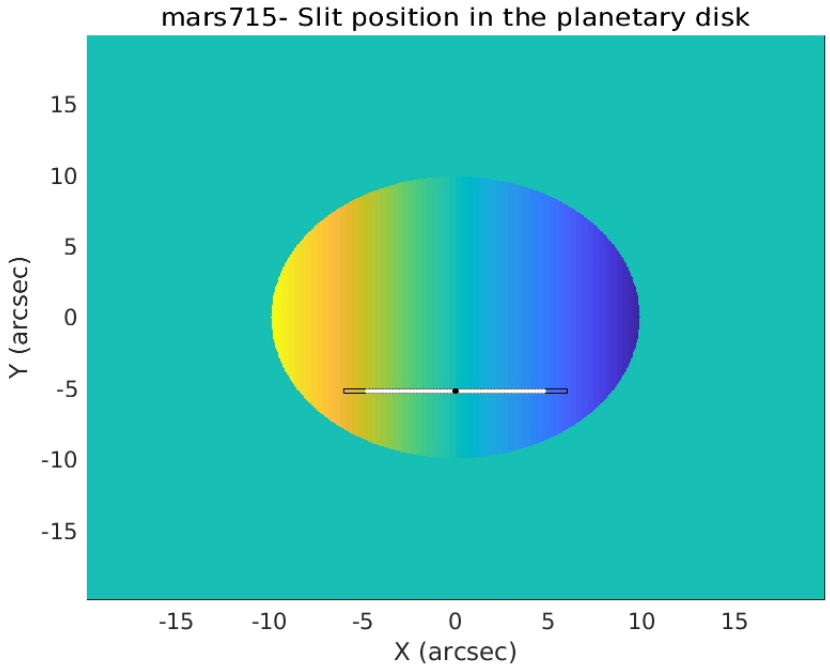

(b)

Figure A.13: (a) Wind velocities along the slit position 13 ($Lat = -46.43°$). (b) Slit's position scheme on the planetary disk.

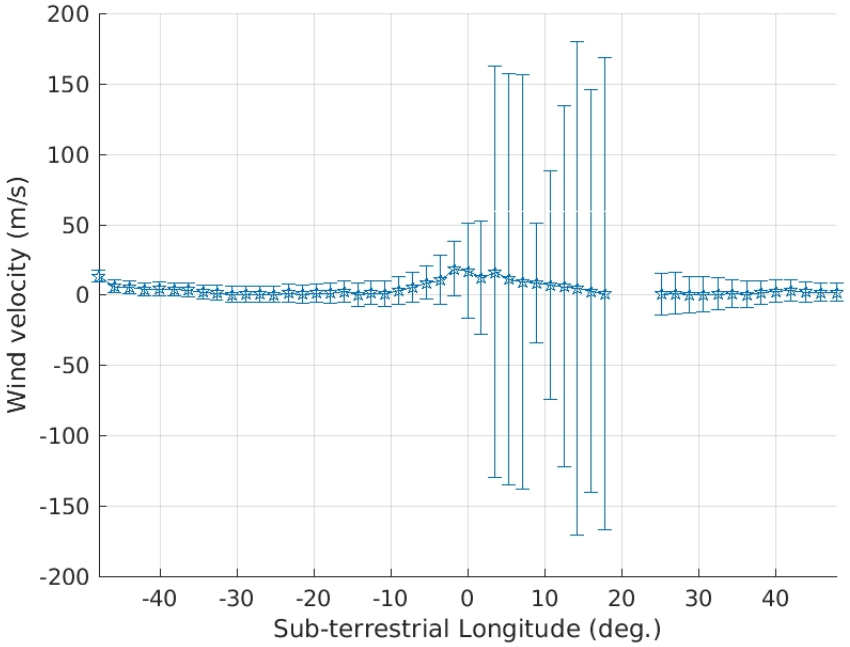

(a)

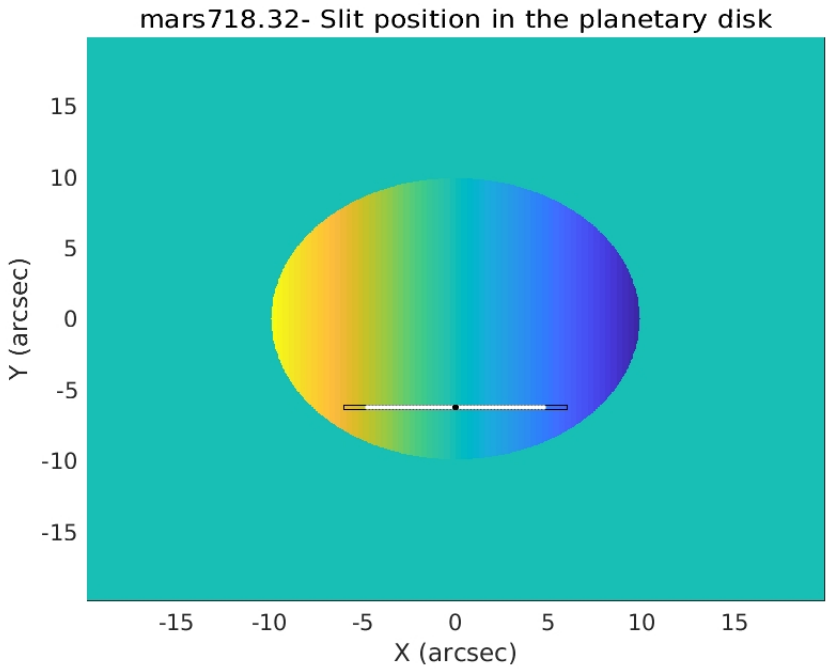

(b)

Figure A.14: (a) Wind velocities along the slit position 14 ($Lat = -53.81°$). (b) Slit's position scheme on the planetary disk.

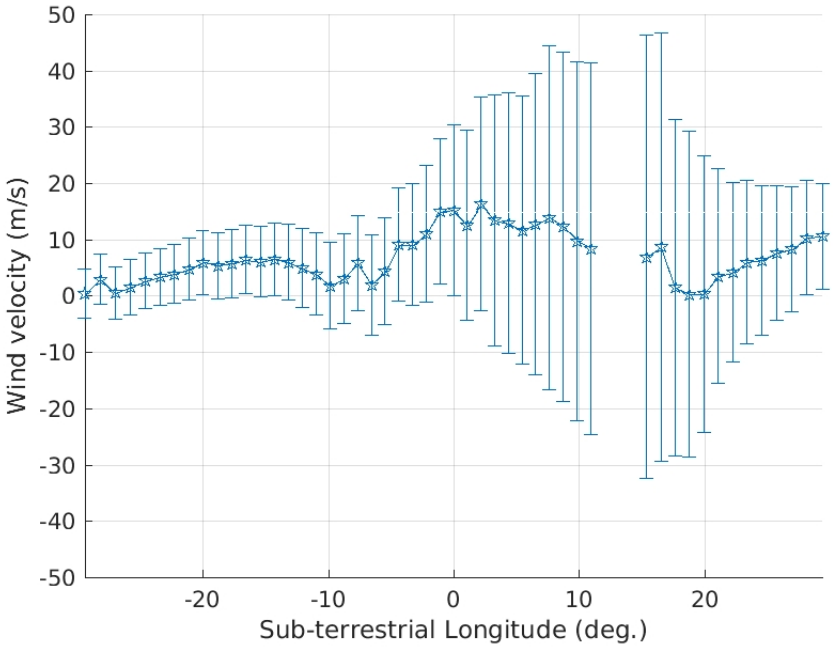

(a)

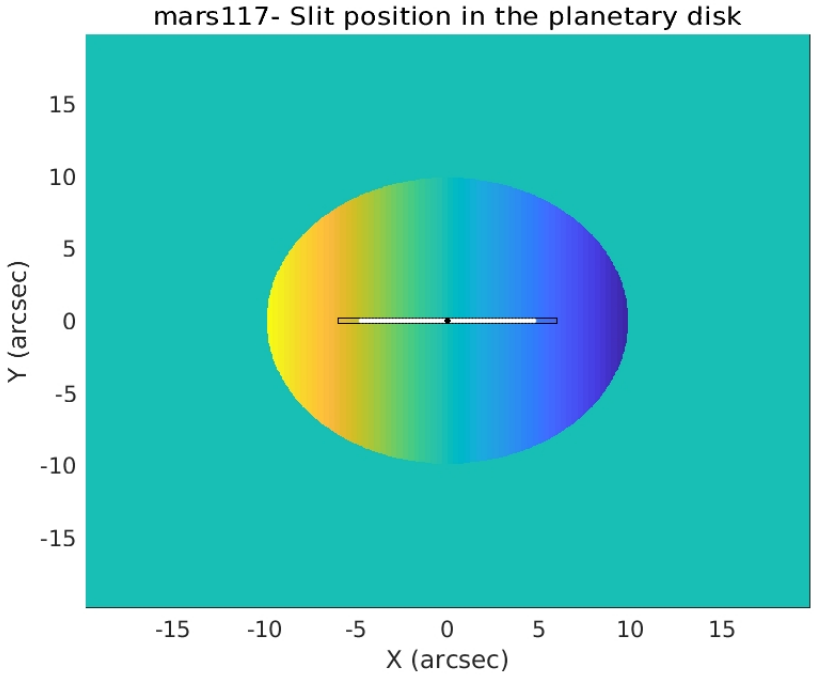

(b)

Figure A.15: (a) Wind velocities along the slit position 15 ($Lat = -14.74°$). (b) Slit's position scheme on the planetary disk.